Spring 5-2022

Implications of Metal Coordination in Damage and Recognition of Nucleic Acids and Lipid Bilayers

Ana Dreab
Old Dominion University, adrea001@odu.edu

IMPLICATIONS OF METAL COORDINATION IN DAMAGE AND RECOGNITION OF NUCLEIC ACIDS AND LIPID BILAYERS

by

Ana Dreab
B.S. June 2015, University of Academy of Science of Moldova, Moldova
M.S. May 2020, Old Dominion University

A Dissertation Submitted to the Faculty of
Old Dominion University in Partial Fulfillment of the
Requirements for the Degree of

DOCTOR OF PHILOSOPHY

CHEMISTRY

OLD DOMINION UNIVERSITY
May 2022

Approved by:

Craig A. Bayse (Director)

Alvin A. Holder (Member)

Jennifer L. Poutsma (Member)

Erin B. Purcell (Member)

Daniel J. Barshis (Member)

ABSTRACT

IMPLICATIONS OF METAL COORDINATION IN DAMAGE AND RECOGNITION OF NUCLEIC ACIDS AND LIPID BILAYERS

Ana Dreab
Old Dominion University, 2022
Director: Dr. Craig A. Bayse

Metal ions have a myriad of biological functions from structural stability to enzymatic (de)activation and metabolic electron transfer. Redox-active metals also mediate the formation of reactive oxygen species which may either cause oxidative damage or protect cellular components. Computational modeling is used here to investigate the role of (1) metal-ion binding to antimicrobial peptides, (2) metal-ion removal and disulfide formation on zinc finger (ZF) proteins, and (3) coordination of thiones/selones for the prevention of metal-mediated redox damage.

Piscidins, natural-occurring antimicrobial peptides, efficiently kill bacteria by targeting their membranes. Their efficacy is enhanced *in vitro* by metal-binding and the presence of membrane-destabilizing oxidized phospholipids (oxPLs). Molecular dynamics (MD) simulations are used to model insertion of Ni^{2+}-bound piscidins 1 (P1:Ni^{2+}) and 3 (P3:Ni^{2+}) into lipid bilayers in the presence and absence of oxPLs. Metallation promotes deeper peptide insertion in the membrane, and P1:Ni^{2+} is suggested to interact more with anionic lipid headgroups in the presence of oxPLs.

The release of Zn^{2+} from ZF proteins through oxidation of the cysteine thiolates is associated with inhibition of viral replication, disruption of cancer gene expression, and DNA repair preventing tumor growth. Multi-microsecond MD simulations were performed to examine the effect of cysteine oxidation on the ZF456 fragment of transcription factor IIIA and its

complex with 5S RNA. Upon oxidation in the absence of RNA, the individual ZF domains unfold yielding a globular ZF456 peptide. Oxidation of the RNA-bound ZF456 peptide disrupts key hydrogen bonding interactions between ZF5/ZF6 and 5S RNA.

The antioxidant properties of sulfur and selenium compounds prevent metal-mediated (i.e., Fenton chemistry) oxidative damage. The effect of the coordination of sulfur/selenium derivatives of imidazolidinone (thiones/selones) on the electronic structure and reduction potential of Fe^{2+} ions solvated or coordinated to guanine are examined using density functional theory. The highest occupied molecular orbital (HOMO) for the Fe(II)-aqua complex is metal-centered but localized on the nucleobase in the Fe^{2+}-guanine complex. Complexation of the thione/selone shifts the HOMO to the sulfur/selenium center suggesting a mechanism for protection of DNA by sacrificial oxidation of the sulfur/selenium ligand.

This dissertation is dedicated to my loving and supporting family.

ACKNOWLEDGMENTS

I would first like to thank my advisor, Dr. Craig. A. Bayse, for giving me the opportunity to conduct my Ph.D. research under his guidance, encouragement, and support. I sincerely thank him for fostering my research and writing skills, inspiring me to perform high-quality work, and for being a patient, considerate, and diligent mentor to me. I would also like to thank my committee members, Dr. Alvin Holder, Dr. Jennifer Poutsma, Dr. Erin Purcell, and Dr. Daniel Barshis for their guidance, support, and valuable feedback throughout the graduate school.

I am grateful to ODU Information Technology Services for managing the High-Performance Clusters, which were essential for my research. Special thanks to Min Dong for providing great assistance with all computational packages. I am also thankful to the ODU Department of Chemistry and Biochemistry for this invaluable opportunity and the continuous assistantship during my time at ODU. I am thankful to the faculty and staff for being kind and welcoming. To all the Bayse laboratory group members, thank you for your support, helpful discussion, and constructive feedback on my work. I am also grateful to my ODU friends and colleagues for sharing the graduate school journey with me.

I am extremely thankful to my family for their unconditional love and support. My mom thought me to value education, have faith, and be always kind. I am beyond grateful for everything she has sacrificed, done, and continues to do for me. I am grateful to my husband, Pavel, for always being by my side. I am thankful to my siblings for encouraging me to follow my dreams and travel overseas to pursue my education. I am also grateful to all my friends that became family. To Taylor and Michael Kelly, thank you for supporting me in realizing my education and career goals.

NOMENCLATURE

A_L	Area per lipid
Aldo-PC	1-palmitoyl-2-(9′-oxo-nonanoyl)-sn-glycero-3-phosphocholine
AMP	Antimicrobial peptide
ARI	Antibiotic-resistant infection
ATCUN	Amino-terminal copper and nickel motif
Cys	Cysteine
COM	Center of mass
CYX	Cystine residue
DFT	Density function theory
DMPC	1,2-dimyristoyl-sn-glycero-3-phosphocholine
DMPG	1,2-dimyristoyl-sn-glycero-3-phosphoglycerol
DOPC	1,2-dioleoyl-sn-glycero-3-phosphocholine
DSSP	Define secondary structure of proteins
FF	Force field
h(C2-C2)	Hydrophobic thickness
h(P-P)	Headgroup-to-headgroup thickness
HID	Histidine residue protonated at the δ-nitrogen
HIE	Histidine residue protonated at the ε-nitrogen
His	Histidine
HOMO	Highest occupied molecular orbital
K_A	Isothermal area expansion (compressibility) modulus

MCPB	Metal Center Parameter Builder
MD	Molecular dynamics
MM	Molecular mechanics
NBO	Natural bond orbital
NPA	Natural population analysis
OxPL	Oxidized phospholipid
oxZF456	Oxidized zinc finger domains 4, 5 and 6
POPC	1-palmitoyl-2-oleoyl-sn-glycero-3-phosphocholine
POPE	1-palmitoyl-2-oleoyl-sn-glycero-3-phosphoethanolamine
POPG	1-palmitoyl-2-oleoyl-sn-glycero-3-phosphoglycerol
P1	Piscidin-1
P3	Piscidin-3
P1:Ni^{2+}	Ni^{2+}-bound piscidin 1
P3:Ni^{2+}	Ni^{2+}-bound piscidin 3
QM	Quantum mechanics
redZF456	Reduced zinc finger domains 4, 5, and 6
RMSD	Root mean square deviations
RMSF	Root mean square fluctuations
ROS	Reactive oxygen species
rS/Se	Reducible sulfur and selenium compounds
S_{CD}	Deuterium order parameters
Selones	Selenium derivatives of imidazolidinone
SOD	Superoxide dismutase

Thiones	Sulfur derivatives of imidazolidinone
TFIIIA	Transcription factor III A
V_L	Volume per lipid
WBI	Wiberg Bond Index
ZAFF	Zinc AMBER FF
ZF	Zinc finger
ZF456	Middle zinc fingers of transcription factor III A
ZPE	Zero-point energy
z	Insertion depth
1$_S$/**1**$_{Se}$	Imidazole thione/selone
2$_S$/**2**$_{Se}$	N-methylimidazole thione/selone
3$_S$/**3**$_{Se}$	N,N′-dimethylimidazole thione/selone
4$_S$/**4**$_{Se}$	1,4,5-trimethylimidazole thione/selone
5$_S$/**5**$_{Se}$	1,3,4,5-tetramethylimidazole thione/selone
ρ	Azimuthal rotation angle
τ	Tilt angle

TABLE OF CONTENTS

Page

LIST OF TABLES

Table Page

LIST OF FIGURES

Figure Page

Figure Page

CHAPTER I

INTRODUCTION

Metals in Biology

Metals serve various biological functions including facilitation of enzyme catalysis by aiding the substrate's positioning and activation for reactions (i), electron transfer (ii), structural stability (iii), and signaling by binding to ligands and behave as molecular "switches" (iv).[1–7] Additionally, redox-active metals (e.g., Fe(II/III), Cu(I/II)) can function as redox centers and transport oxygen.[1–4,8–10] Previous surveys on enzymes with experimentally characterized structures estimated that 47% of these proteins required metals to function.[2,9] Metalloenzymes predominantly use magnesium (16%), zinc (9%), iron (8%), and manganese (6%) to achieve their catalytical roles (Figure 1).[2,9] Other metals include calcium, cobalt, copper, vanadium, molybdenum, tungsten, nickel, sodium, and potassium; one enzyme makes use of cadmium. Oxidoreductases (i.e., dehydrogenases and NAD^+ reductases) perform their electron transfer using mostly iron (81% distribution across the enzyme classes), copper (93%), and molybdenum and tungsten (81%).[2]

Sodium, potassium, magnesium, and calcium constitute the biological bulk elements being greatly abundant.[3] Na^+ and K^+ are generally required for osmotic balance, charge compensation when bound to anionic functional groups, e.g., of nucleic acids, and enzymatic catalysis.[5,11] Na^+ and K^+ advance enzyme activation in two distinct modes: type I, where the

---

This Dissertation is formatted based on the Journal of Chemical Information and Modeling.

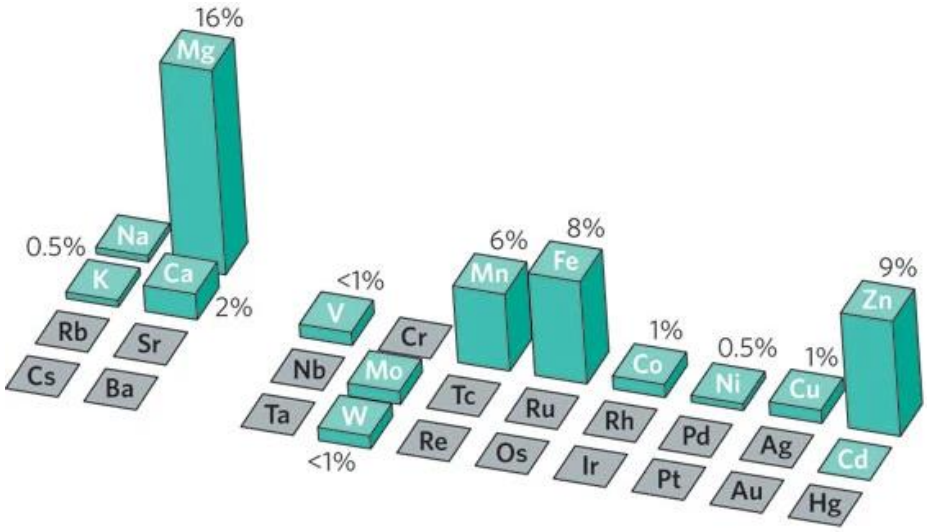

Figure 1. Metals used in biological catalysis. The height of the column is proportional to all enzymes with known structures using the respective metal. Cd is used by a single enzyme. Reprinted with permission from reference [9].

monovalent cations (M^+) bind to the active site of the enzyme connecting it to the substrate and often work simultaneously with divalent cations (i.e., Mn^{2+}, Mg^{2+} or Zn^{2+}), and type II, where the M^+ binds at a different site than the active one and induces conformational transitions.[12,13] Examples of K^+-promoted type I activation assisted by Mg^{2+} ions include kinases (e.g., pyruvate, pyridoxal, branched-chain α-ketoacid dehydrogenase, and pyruvate dehydrogenase),[14–17] recombinases (e.g., Rad51),[12] and phosphatases (e.g., fructose-1,6-bisphosphatase and S-adenosylmethionine synthase)[18,19]. Class II aldolases, such as fructose- and tagatose-1,6-bisphosphate follow a Na^+-dependent type I activation paired with Zn^{2+}.[20,21] Examples of type II activation are found in ribokinases (with no discrimination for Na^+ or K^+),[22] pyridoxal 5'-phosphate (PLP)-dependent enzymes (e.g., dialkyl glycine decarboxylase, serine dehydratase,

tryptophanase, tyrosinase, and tryptophan synthase),[23–27] thrombin (performed by Na^+),[28] certain K^+-dependent dehydrogenases,[29] and Na/K-ATPase[30].

The essential divalent metal ions typically bind to biomolecules according to the Irving–Williams series (i.e., $Mg^{2+} < Mn^{2+} < Fe^{2+} < Co^{2+} < Ni^{2+} < Cu^{2+}$ (Cu^+) > Zn^{2+}), unless steric hindrance is present.[31] Magnesium is important for regulating ion channels, enzymes, signaling pathways, metabolic cycles, and assisting nucleic acid and protein folding.[32,33] DNA polymerases use Mg^{2+} for high-fidelity DNA replication.[34] Calcium is involved in almost all aspects of cell function being able to bind reversibly to geometric irregular sites and displaying a fast ligand-exchange rate.[35] The 1% of Ca^{2+} not localized in bones as hydroxyapatite or teeth as fluorapatite can interact with plasma membrane receptors to activate various signaling pathways.[3] Ca^{2+}-binding proteins belong to two classes that have a different impact on the total cellular content of Ca^{2+}. The proteins in the first class may act as Ca^{2+} "sensors" and are responsible for Ca^{2+} buffering and maintaining the relevant Ca^{2+} homeostasis.[36,37] The second class consists of membrane proteins that transport Ca^{2+} across plasma or organelle membranes.[36] Some well-known Ca^{2+}-interacting examples include EF-hand proteins (e.g., calmodulin, S-100, parvalbumin, and calretinin), C_2-domains (e.g., in protein kinase C), annexins, and ATPase.[36]

Manganese, iron, cobalt, copper, zinc, and molybdenum constitute the trace metals biologically relevant for humans. Mn is incorporated in several enzymes such as arginase, phosphoenolpyruvate decarboxylase, and superoxide dismutase (SOD).[3] The arginase enzyme catalyzes the rate-determining step of the urea synthesis and MnSOD is a mitochondrial metalloprotein that mitigates reactive oxygen species (ROS).[38] Iron is an essential micronutrient whose levels are strictly controlled via a complex endocrine and paracrine system.[39,40] Ferric iron is transported through the blood by the serum protein, transferrin and is intracellularly stored by

the globular protein, ferritin.[41,42] The cytosolic Fe is exported by the transmembrane protein, ferroportin.[43] Among the ~500 human metalloproteins containing Fe, numerous ones have either a heme prosthetic group (e.g., hemoglobin, myoglobin, and cytochromes) or an Fe-S cluster.[39] Within the Fe-containing heme-proteins, hemoglobin and myoglobin transport and store oxygen;[44] cytochromes are responsible for electron transfer and redox catalysis;[45] peroxidases catalyze the oxidation of substrates by hydrogen peroxide;[46] and catalases decompose hydrogen peroxide to water and oxygen.[47] Fe-S clusters are structurally and chemically diverse and take part in a variety of processes including electron transfer, regulation of gene expression and enzyme activity, substrate binding and activation, and Fe storage.[48] Cobalt is mainly encountered in association with cofactors in cobalamin-dependent enzymes.[9] Vitamin-B_{12} (cyanocobalamin) is the only human vitamin for that contains metal and is synthesized exclusively by microorganisms.[49] Some prominent enzymes essential for human health that have cobalamin as a cofactor are methylmalonyl-coenzyme A mutase which helps break down several amino acids, some lipids and cholesterol, and methionine synthase.[50,51]

Copper and zinc are catalytic and structural cofactors for a huge number of proteins and enzymes, and both metals play an important role in the function of the immune system.[4,52,53] Similar to Fe, the intracellular bioavailability of Cu is tightly regulated by the transporter (e.g., albumins) and chaperone proteins.[54] Cu participates in mitochondrial energy (ATP) production through cytochrome c-oxidase. It offers protection against oxidative stress via Cu/Zn SOD and supports extracellular matrix stability by covalently crosslinking collagen and elastin via lysyl oxidase.[54] Cu also acts as a cofactor in monooxygenases which catalyze peptide amidation and maturation,[55] amine oxidase which is responsible for the oxidative deamination of primary amines,[56] and coagulation factors V and VIII. Cu, as well as Zn, assist protein folding. Zn

cellular uptake, distribution, storage, and release are regulated by metallothioneins which have a high cysteine (Cys) and low aromatic content.[5,53] This metal plays a structural role in Zn finger (ZF) proteins, in which Zn is tetrahedrally coordinated by a combination of Cys and histidine (His) residues, and a catalytic role in enzymes such as carbonic anhydrase, carboxypeptidase, alkaline phosphatase, and alcohol dehydrogenases. Many ZF proteins may mediate protein-protein interactions in addition to binding to nucleic acids.[3,53,57]

Molybdenum is found mostly in association with cofactors (i.e., FeMo or pterin-based) in Mo-dependent enzymes.[58] This trace element is important for almost all organisms since it is used by a great variety of enzymes including nitrogenase (bacterial Mo nitrogenase is the only one that uses FeMo as a cofactor), nitrate reductases, sulfite oxidase, and xanthine oxidoreductases.[59] Nitrate reductase which is not found in animals, is involved in the inorganic nitrogen assimilation.[60] The eukaryotic sulfite oxidase catalyzes the final step in the degradation of S-containing amino acids (e.g., methionine and taurine), where the sulfite is oxidized to sulfate.[60] The mammalian xanthine oxidoreductases may have dual activity: dehydrogenase and oxidase, and are involved in purine catabolism.[61]

Vanadium, nickel, cadmium, and tungsten are only essential for some forms of life.[3] W and Mo share similar chemical features (e.g., atomic, and ionic radii), and W can substitute for Mo in many prokaryotic enzymes.[62] Vanadium is essential for many marine algae, bacteria, and fungi which contain V-depending haloperoxidases and/or nitrogenases.[63] V haloperoxidases use hydrogen peroxide to catalyze the oxidation of halide ions, and V nitrogenases reduce N_2 to NH_3 in bacteria.[64] Ni-containing enzymes or cofactors occur in archaea, bacteria, unicellular eukaryotes, and plants.[3] Eight Ni enzymes are known to date and all, except glyoxalase I, are involved in the production and/or use of key gases (i.e., H_2, CO, CO_2, CH_4, NH_3, and O_2) from

the global biological carbon, nitrogen, and oxygen cycles.[65] Cadmium-carbonic anhydrase is the only natural occurring enzyme that contains Cd. Additionally, several phytoplankton species may use a low concentration of Cd^{2+} ions to enhance their growth under Zn limitations.[66]

Metal homeostasis is generally highly regulated throughout biology via complex mechanisms involving metal sensors and chaperones.[67] However, dyshomeostasis is presumed to contribute greatly to pathologies. For example, a high level of Mg^{2+} in the blood (hypermagnesemia) results in renal failure, and hypomagnesemia is related to many conditions including cardiovascular pathologies, hypertension, and alcoholism.[3,5] The Cu level in serum elevates in response to inflammation,[68] and nutritional Cu deficiency causes impaired immune responses, neuropathies, and iron deficiency anemia (Cu is necessary for the absorption of Fe from the gut).[52] Genetic Cu deficiency causes Menkes (mental and physical developmental impairment), while Cu excess leads to Wilson's disease (accumulation of Cu in vital organs).[69] Aberrant Cu transport has also been associated with Parkinson's Huntington's, and Alzheimer's diseases.[52,70,71] Zn deficiency during pregnancy compromises embryonic, fetal, and postnatal development giving rise to neurological disorders, immune system dysfunction, and growth retardation. Impaired Zn absorption is a cause for acrodermatitis enteropathica, a rare recessive genetic disorder.[72] Fe deficiency alters its homeostasis and is related to anemia.[39] Increased Fe absorption from food is known as hereditary hemochromatosis and can result in diabetes or liver disease, and heart problems as excess Fe is stored in these organs.[8] Deficiency of Mo pterin-based cofactor is a rare recessive hereditary disorder that eventually causes the death of the patients.[59] A good and complete understanding of metal homeostasis and sensing would likely aid in the improved understanding of metal aberrations and in the development of novel therapies.

This dissertation focuses on three distinct research topics involving the biological activity of transition metals. First, Cu^{2+} and Ni^{2+} peptide-binding motifs are investigated for their ability to modify features of antimicrobial peptides in lipid bilayers proposed to enhance membrane disruptive activity. The second topic focuses on the zinc finger proteins and structural effects of oxidation of their Zn^{2+}-binding sites as occurs in some promising anticancer and antiviral treatments. Lastly, Fe^{2+}-mediated oxidative stress and its prevention by sulfur and selenium compounds are addressed.

The amino-terminal copper and nickel (ATCUN) motif of proteins and peptides

The ATCUN binding unit is a naturally occurring structural motif found in proteins (e.g., albumins and protamins) and peptides (e.g., histatin-3/5 and piscidin 1/3) that contain: a free NH_2 terminus (1), a His residue in the third position (2), and two intervening backbone amide groups (3) (Figure 2).[73] The ATCUN-Cu^{2+} complexes, formed by the high-affinity coordination of the first three backbone nitrogen and the histidine imidazole-N^{δ} to Cu^{2+} in a square planar geometry, can form reactive oxygen species (ROS) leading to oxidative damage of biological molecules.[73–78] As a result, the ATCUN-Cu^{2+} motif in proteins/peptides often has nuclease, protease, and lipase activity which is utilized in protein design for therapeutic purposes.[74,76,79] The ATCUN-Ni^{2+} motif is also effective at cleaving DNA but through a different mechanism than the ATCUN-Cu^{2+} complex.[73] Additionally, the ATCUN-M^{2+} derivatives have been investigated for a large range of biological and chemical applications such as enhanced antitumor activity,[80] enzyme inhibition,[81] water oxidation,[82] hydrogen evolution,[83] nitrite to ammonia reduction,[84] spectroscopic probes, and imaging agents.[85]

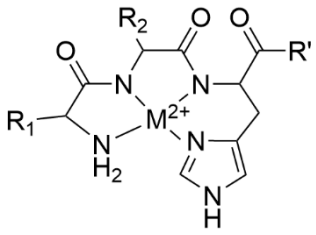

Figure 2. Schematic representation of the ATCUN motif.

The antimicrobial peptide (AMP) database (https://aps.unmc.edu/database) includes more than 40 entries for naturally occurring peptides that possess an ATCUN motif, but the role of this motif in the biological activity of the peptides has not been directly examined for all.[86] Synthetic ATCUN-Cu^{2+} AMPs have been made to explore the oxidative cleavage activity of the ATCUN-M^{2+} structure, and thus to enhance the antimicrobial activity of the peptides.[77,87–89] This increased activity is believed to be due to the generation of ROS which oxidize the lipids in the membrane.[77,87,88] For example, a correlation was established between the rate of ROS generation and the extent of lipid oxidation for the ATCUN derivatives of anoplin, a membrane-active peptide with broad-spectrum antibacterial activity.[88] In a time of continued increase in antibiotic resistance, metalloantibiotic-based AMPs may represent promising novel therapeutics.

Zinc finger (ZF) proteins

Approximately 10% of all proteins encoded in the human genome take part in Zn^{2+} binding according to bioinformatic studies.[90] ZF proteins are a major subset of Zn-binding proteins and one of the most numerous classes of proteins. ZFs were first discovered in 1985 as sequence-specific DNA binding motifs in the *Xenopus laevis* protein transcription factor IIIA

(TFIIIA).[91] The name, zinc fingers, started as laboratory jargon because they incorporated zinc and gripped DNA.[92] Based on the combination of Cys and His residues binding to Zn^{2+}, ZFs can be divided into three classes: Cys_4, $Cys_2HisCys$ (Cys_3His), or Cys_2His_2 (Figure 3).[93,94] The apoprotein binds Zn^{2+} ions only in a tetrahedral coordination geometry which offers increased stabilization to the ZF cores compared to other metal ions bound to the same cores. Nonetheless, since Cys binding to Zn^{2+} is entropically driven causing the stability of the ZF core to be more susceptible to temperature, pH, and ionic strength, the overall reactivity of ZFs is enhanced.[95] For example, the substitution of Zn^{2+} by other metal ions can lead to incomplete metal coordination or Cys oxidation.[95] Interactions with reactive oxygen or nitrogen species, reducible sulfur/selenium (rS/Se) compounds, and with other cellular oxidants cause the oxidation of Cys thiolates and subsequent release of Zn^{2+}. In the absence of the key structural metal ion, the

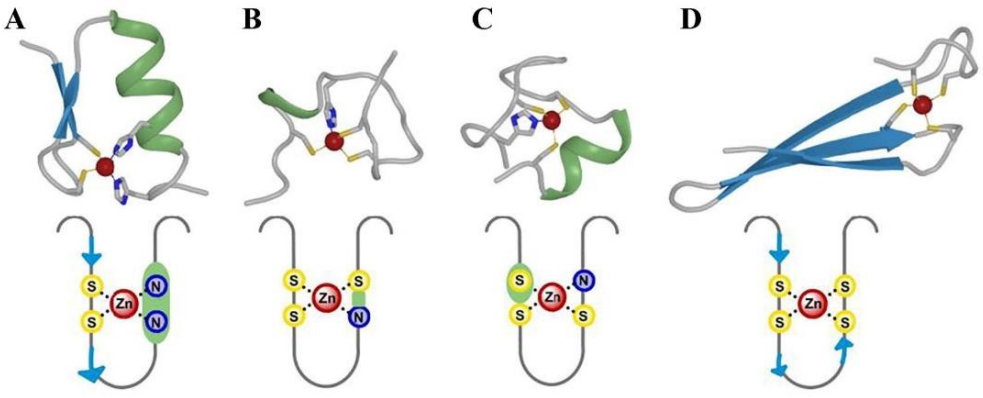

Figure 3. Graphical representation of domain folds and metal coordination within single-ZF proteins. (A) Cys_2His_2 ZF from ZNF478 (PBD: 2yrh), (B) $Cys_2HisCys$ (gag knuckle) from HIV-1 NCp7 (PDB: 2l44), (C) Cys_3His ZF from tristetraprolin (PDB: 1m90), (D) Cys_4 (zinc ribbon) from TIF 2 (PDB: 1k81). β-sheets, α-helixes, and Zn^{2+} ions are colored in blue, green, and red, respectively. Adapted with permission from reference [95].

tertiary structure of the ZF protein unravels leading to the loss of ZF functions.

Zn^{2+} release is associated with disruption of gene expression and DNA repair, which can prevent tumor growth. For example, both ebselen and selenite inhibit DNA binding by TFIIIA, SP1, and NF-κβ *in vitro*.[96,97] Combined inhibition *in vivo* of ZFs may explain ebselen's autoinflammatory and anti-cancer effects.[96] Recently, disulfiram and ebselen were shown to eject Zn^{2+} from the multiprotein SARS-CoV2 replication and transcription complex (i.e., nsp10, nsp13, and nsp14) and inhibit SARS-CoV-2 replication when combined with remdesivir.[98,99] Thus, targeting specific ZF proteins may be a selective way to fight viral infections and cancer. The mechanism of Zn^{2+} release by rS/Se oxidants involves an initial electrophilic attack of the rS/Se compounds (represented as RE–X, E = S, or Se) on a ZF Cys sulfur (Figure 4). A sulfenated/selenenated intermediate is formed following the transfer of RE^+ to the Cys and loss of X^-. In the case of the weaker electrophiles, a chalcogen bonded donor-acceptor intermediate may be formed along this pathway.[100] The ZF undergoes (1) internal Cys attack to form an intramolecular disulfide bond (oxZF) with the release of RE^- and/or (2) sulfen-/selenenation of the remaining Cys by additional rS/Se equivalents. The softer rSe compounds interact more strongly than their sulfur counterparts while the reactivity of ZF models decrease in the series: Cys_4 > $Cys_2HisCys$ > Cys_2His_2.[100–102]

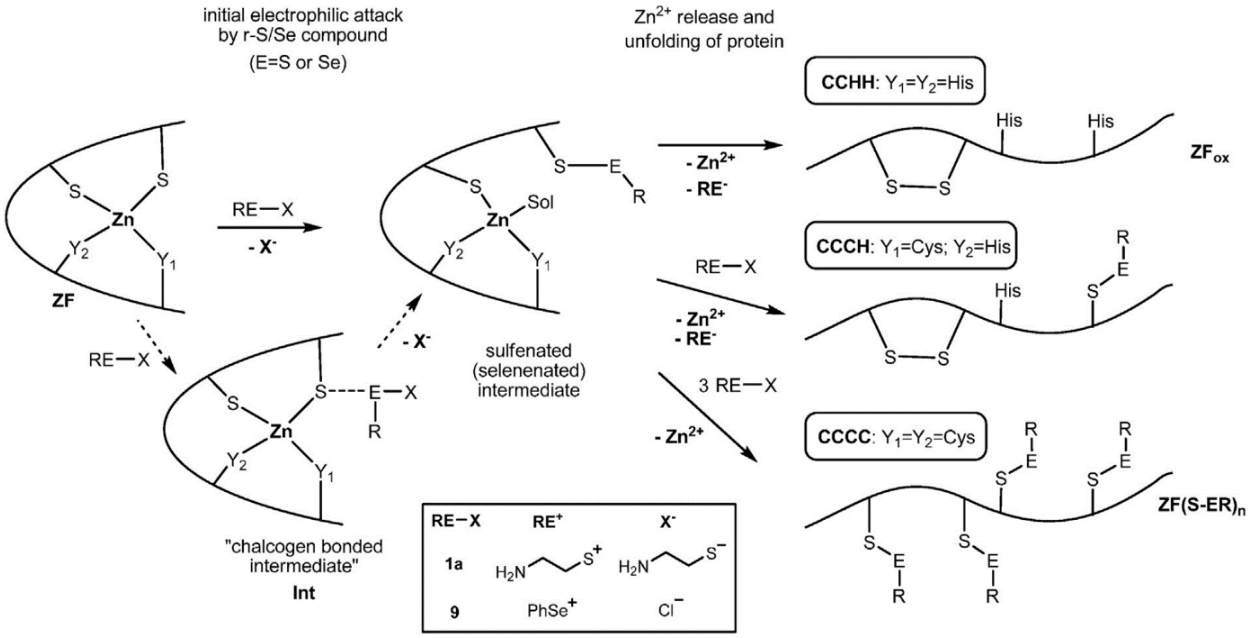

Figure 4. Mechanism of Zn^{2+} release from ZF proteins by rS/Se compounds (RE–X) with examples of sulfen−/selenenating groups (RE^{+}, shown in the inset). Reprinted with permission from reference [100].

Metal-mediated ROS generation and Oxidative Stress

Elevated intracellular amounts of ROS are linked with (1) oxidative stress which causes DNA, protein, and lipid damage, and (2) redox biology, where ROS are used as signaling molecules to initiate biological processes. Usually, a small increase in ROS levels refers to redox biology, whereas a high ROS level is defined as oxidative stress and has been associated with numerous pathologies such as inflammatory and neurodegenerative diseases, carcinogenesis, diabetes, and aging.[103,104] ROS classification includes both free radicals (i.e., $O_2\cdot^-$, $CO_3\cdot^-$, ·OOH, ·OH, ·OOR, and ·OR), and non-radical compounds (i.e., H_2O_2, $^1O_2$, HOCl, and O_3) among

which hydrogen peroxide (H_2O_2) is a major oxidant in living organisms. H_2O_2 produces hydroxyl radical, the most damaging ROS, through the Fenton or Fenton-like reaction (eq. 1).[104] This reaction could be the cause of toxicity for some transition metals including iron, the most abundant transition metal in the human body. In addition to Fe^{2+}, several other metal ions (Cu^{+} is probably the next most common ion, followed by Ni^{2+}, Co^{2+}, Ti^{3+}, Cr^{4+}, and Cr^{5+}) can drive the Fenton reaction in the absence of chelators, which can either inhibit or enhance the reaction.[105] Under stress conditions, the superoxide radical anion, a primary ROS product, reduces Fe^{3+} and subsequently releases Fe^{2+} ions from Fe-bound biological molecules (eq. 2) which can further participate in the Fenton reaction.[104]

$$M^{n+} + H_2O_2 \rightarrow M^{(n+1)+} + OH^- + \cdot OH \quad (1)$$

$$M^{(n+1)+} + O_2\cdot^- \rightarrow M^{n+} + O_2 \quad (2)$$

The metal ions are sequestered and stored in the cells such that their availability to generate ROS is minimal under normal conditions. The cells also have complex antioxidant regulatory systems to maintain appropriate ROS homeostasis. Despite this, disruption in proper ROS balance leading to oxidative stress and tissue injury still occurs.[106,107] Chelating drugs have been developed to prevent the excess of free metal ions and their associated toxicity. Among these chelators, desferrioxamine B and deferiprone are used as iron reducers (i.e., bind and remove iron from the bloodstream) in hemochromatosis and β-thalassemia,[108,109] while penicillamine and tetrathiomolybdate are used as copper reducers to treat Wilson's disease[110]. The copper depletion property of tetrathiomolybdate is also being explored in phase II clinical studies as a way to impair breast cancer metastasis.[111] Sulfur and selenium antioxidant complexes have been studied for the prevention of metal-mediated ROS formation and ultimately disease treatment or prevention.[107]

In this dissertation, three different aspects of metal ions in biology are addressed. First, Ni^{2+} ions have been shown to increase the efficacity of AMPs. All-atom molecular dynamics (MD) simulations are used to model the ability of ATCUN-Ni^{2+} piscidins 1 and 3 to insert and permeabilize lipid bilayers, which are mimics of the bacterial membrane. Due to the capability of the ATCUN-Ni^{2+} complex to oxidize lipids in membranes,[112] and the experimental evidence that these oxidation products are relevant for some bacteria,[113,114] lipid bilayer systems with and without oxidized phospholipids (oxPLs) have been considered in the current investigation. The study of piscidins could facilitate the understanding of the mechanism of action of other metallopeptides that share similar features and help to design novel therapeutics for antibiotic-resistant infections. Second, the effects of oxidative removal of Zn^{2+} (coinciding with the formation of disulfide bonds) from ZF proteins and the interactions of oxidized ZFs with nucleic acids are examined at the atomistic level. Targeting ZF proteins involved in the survival and progression of cancer cells or part of viral replication and transcription mechanisms serves as a promising strategy for cancer treatment or viral inhibition.[98,115–117] Disulfide bond formation induces significant conformational changes in the free protein that inhibit RNA binding. In the oxidized ZF-RNA complex, the loss of major hydrogen bonds important to RNA recognition may lead to the dissociation of the oxidized ZFs. Finally, the prevention of Fe^{2+}-mediated DNA damage by imidazole-based thiones and selones coordination is investigated through DFT studies of the free ligands and their complexes with Fe^{2+} coordinated to water and guanine. Metal coordination has been suggested as the primary mechanism of thiones/selones to prevent DNA damage.[118–121] Thus, protection is expected to occur through sacrificial oxidation of the coordinated thione/selone[122,123] rather than through the direct ROS scavenging observed for other sulfur and selenium compounds.[124–126]

Computational methods

To address the aforementioned research problems, molecular mechanics and quantum mechanics computational methods are used in this dissertation.

Molecular Mechanics (MM) is an inexpensive technique to compute the potential energy surface for arrangements of atoms using classical Newtonian mechanics. The potential energy of a chemical system in each conformation is approximated from the sum of the bonded (intramolecular) and nonbonded (intermolecular) terms (eq. 3-5).[127,128]

$$E_{total} = E_{bonded} + E_{nonbonded} \quad (3)$$

$$E_{bonded} = \sum_{bonds} k_r(r - r_{eq})^2 + \sum_{angles} k_\theta(\theta - \theta_{eq})^2 + \sum_{dihedrals} \frac{V_n}{2}(1 + \cos(n\phi - \gamma) \quad (4)$$

$$E_{nonbonded} = \sum_{i<j} \left[\frac{A_{ij}}{R_{ij}^{12}} - \frac{B_{ij}}{R_{ij}^{6}}\right] + \sum_{i<j} \left[\frac{q_i q_j}{\varepsilon R_{ij}}\right] \quad (5)$$

The bonded terms (eq. 4) include the bond stretching, angle bending, and dihedral energies, whereas the nonbonded interactions between all-atom pairs (eq. 5) include the van der Waals energy computed using the classical Lennard-Jones 6-12 potential,[129] and the electrostatic energy described by the Coulomb potential. Each atom in MM is represented by a particle with defined mass and radius, the chemical bonds between atoms are modeled as springs, and torsion angles are computed as an energy approximation between eclipsed and staggered conformations using a sinusoidal function. The bond stretching and angle bending terms each required a reference or equilibrium value (r_{eq} and θ_{eq}) and a force constant (k_r and k_θ). These parameters along with partial atomic charges (q_i and q_j) and van der Waals atomic radii need to be parameterized to fit quantum mechanical calculations and/or experimental data for better behavioral reproduction of real molecules in motion.[128] The collection of empirical parameters and the potential energy

function is described as a force field (FF). Numerous force fields have been developed over the years for different types of molecules (e.g., organics, biomolecules, inorganics) and many of them continue to be in use today including MM3,[130] MMFF,[131] OPLS,[132] AMBER,[133] and CHARMM[134].

In this dissertation, AMBER FFs are used to model metal-bound peptides (piscidins) and proteins (ZFs) in the presence of lipid mixtures and nucleic acids, respectively, to gain atomic-level insights into the importance of metal-binding to their specific mechanisms of action. The common FFs are designed for general organic molecules (e.g., *GAFF*),[135] and macromolecules such as proteins (e.g., *ff14SB*),[136] nucleic acids (e.g., *OL3*),[137] and lipids (e.g., *lipid17*)[138] that contain standard residues (e.g., the 20 amino acids and particular phospholipids only). None of these FFs are suitable for modeling non-standards residues such as oxPLs or metal-binding sites including the ATCUN-Ni^{2+} complex and Cys_2Hys_2-Zn^{2+} ZFs. Due to the multiple coordination modes of the transition metals and the numerous potential ligands, it becomes challenging to model metal complexes, especially if unique FFs are required for each metal complex.[139] Three main approaches have been developed to include metal ions into FFs (Figure 5).[140] The bonded model describes bonds, angles, and torsions between the metal ion and its ligating residues, and the van der Waals constituent of the nonbonded energy function (eq. 5).[141] The nonbonded model treats the interactions purely via electrostatic and Lennard-Jones terms placing integer charge on the metal ion.[142] The cationic dummy atoms model uses dummy atoms (cations) to mimic the valence electrons around the metal ion, and the interactions between the dummy atoms and ligands are described as in the nonbonded model.[143,144] Various variations and combinations of the three basic models exist, and multiple automated procedures for the generation of parameters for inorganic coordination chemistry have been developed over the years.[145–147]

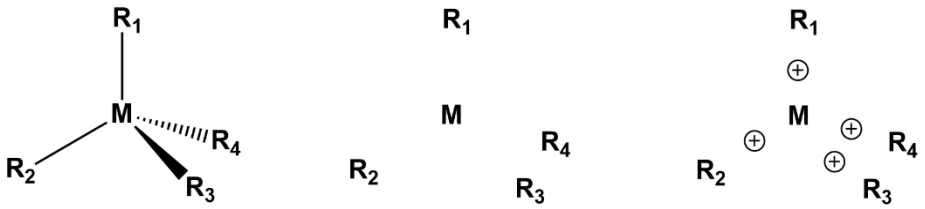

Figure 5. Schematic representations of three approaches that incorporate metals into MM force fields: (left) the bonded model, (middle) the nonbonded model, and (right) the cationic dummy atom model. Adapted with permission from reference [147].

The python-based Metal Center Parameter Builder (MCPB) computer program[139] was used to develop the FF parameters for the ATCUN-Ni^{2+} complex in this study. This program is based on the bonded plus electrostatic approach which fits perfectly with the form of other AMBER FFs (see eq. 4-6).[147] MCPB helps to derive parameters for metal sites from quantum mechanical calculations using (1) a smaller model to obtain the bond and angle parameters associated with the metal, and (2) a larger model to calculate the partial charges based on the restrained electrostatic potential.[139,147] To imitate the chemical environment at an affordable computational cost, the smaller model and the larger one were chosen to coincide for our system and includes the Ni^{2+} ion, the backbone atoms (C, O, N and H) of the first two ATCUN residues, and the backbone and side chain of His3 capped with NH-CH3 group. For the modeling of Cys_2Hys_2-Zn^{2+} ZFs, Zinc AMBER FF (ZAFF) was successfully applied. ZAFF is intended for the modeling of four-coordinated Zn metal centers and was developed with the release of the MCPB program, hence a bonded-based FF.[147] The MCPB based parameters were chosen for the metal-binding sites in the current study because (1) it has been widely and successfully used in

the literature,[148–152] and (2) other approaches (e.g., nonbonded model) have failed to maintain the proper geometry of the Cys_2Hys_2-Zn^{2+} site in test simulations.

The major application of MM force fields is in molecular dynamics (MD), a simulation-based approach that studies the temporal evolution (trajectory) of a set of interacting atoms by solving Newton's law

$$F_i = m_i a_i. \tag{6}$$

Here, m_i and a_i are the mass and acceleration, respectively, of the atom, and F_i is the force acting upon it. The force of an atom can also be computed as the energy derivative with respect to the change in the atom's position (eq. 7).

$$F_i = m_i a_i = -\frac{dE}{dr_i} \tag{7}$$

Thus, the position of each atom along a series of discrete time steps (e.g., 1 or 2 fs) can be determined by using the known atomic forces and masses. The velocities are calculated from the acceleration according to eq. 8, from which the positions are finally calculated (eq. 9)

$$a_i = \frac{dv_i}{dt} \tag{8}$$

$$v_i = \frac{dr_i}{dt} \tag{9}$$

In summary, at each step of this procedure, the forces acting on the atoms are computed and used with the current positions and velocities to generate new positions and velocities at the time step ahead. The atoms are then advanced to new positions and the dynamics cycle is reiterated.[153] To integrate these equations of motion, several numerical algorithms, such as the Leapfrog and Verlet algorithms, have been generated.

MD simulations are usually carried out on computer clusters or supercomputers making use of multiple parallel processors because of the billions of iterations required to generate the desired trajectories. Common MD packages may have the same name as their default force fields such as AMBER,[154] CHARMM,[134] and NAMD,[155] or lacking one on its own, support a variety of force fields, such as GROMACS[156] that has implemented AMBER, CHARMM, GROMOS, and OPLS force fields. Complex, dynamic processes occurring in biological systems can be investigated by performing MD simulations. Protein folding and stability under various conditions (pH, temperature, ionic strength), conformational changes, drug design, and molecular recognition between proteins, nucleic acids, membranes, or metal complexes are a few such applications.

MD simulations of ZF protein – RNA complexes provide insights into the conformational changes of the protein upon oxidation and their impact on the key protein-RNA interactions. The effect of oxidation on protein structure is evaluated by calculating root mean square (RMS) deviations, atomic RMS fluctuations, and radius of gyration profiles using CPPTRAJ,[157] the main AMBER program for trajectory processing. Additionally, statistical analysis is performed using the TimeScapes package.[158] The change in protein-RNA interactions is determined by tracking (non)native contacts and hydrogen bond analysis. MD simulations of free and Ni^{2+}-bound piscidin P1 and P3 in mixed lipid bilayer deliver atomic insights into the piscidin mode of action. Peptide-bilayer systems are assembled using the Membrane Builder module in CHARMM-GUI,[159] a popular tool to build lipid bilayers. Structural properties of the simulated bilayers, such as area per lipid, isothermal area compressibility modulus, lipid order, and bilayer thickness are determined using CPPTRAJ routines and in-house python and bash scripts. Peptide

position and orientation into the bilayer are described in terms of the tilt angle, azimuthal angle, and insertion depths.

Quantum Mechanics (QM) was developed as a new mechanics required to describe a microscopic system of dual nature (wavelike and particle-like properties). The fundamental postulate of QM is that the operators acting upon a wave function (Ψ), which exists for any chemical system return the observable properties of the system. The system energy (E) is returned as an eigenvalue by the Hamiltonian operator (H) and gives the Schrödinger equation: $H\Psi = E\Psi$. The Hamiltonian depends on both the positions and nuclei atomic numbers, and the total numbers of electrons. Density functional theory (DFT) evolved as a new method of obtaining a more accurate approximate solution to the Schrödinger equation for a many-body system without referencing a wave function. The first attempt to define a DFT used Thomas-Fermi equations in combination with an assumed variational principle. DFT emerged as a valid quantum chemical methodology when the Hohenberg-Kohn existence and variational theorems were defined. According to these theorems, the structural and electronic properties of many-body systems can be described by using functionals of the electron density. As DFT functionals and computer power have improved, the applications of DFT in areas of material science, computational physics, and chemistry have been growing in the last few decades.

In this dissertation, DFT geometry optimizations are performed on free ligands and their complexes with Fe(II) coordinated to water and guanine using the mPW1PW91 exchange-correlation functional[160,161]. The trends in the zwitterionic properties of the free ligand and their correlation with the complex stability are estimated by calculation of the Wiberg bond indices (WBIs)[162] and Natural Population Analysis (NPA) charges using Natural Bond Orbital (NBO) analysis[163] as implemented in the Gaussian 09 software package[164]. Wiberg bond order measures

the electron population overlap between two atoms. NBO analysis serves as a method to analyze hybridizations and covalency effects in polyatomic molecules. In NBO, the original basis set goes through a series of transformations to various localized basis sets: natural atomic orbitals, hybrid orbitals, bond orbitals, and localized molecular orbitals.[163]

In summary, the goal of this dissertation is to rationalize the role of metal ions in varying aspects of cell life using MD simulations and DFT calculations by characterizing the atomic changes upon addition or removal of metal ions, and the possible mechanism of protection in case of dyshomeostasis. The dissertation is divided into three chapters:

- Chapter 2 discusses the effect of metal binding and oxidized lipids incorporation on the membrane activity of piscidin 1 and 3
- Chapter 3 addresses the conformational changes of free and RNA-bound ZFs upon removal of metal ion
- Chapter 4 estimates the prevention of metal-mediated DNA damage by thione/selone compounds through DFT calculations.

CHAPTER II

THE EFFECT OF METAL BINDING AND OXIDIZED LIPIDS INCORPORATION ON THE MEMBRANE ACTIVITY OF ANTIMICROBIAL PEPTIDES

Introduction

Antibiotic-resistant infections (ARIs) affect 2.8 million Americans annually and claim more than 35,000 lives according to the 2019 CDC's Antibiotic Resistance Threats report.[165] ARIs are particularly dangerous for infection-prone patients such as those with chronic conditions or receiving chemotherapy, dialysis treatment, or an organ transplant. Due to the lack of effective drugs, tens of billions of dollars are spent each year on excess healthcare costs.[165,166] Despite the effort to reduce infection and death related to ARIs, the spread of new resistance forms and the number of antibiotic-resistant patients remain high. Increased risk of ARIs is of great concern because their spread is challenging to identify and contain, which jeopardizes the patients. More work is required to treat high-risk patients and develop novel therapeutics with low induction of bacterial resistance. Without urgent action, the estimated global death because of multi-drug resistance could reach 10 million by 2050.[167]

Antimicrobial peptides (AMPs) are promising alternatives to conventional antibiotics because they are considered safe, unlikely to induce bacterial resistance, and have a low risk of accumulation in tissue. AMPs are a diverse group of synthetically designed or naturally occurring peptides that contribute to natural immune responses.[168] The AMP Database contains over three thousand AMPs, most of which are cationic and have fewer than fifty amino acids.[169] AMPs can be classified into four classes based on their secondary structure: α-helical, β-sheet,

loop, and extended peptides, with most of them belonging to the first two categories.[170–173] α-Helical AMPs are unstructured in aqueous solutions but develop an amphipathic helical structure in the presence of membranes or organic solvents.[168,174,175] β-Sheet AMPs, which have a more defined structure in solution, do not experience significant conformational changes upon interaction with the bacterial membranes.[169,170] The first AMP to be identified was gramicidin which was isolated from a soil gram-positive bacterial strain of *Bacillus brevis* in 1939 and shown to be active against gram-positive bacteria.[176–178] Subsequently, numerous AMPs have been discovered and characterized.[179] In 1956, the first animal AMP, phagocytin, was isolated from rabbit leucocytes.[180] The research interest in these peptides really began to grow with the isolation of defensins and cathelicidins from mammals in the 1980s. The former display antibacterial, antiviral, and antifungal activities via diverse modes of action.[181,182] Over time many AMPs have been discovered, many of which are used as therapeutics in the market or are under clinical trials.[171]

AMPs inactivate invading pathogens rapidly and non-specifically. The AMPs containing cationic residues bind with high affinity to the surfaces of bacterial membranes which are rich in anionic phospholipids. The mammalian cell membranes on the other hand consist of zwitterionic phospholipids and interact with low affinity with the AMPs. The electrostatic interactions of AMPs with the bacterial membrane surface disrupt the membrane integrity yielding to leakage of the cell content and eventually, cell death.[168,170] Few mechanisms for membrane disruption, including the barrel-stave, toroidal pore, and carpet model (Figure 6), have been proposed and are based on experiments with model membranes.[171,183,184] These modes of action are not mutually-exclusive, and AMPs can combine multiple mechanisms to kill their targets. Additionally, AMPs may achieve membrane permeabilization by decreasing/increasing the

membrane thickness, clustering the phospholipid headgroups, or translocating the membrane and targeting specific intracellular molecules or processes.[185–187] The latter is known as a non-membrane disruptive pathway to kill foreign microbes. The chosen mode(s) of action may depend on parameters such as species and tissue localization of the target pathogen, or local environment and concentration of the peptide.[170,184,188] In addition to broad-spectrum antibacterial and antifungal activity, many have complex immunomodulatory functions and synergistic interactions with conventional antibiotics.[171] These properties offer AMPs a great advantage over traditional antibiotics in the fight against infectious diseases. So far, five naturally occurring AMPs have been approved for clinical use as an alternative to antibiotics due to their antimicrobial potency.[168] Moreover, their cationic analogs constitute the bulk of hundreds of AMPs that are under clinical evaluation. Several peptides failed to display increased efficacy over conventional treatment, and/or presented pharmacokinetics and safety concerns which resulted in the discontinuation of their clinical studies.[168] However, an analysis carried out by Lau et al. on all peptides from human clinical trials revealed that peptides are more successful than small-molecule drugs regardless of the clinical study's stage.[189]

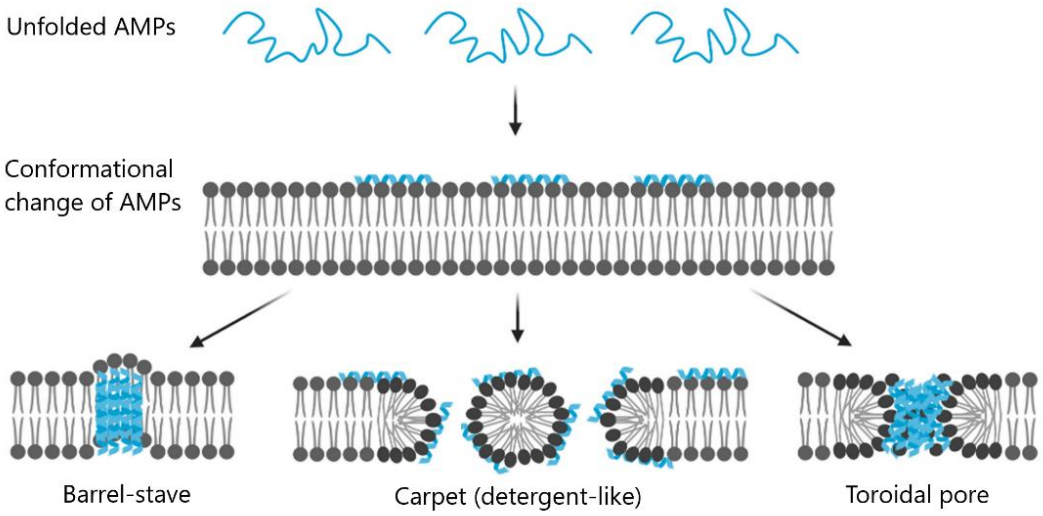

Figure 6. Models of membrane disruption by AMPs. Adapted from reference [168].

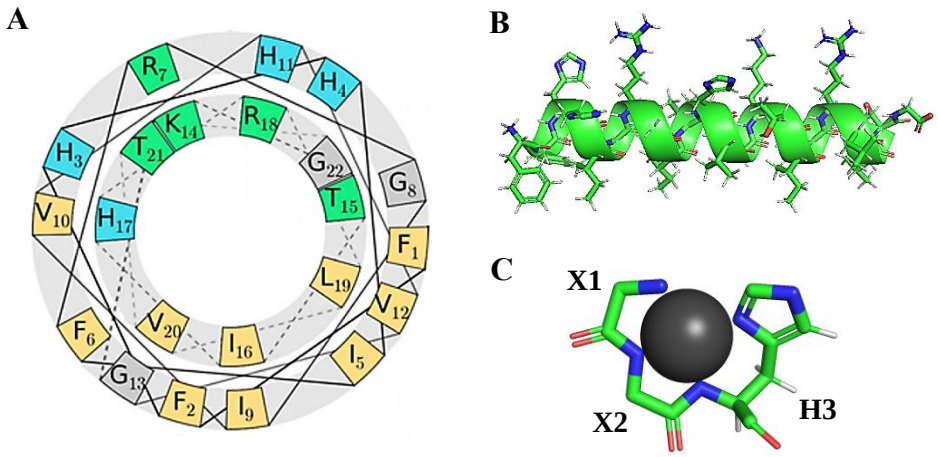

Figure 7. Selective structural representations of the piscidins included in the current study. (A) Color-coded helical wheel of P1 adapted with permission from reference [190]. The more polar residues are colored in green, while the hydrophobic ones are in yellow. His and Gly residues are indicated in blue and gray, respectively. (B) P3 secondary structure with the side chains widely extended. (C) The ATCUN-Ni^{2+} motif.

Piscidins, the α-helical AMPs residing in the mast cells of fish,[191] were shown to efficiently kill bacteria within minutes by targeting their membrane instead of specific cellular targets.[192] As with other AMPs, they function by permeating and weakening the membrane in a concentration-dependent manner.[193,194] Piscidins are believed to bind to the bacterial membrane first, a process driven both by electrostatic and hydrophobic interactions. The amphipathic structure of the peptides allows them to insert into the bacterial membrane and induce changes in the membrane structure and organization. These modifications lead to membrane permeabilization and eventual bacterial death.[195–197] Piscidin 1 (P1, FFHHIFRGIVHVGKTIHRLVTG) and piscidin 3 (P3, FIHHIFRGIVHAGRSIGRFLTG) are naturally occurring isoforms discovered in mast cells of hybrid striped sea bass.[191,198] These broadly studied peptides assume an amphipathic, α-helical structure (Figure 7) in the presence of membranes to maximize their interactions with phospholipids. P1 and P3 have 22 residues and share 68% sequence identity including three histidine residues (H3, H4, and H11).[192] The histidine (His) residues are important for metal-binding and attraction to the cell membrane.[190,196] P1, with an additional His in position 17 (H17), is one of the most potent AMPs and is also effective against cancer and HIV.[192,199–202] P3, the less hemolytic isoform, has a nuclease activity against bacterial DNA but display a lower rate of killing bacteria (1h vs minutes).[192,195] Neutron diffraction and MD revealed that P1 inserts into the membrane through its C-terminal end, the hydrophilic extremity carrying H17, whereas P3 directs its N-terminal end toward the bilayer interior.[190] Additionally, the histidines of P1 insert more deeply into the lipid bilayer than those of P3 as shown by computational modeling.[196]

Piscidins' antimicrobial potency has been attributed to the atypically large number of His residues in such a short peptide and an Amino Terminal Cu(II)- and Ni(II)- binding (ATCUN)

motif of consensus sequence XXH at the N-terminal end of the peptide (Figure 7C).[75,78,203] This motif is not the same for the two isoforms (FFH- for P1 vs FIH- for P3) but both bind Cu^{2+} and Ni^{2+} ions with high affinity. Formation of the bulky ATCUN-Cu^{2+}/Ni^{2+} complex upon metal binding to the ATCUN motif (metallation) is believed to lower the overall charge of piscidin by 1 through deprotonation of the N-terminal ammonium group (coordination of the +2-metal ion is countered by the loss of the F2 and H3 backbone hydrogens). This net loss of charge could explain the increase in antimicrobial capacity.[73,204] Experimentally, the effect of metallation was tested using dye leakage assays, a standard experiment for measuring the extent of damage induced by external agents (i.e., piscidins) on synthetic lipid vesicles (bacteria mimics).[190] Metallated P1 showed a five-fold increase in permeabilization effectiveness measured in terms of peptide concentration required to induce leakage in 50% of the vesicles (EC_{50}).[205]

Additionally, metallation creates a favorable local environment for the formation of reactive oxygen species (ROS) that can chemically damage biological molecules including the unsaturated fatty acid chains of the membrane lipids.[206–208] Bacterial membranes mainly contain saturated and monounsaturated phospholipids which do not easily undergo oxidative damage under normal conditions. But some bacteria were discovered to integrate easily oxidized exogenous polyunsaturated fatty acid in their membrane to escape antimicrobial agents through changes in membrane structure, biofilm formation, and motility.[114,209,210] The conditions that enable membrane-disruptive interactions of metallopeptides with bacteria (e.g., labile copper ions and ROS formation) are believed to be relevant *in vivo* as well.[205] Oxidation of the phospholipids by ROS can damage the bulk properties of the membrane (by e.g., increasing the water content or passive permeability).[207,211,212] The ROS-mediated oxidized phospholipids (oxPLs) have a shortened acyl chain functionalized with aldehyde or hydroperoxyl groups.

Moreover, few AMPs (e.g., indolicidin) were shown to exhibit increased interactions with bilayers containing aldehyde-functionalized oxPLs suggesting that this type of oxPLs may represent a novel molecular target of other AMPs including piscidin.[206,213]

Previously, MD simulations of P1 and P3 in binary lipid mixtures relevant to bacterial membranes (e.g., POPC/POPG and POPE/POPG, where POPC: 1-palmitoyl-2-oleoyl-sn-glycero-3-phosphocholine, POPG: 1-palmitoyl-2-oleoyl-sn-glycero-3-phosphoglycerol, and POPE: 1-palmitoyl-2-oleoyl-sn-glycero-3-phosphoethanolamine, Figure 8A) have been carried out to investigate (1) the effects of lipid composition on the surface-bound state of the peptides, (2) the mechanism of membrane disruption, and (3) the structure and orientation of the peptides in the bilayer.[190,196,214,215] These studies have found that the two piscidins have distinct bilayer orientations and insertion modalities (N- vs C-termini) which are dependent on the lipid composition.[190,196,214] Additionally, P1 was suggested to prefer surface defects over pore formation as its mode of action.[215] However, P1 and P3 bound to oxPLs-containing bilayers, or metal-bound P1 and P3 in any lipid bilayers have not been characterized at the atomic level.

This study focuses on P1 and P3 and their capability to bind metal ions to enhance their membrane disruptive effects. MD simulations were performed on both metallated and apo P1 and P3 in 3:1 POPC/POPG and 2.6:1:0.4 POPC/POPG/aldo-PC bilayers (where aldo-PC: 1-palmitoyl-2-(9′-oxo-nonanoyl)-sn-glycero-3-phosphocholine, Figure 8). The first lipid mixture, a well-accepted mimic of the bacterial membrane, was used to investigate how metallation alone influences the bilayer structural parameters and the ability of piscidins to insert into the membrane. The tertiary lipid mixture was utilized to study whether aldo-PC influences the insertion depths and the topology that the piscidins adopt in the bilayer, as well as to determine any aldo-PC-induced structural membrane changes. This study uses 10% aldo-PC because it has

been suggested to be physiologically relevant under oxidative stress.[216,217] In addition, studying piscidins could be useful for understanding the mechanisms of other AMPs and metallopeptides that share common features including the development of secondary structures upon membrane binding. The information gathered from this study may help design novel therapeutics for antibiotic-resistant infections.

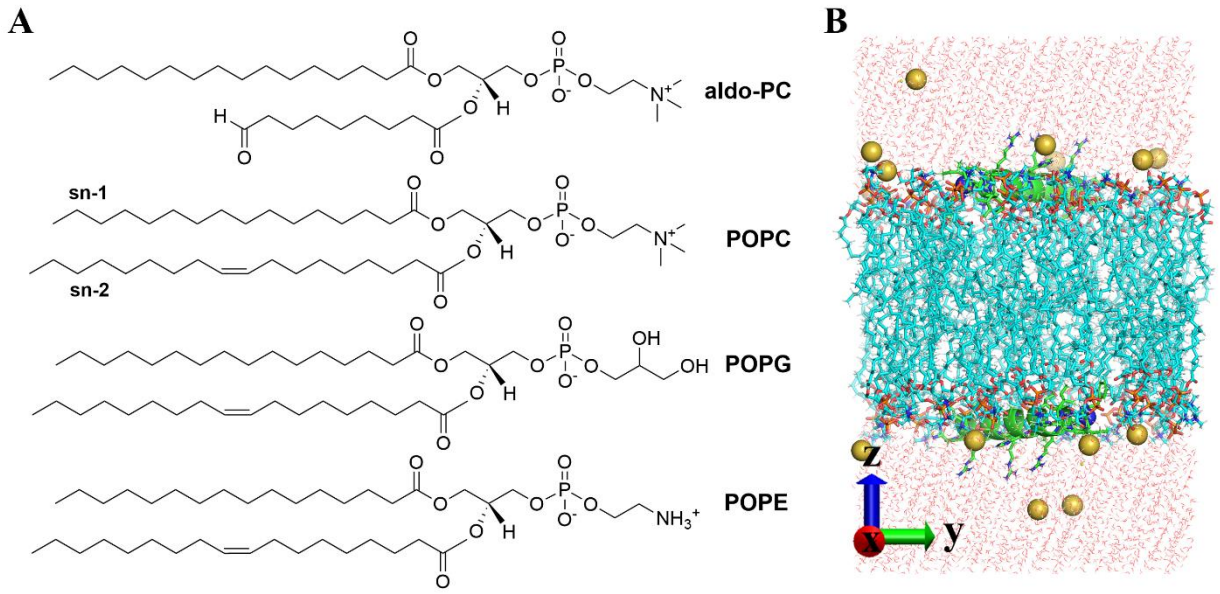

Figure 8. (A) Structures of phospholipids of interest. Aldo-PC: 1-palmitoyl-2-(9′-oxo-nonanoyl)-sn-glycero-3-phosphocholine, POPC: 1-palmitoyl-2-oleoyl-sn-glycero-3-phosphocholine, POPG: 1-palmitoyl-2-oleoyl-sn-glycero-3-phosphoglycerol, and POPE: POPE: 1-palmitoyl-2-oleoyl-sn-glycero-3-phosphoethanolamine. (B) Representative input structure for the MD simulations of piscidins in mixed lipid bilayers. Peptides are represented as green ribbons and licorices; the phospholipids and water atoms are depicted as licorices and lines, respectively, colored as follows: carbon – cyan, oxygen – red, nitrogen – blue, and hydrogen – light gray. Sodium ions are represented as orange spheres.

Computational Methods

MD simulations were performed on apo and Ni^{2+}-bound P1 and P3 in 3:1 POPC/POPG and 2.6:1:0.4 POPC/POPG/aldo-PC lipid bilayers with a ratio of one peptide per 40 lipids in each leaflet of the bilayer (P/L = 1:40) using the AMBER18 software package[218]. Peptide-bilayer systems were assembled using the Membrane Builder module within the CHARMM-GUI interface.[159,219] Initial peptide structures were generated as previously described for free piscidins.[196] Briefly, α-helical peptides with extended sidechains were generated. The center of mass (COM) of the heavy backbone atoms of one peptide was aligned ~20 Å above the center of the bilayer, while a second peptide was placed ~20 Å below the center of the bilayer. Each peptide was rotated along its helical axis to assure that hydrophobic residues were facing the bilayer interior. Each system contains a 16 Å water layer above each leaflet (~56 waters/lipid), 15-20 sodium ions, and chloride ions to neutralize the models and add a slight salt concentration. Simulations were performed using the AMBER *ff14SB* protein force field[136] and the Lipid17 force field.[138] The force field for the oxidized lipid acyl chain containing an aldehyde functional group was obtained using the Antechamber package[220]. The ATCUN-Ni^{2+} parameters were generated using the python-based Metal Binding Protein Builder (MCPB) module[139] in AmberTools, which is a well-established tool for metal site parameterization. Peptides were modeled with neutral histidine side chains according to previously reported pKa values.[190] Solvent and counterions used the TIP3P water model[221] with Joung and Cheatham monovalent ions parameters[222]. MD simulations of apo P1 and P3 in POPC/POPG were performed for comparison to the previous MD simulations in CHARMM.[190,196,214] Simulations for peptide-free

bilayers (3:1 POPC/POPG and 2.6:1:0.4 POPC/POPG/aldo-PC) were performed to estimate the peptide-induced changes to the membrane.

Models were prepared for production simulations by initial minimization followed by heating from 0 to 313K in four stages using the Langevin thermostat for a total of 150 ps. Constant volume and weak restraints (force constants of 100 and 10 kcal mol^{-1} $Å^{-2}$ on peptides and lipids, respectively) were applied during the first stage (0 K to 100 K). The remainder of the heating (from 100 K to 200 K (2), 200 K to 250 K (3), and 250 K to 313 K (4)) was conducted under constant pressure using semi-anisotropic Berendsen regulation with a relaxation time of 2 ps. Production runs were performed at constant pressure (1 atm) and temperature (313 K) in a monoclinic periodic box with zero surface tension using the PMEMD implementation[223] of AMBER 18. SHAKE constraints were applied to bonds to hydrogen atoms. Electrostatic interactions were treated with the particle mesh Ewald method (cutoff = 10 Å). Since peptide-induced defect formation is on the microsecond time scale, the MD simulations were performed for at least 2 μs with a 1 fs time step, which was preceded by a 100 ns equilibration run. Analyses performed using the AmberTools CPPTRAJ routines[157] and Python scripts were averaged over duplicate simulations.

Area per lipid, volume per lipid, isothermal compressibility modulus, and bilayer thickness were averaged over the 2.0 μs simulations (Tables 1 and 3). The area per lipid parameter, defined as the average area each phospholipid occupies in the x- and y- plane (containing the headgroups, Figure 8B), indicates whether the bilayer is in the correct phase (i.e., liquid crystalline or gel phase). Area per lipid (A_L) can easily be computed from MD simulations using the box dimensions according to eq. 10 where L_x and L_y are the x- and y- dimensions of the simulation box, respectively, and m_{lipid} is the number of lipids per leaflet.[224]

$$A_L = \frac{L_x \times L_y}{m_{lipid}} \quad (10)$$

Theoretical values were compared to the experimentally derived ones, but the experimental data often depend on the technique used for the measurement and display a high degree of uncertainty. Volume per lipid (V_L) was calculated according to eq. 11, where V_{box} is the volume of the simulation box, n_w is the number of water molecules, V_w is the volume of a water molecule and n_{lipid} is the total number of lipids in the bilayer.[224] The volume of a TIP3P water molecule was previously determined to be 30.53 Å^3.[225]

$$V_L = \frac{V_{box} - n_w V_w}{n_{lipid}} \quad (11)$$

The isothermal area expansion (compressibility) modulus, K_A, was computed from the variation in the area per lipid using eq. 12, where k_B is Boltzmann's constant, T is temperature, $\langle A_L \rangle$ is the average area per lipid and σ_A^2 is the variance in the area per lipid.[224]

$$K_A = \frac{2k_B T \langle A_L \rangle}{n_{lipid} \sigma_A{}^2} \quad (12)$$

K_A values are indicative of the peptide-induced changes to the fluidity of the bilayer. Using the Berendsen method for pressure coupling, we calculated a K_A value for the peptide-free bilayer that was within the experimentally obtained range. The average electron density profiles for all five systems were calculated over 2 μs and decomposed into contributions from the following groups: phosphate (PO_4), methylenes (CH_2), terminal methyls (CH_3), and peptide backbone (pepBB) using CPPTRAJ (Figure 9 and 17). The headgroup-to-headgroup (h(P-P)) and hydrophobic (h(C2-C2), where C2 is from the sn-2 chain, Figure 8A) bilayer thicknesses were computed using the peak-to-peak distance in the phosphate (purple) and methylene (gray) decomposed electron density profiles, respectively. Deuterium order parameters (S_{CD}) of the

carbons in the acyl chains, were calculated according to eq. 13 for the bilayer alone and those with piscidins.

$$S_{CD} = \frac{1}{2}\langle 3\cos^2\theta - 1\rangle \quad (13)$$

S_{CD} reflects the chain mobility at a single carbon position and is a measure of the relative orientation of C-D bonds about the z-axis. In equation 13, θ is the angle between the C-H (only experimental measurements require deuterium, and H atoms have been used in the simulations) vector and bilayer normal (z-axis), such that an S_{CD} value of 1 infers a parallel position and S_{CD}=0 suggests total arbitrary motion.

The tilt (τ), and azimuthal rotational (ρ) angles were computed at 10 ns intervals relative to a reference structure with φ/ψ angles of -61°/-45° and zero Euler angles. Peptide insertion depths (z) were calculated as the distance between the center of mass (COM) of the peptide heavy backbone atoms and the plane of the phosphorous atoms of the lipid headgroups. τ, ρ and z were calculated separately for the N-terminal (residues 5-10) and C-terminal (residues 14-20) ends because of the previously reported kinking at G13, the fraying of terminal residues[196] and the complexation of the N-terminus with Ni(II).

Results and Discussion

MD simulations of piscidins in POPC/POPG bilayers

MD simulations were performed on peptide-free, P1- and P3-bound 3:1 POPC/POPG/ bilayers for comparison with previous MD simulations carried out in CHARMM.[214] Generally, the results in this study are consistent with the CHARMM simulations.[214] The area and volume per lipid (A_L and V_L, respectively), as well as the compressibility modulus (K_A) for the

POPC/POPG bilayer alone, are in good agreement with the experimental values of a single component bilayer suggesting that the system is well equilibrated in its liquid phase (Table 1). The headgroup-to-headgroup (h(P-P)) and hydrophobic thicknesses (h(C2-C2)) computed from the respective electron density profiles (Figure 9) are listed in Table 1. H(P-P) and h(C2-C2) differ by ~10 Å. The absolute thickness values were shown to be different between the AMBER and CHARMM force fields (i.e., h(P-P) ~37.5 Å and ~39.0 Å, respectively),[226] but they both follow similar trends (i.e., the difference between h(P-P) and h(C2-C2)).

Table 1. Average structural properties over two trials of the POPC/POPG bilayer system simulations, where V_L is volume per lipid, A_L - area per lipid, K_A - isothermal area expansion modulus, h(P-P) – headgroup-to-headgroup thickness and h(C2-C2) – hydrophobic thickness

POPC/POPG	V_L (Å^3)	A_L (Å^2)	K_A (mNm^{-1})	h(P–P) (Å)	h(C2–C2) (Å)
Exp	*1256**[227] *1265*[§228]	*64.3*,* *65.3*[§228]	*180-330*[¥229]	*37.0**[227] *36.0*[§228]	
MD	1206 ± 0	*68.3**[227] 67.1 ± 0.4	254 ± 114	37.5 ± 0.2	27.4 ± 0.2
+ P1	1290 ± 0	72.1 ± 0.5	208 ± 87	37.3 ± 0.4	27.4 ± 0.4
+ P3	1287 ± 1	71.8 ± 0.6	218 ± 120	37.2 ± 0.3	27.3 ± 0.4
+ P1-Ni^{2+}	1290 ± 0	71.9 ± 0.4	202 ± 98	37.4 ± 0.3	27.5 ± 0.3
+ P3-Ni^{2+}	1286 ± 0	71.4 ± 0.4	250 ± 98	37.5 ± 0.3	27.6 ± 0.3

The experimental value for pure POPC at (¥) 298 K, (*) 303 K and (§) 313 K

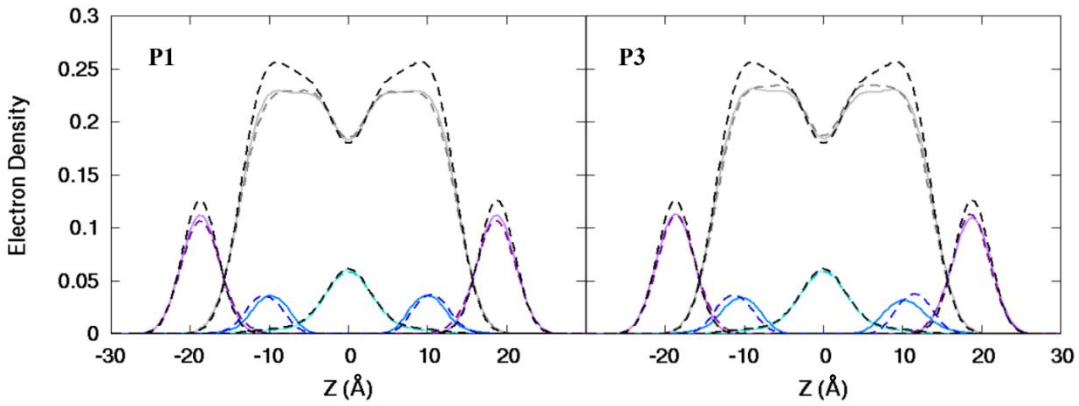

Figure 9. Electron density profiles for P1 and P3 in POPC/POPG. Profiles are shown for the phosphates (purple), peptides (blue), CH_2 acyl chains (gray), and terminal CH_3 (cyan). Electron density profiles containing membrane and apo or metallated piscidin are in darker dashed or solid lines, respectively, whereas the bilayer-only systems are in dashed black lines.

Backbone heavy-atom RMSDs for the first 20 residues of P1 and P3 with respect to the first equilibrated structures suggest that P3 is slightly more flexible than P1 (RMSD = 0.98 Å vs 0.80 Å for P3 and P1, respectively). The orientation of each peptide, which maintained the α-helical structure throughout the simulations (Figure 10A, B), is described by the tilt (τ) and azimuthal rotational angles (ρ, Figures 11 and A1, Table 2). The average orientation of the N-terminal end for apo piscidins is slightly toward the headgroups registering τ values of 95°, whereas the C-terminal ends are parallel to the surface. In the experimental studies,[196] ρ rather than τ is the most relevant for distinguishing between P1 from P3. While P1 and P3 display similar ρ_C values, the ρ_N of the latter is smaller (248° vs 261°), which means that the P3 N-terminal end does not distribute the hydrophobic and hydrophilic residues evenly in the membrane. Similar orientations and kinked structures have been previously reported for P1 and P3 in DMPC/DMPG and POPE/POPG bilayers ($\Delta\tau$ ~6-8° and $\Delta\rho$ ~15-20°).[196] The peptide

backbones for P1 and P3 are on average ~7-8 Å below the P atoms and just under the C2 atoms of the lipids sn-2 acyl chain (Table 2). P1 inserts slightly deeper in the bilayer than P3 but both experience similar differences in the z_N and z_C values ($\Delta z \sim 0.1$ Å) within the isoform.

Table 2. Tilt angles τ (°), azimuthal rotation angles ρ (°) and depths of insertion z (Å) for the backbone atoms of N- (residues 5−10) and C- (residues 14−20) helical segments of each peptide in POPC/POPG averaged over two trials. Insertion depth for the backbone atoms of the full-length peptide ($z_{1\text{-}22}$) is also reported

	τ_N	τ_C	$\Delta\tau = (\tau_N - \tau_C)$	
P1	95 ± 1	88 ± 1	7.5 ± 1	
P3	95 ± 1	89 ± 1	6.1 ± 0	
P1-Ni^{2+}	90 ± 1	83 ± 1	7.0 ± 1	
P3-Ni^{2+}	86 ± 2	82 ± 2	4.0 ± 1	
	ρ_N	ρ_C	$\Delta\rho = (\rho_N - \rho_C)$	
P1	261 ± 2	241 ± 1	19.5 ± 1	
P3	248 ± 1	233 ± 2	15.3 ± 0	
P1-Ni^{2+}	251 ± 1	235 ± 1	16.0 ± 1	
P3-Ni^{2+}	237 ± 1	224 ± 1	12.7 ± 1	
	z_N	z_C	$\Delta z = (z_N - z_C)$	$z_{1\text{-}22}$
P1	-8.2 ± 0.2	-8.3 ± 0.3	0.1 ± 0.2	-7.8 ± 0.3
P3	-7.4 ± 0.1	-7.5 ± 0.3	0.1 ± 0.2	-7.0 ± 0.2
P1-Ni^{2+}	-9.1 ± 0.2	-8.0 ± 0.3	-1.2 ± 0.1	-8.2 ± 0.2
P3-Ni^{2+}	-9.1 ± 0.4	-7.1 ± 0.2	-2.0 ± 0.5	-7.9 ± 0.2

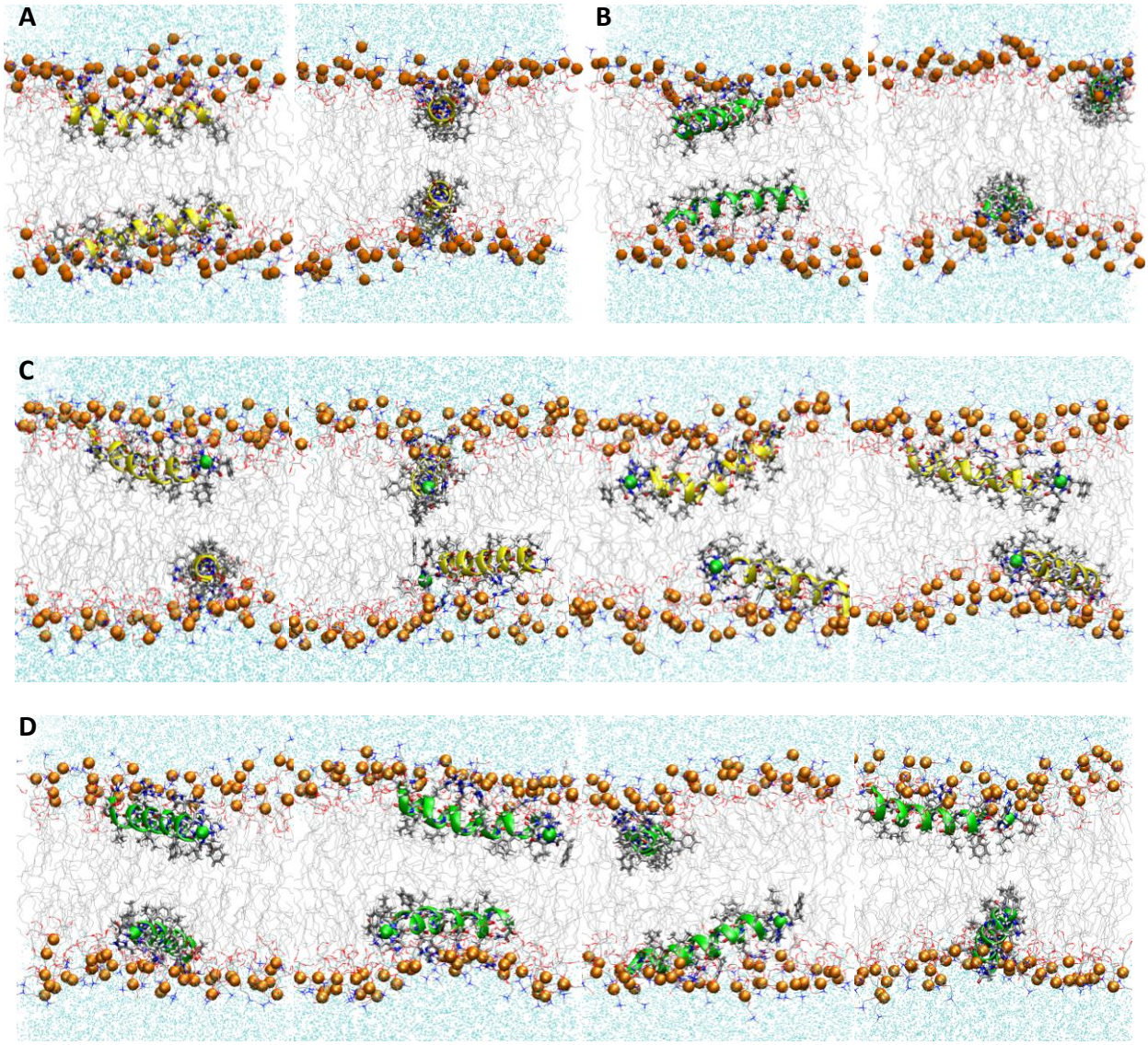

Figure 10. Snapshots from MD simulations of (A) P1, (B) P3, (C) P1:Ni^{2+}, and (D) P3:Ni^{2+} in POPC/POPG. Peptides are represented as yellow (P1 isoforms) or green (P3 isoforms) ribbons and licorice. Phosphorous atoms are depicted as orange spheres while the rest of phospholipids atoms except hydrogen are depicted as lines colored as follows: carbon – gray, oxygen – red, and nitrogen – blue. Water molecules are represented as cyan points.

The presence of piscidins in the bilayer reduces the height of CH_2 and PO_4 density peaks, and asymmetrically widens the PO_4 density peaks in both the current and previous simulations (Figure 9).[214] A decrease in the electron density for the bilayer components are expected when other molecules are embedded in the bilayer. As these molecules move deeper into the bilayer, they may pull in certain groups (i.e., PO_4) causing an asymmetric widening of their density peaks. Also, the insertion of apo peptides induces minimal P-P thinning and has little to no effect on the C2-C2 thickness of the membrane (Table 1). In contrast, P1 and P3 reduced h(C2-C2) by 1.0 Å and 1.4 Å, respectively in the CHARMM simulations. The standard errors calculated for these values (1.3-1.4 Å) suggest that the peptides cause large variation in the hydrophobic thickness of the membrane including possible thickening. Additionally, the results of membrane-bound AMP simulations depend on the force field parameters suggesting that slightly different results may be obtained and that researchers should take care in method selection.[230] As noted previously,[214] an increase in A_L and $V_{L,}$ and a reduction in K_A are observed with the addition of piscidins due to their interactions with the phospholipid headgroups and upper chain regions. A similar inability of acyl chains to pack relatively tightly together (lower K_A) was observed in the MD simulations of fentanyl, an opioid analgesic, in a 1,2-dioleoyl-sn-glycero-phosphocholine (DOPC) bilayer.[231] The A_L expansions agree with the results published by Perrin et al (V_L data has not been reported), but opposite K_A changes in response to the two piscidins were reported (P1 increases the K_A and P3 decreases it).[214] Altogether the membrane structural parameters for the bilayer alone are in agreement with the experimental data, and the peptide-induced changes noted in the current simulations are comparable with previous results.

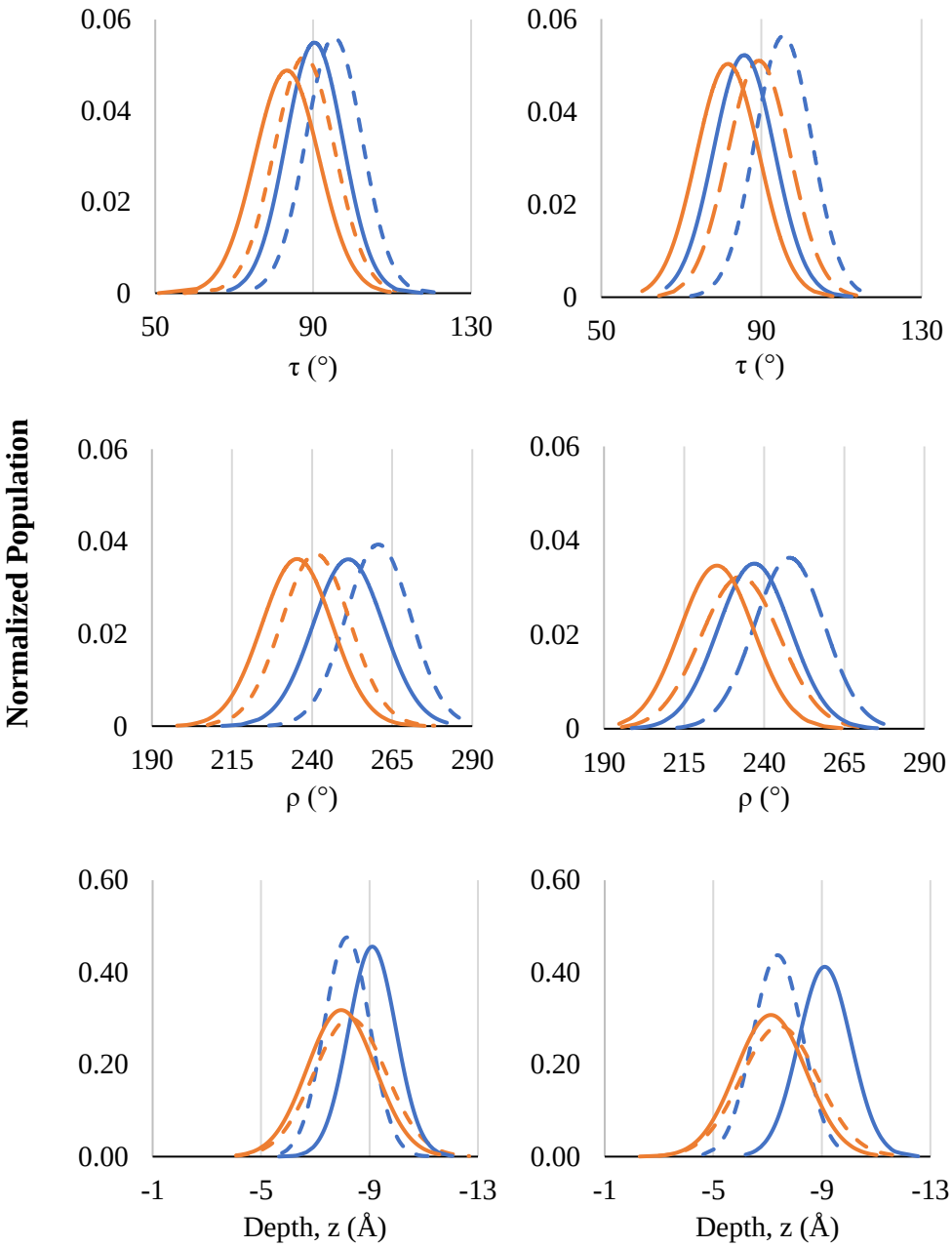

Figure 11. Distribution of tilt angles (τ), azimuthal rotation angles (ρ), and depths of insertion sampled by the N- (blue) or C- (orange) terminal residues of P1 (left) or P3 (right) in POPC/POPG during the 2-μs MD simulations. Curves for apo and metallated piscidins are shown as dashed and solid lines, respectively.

All-atom MD simulations of the metallated P1 and P3 in the 3:1 POPC/POPG bilayer showed that both piscidins are dynamic in the membrane as suggested by the backbone heavy-atom RMSDs for the first 20 residues of P1:Ni^{2+} and P3:Ni^{2+} (RMSD = 1.07 Å and 1.13 Å for P1:Ni^{2+} and P3:Ni^{2+}, respectively). The ATCUN residues have low RMSDs (0.19 Å and 0.22 Å for P1:$Ni^{2+}$and P3:Ni^{2+}, respectively) similar to experimental values (*M.L. Cotten, personal communication*). Examination of the MD trajectories confirmed that the metal-bound peptides are embedded in the bilayer below the lipid phosphate plane and remained predominately α-helical with the hydrophilic residues oriented toward the water-bilayer interface, similar to the apo peptides in the current and previous studies[196]. The sidechains of Arg and Lys were well-extended to preferentially interact with the negatively charged PG headgroups (Figure 10C, D).

The aromatic sidechains of the ATCUN motif and the adjacent residues have been proposed to stabilize the Ni^{2+} ion through cation-π interactions and aid the insertion of the metal-bound N-termini into the bilayer.[232] Figure 12 shows the superposition of the ATCUN motif and H4 residue for snapshots of P1:Ni^{2+} taken over 200 ns interval along the MD trajectory. While the center of mass of F2 is positioned ~6.5 Å from the nickel center for 96% of the trajectories, the aromatic groups of F1 and H4 make close contacts (~5.2 Å for 59% and ~4.2 Å for 94% of frames, respectively) that are within the range expected for cation-π interactions.[233,234] For 4% of frames, the F1 phenyl group makes a much closer 4.0 Å contact. The longer distances for F2 and F1 (~6.3 for 37% of frames) occur when their sidechains protrude into the lipid bilayer. The H4 imidazole faces the headgroup region of the bilayer and forms a cation-π interaction or fills a fifth coordination site on Ni^{2+} through its δ-nitrogen. Similar interactions and average distances were observed between Ni^{2+} and the sidechain of F1 and H4 in P3:Ni^{2+}. Although these results contrast with previous gas-phase DFT calculations that suggest a cation-π interaction with F2,[232]

they confirm the potential for the metal center to be partially shielded by aromatic sidechains. The role of F1 and not F2 in forming cation-π interactions with the Ni^{2+} ion is consistent with the lack of change in the insertion depth of the N-terminal end (z_N ~ 9.1 Å) when F2 (in P1:Ni^{2+}) is replaced by I2 (in P3:Ni^{2+}).

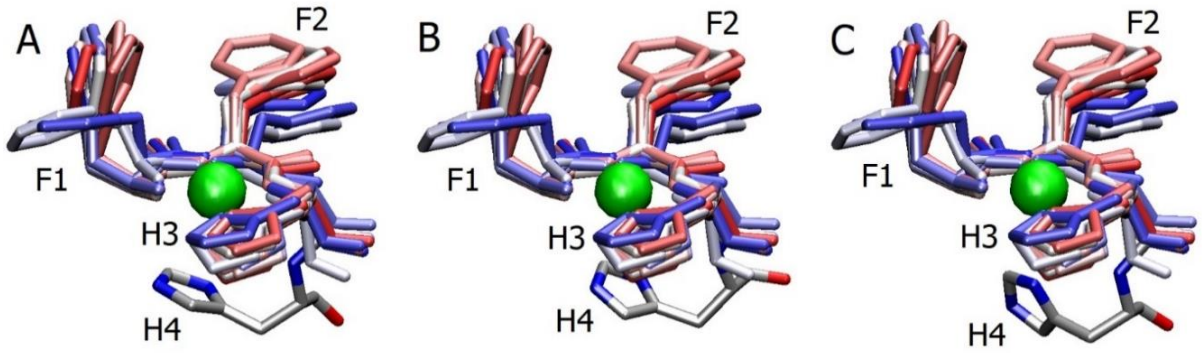

Figure 12. Overlays of the ATCUN residues and H4 for the P1:Ni^{2+} structures in POPC/POPG taken from the MD simulations at intervals of 200 ns (0:20:209). The structures from the beginning of the trajectory are colored red, the middle are white, and the end are blue. H4 residue is taken at (A) t = 1100 ns, (B) t = 1700 ns, (C) t = 2100 ns.

The dynamic nature of membrane-bound piscidin is reflected in the distribution of τ and ρ which do not change significantly in the presence of the Ni^{2+} ion (Figure 11). The overall loss of charge and the shielding of the metal by coordination and by hydrophobic sidechains make it less attracted to the negatively charged phosphate groups. As a result, the N-terminal end no longer points towards the phosphate groups and is now parallel to the surface for P1:Ni^{2+} and slightly canted toward the bilayer center (τ = 86°) in P3-Ni^{2+} (Table 2). The orientation of the C-

terminal ends, which were parallel to the surface for the apo piscidins, are tilted toward the bilayer core in the metallated peptides. This trend could be attributed to the need to maintain the kinked structures ($\Delta\tau \sim 4\text{-}8°$) which is more pronounced in P1. The MD τ values follow a similar trend to the experimental results (*M.L. Cotten, personal communication*): Ni^{2+}-bound peptides are tilted more towards the bilayer center than the apo peptides. P1:Ni^{2+} and P3:Ni^{2+} adopt more distinct ρ angles than the apo peptides (Table 2). Values of ~260° and ~235° for the apo peptide ρ_N (N-terminal residues) and ρ_C (C-terminal residues), respectively, assure an even distribution of the hydrophobic residues at the hydrophobic core of the lipids and the hydrophilic residues at the water-bilayer interface (Figure A1).[196] ρ_N values for P1 and P3 decrease by 10° and 11°, respectively, upon metallation. These changes allow the F1 and F2/I2 ATCUN residues to be better positioned in the lipid hydrophobic core and for H3 to be better placed at the water-bilayer interface. In contrast, the reduction in the ρ_C values allows the C-terminus hydrophobic and hydrophilic residues of P1:Ni^{2+} to be more evenly distributed in the bilayer than ones of P3:Ni^{2+} (Figure A1). Thus, the metallation has a different effect on the C-terminal end orientation in the membrane of these two isoforms. The $\Delta\rho$ (ρ_N - ρ_C) is reduced by only ~3.5° upon metal-binding for the following trend in $\Delta\rho$: P1 > P1:Ni^{2+} ≈ P3 > P3:Ni^{2+}. Therefore, the helical rotations on each side of the kink at G13 (the end of the $G(X)_4G$ motif) is dependent on both the sequence and the metallation state. The distinct rotation of the two ends of piscidins is required to maximize their hydrophobic interactions with the bilayer.

Generally, the peptide backbones for metallated piscidins are found at similar positions in the membrane compared to the apo peptides: ~7-8 Å below P atoms and just under the C2 atoms of the lipids sn-2 acyl chain (Table 2). Charge neutralization and metal-binding in the formation of the ATCUN complex influence the insertion of N-termini in the bilayer to a greater extent

than the C-termini. The distribution of insertion depths for the N-termini (z_N) cover a relatively small range, and the values are downshifted when metallated, especially for P3-Ni^{2+} (Figure 11). In contrast, the C-termini depths (z_C) have wider distributions and are indistinguishable between the apo and holo state of each isoform. Metallation deepens the N-terminal end in the membrane by ~0.9 Å for P1:Ni^{2+} vs. apo P1 and ~1.7 Å for P3:Ni^{2+} vs. apo P3, with both metallated isoforms sharing a z_N of ~9.1 Å (Table 2). The enhanced insertion of P1:Ni^{2+} and P3:Ni^{2+} may contribute to their higher toxicity toward planktonic bacteria when compared to the apo peptides.[235] To compensate for the increase in the magnitude of z_N, the C-terminal ends of the metallated peptides remain somewhat closer to the headgroups than their apo counterparts resulting in a greater $|\Delta z|$ ($|z_N - z_C|$, 1-2 Å vs 0.1 Å).

The insertion of P1:Ni^{2+} causes a negligible P-P thinning, while P3:Ni^{2+} does not modify the bilayer thickness (Table 1). At the same time, the C2-C2 distance slightly increases upon the insertion of the metallated peptides. The decomposed electron density profiles with contributions from the peptide backbone are asymmetrical suggesting an uneven distribution of the peptides in each leaflet (Figure 9). The mean distance of piscidin from the bilayer center increases in the following order P1:Ni^{2+} < P3:Ni^{2+} < P1 < P3 with P1: Ni^{2+} displaying a density maximum at ~9.9 Å. As such, metallation promotes a deeper peptide insertion into the bilayer which causes the membrane to thicken by extending the acyl chains. Similar bilayer behavior is also observed upon cholesterol incorporation into the membrane.[236,237] Metallation yields a smaller increase in A_L which stipulates a less dynamic diffusion of metal-bound peptides into the bilayer. In terms of K_A, P1:Ni^{2+} displays the greatest decrease suggesting that metallated P1 increases the fluidity of the membrane the most. Surprisingly, P3:Ni^{2+} shows an insignificant change in K_A compared with the bilayer alone, but the apo systems do show a decrease. The insignificant change in K_A

suggests a lack of conformational changes in the headgroup region, which would restrict the fluidity and may be caused by metallation-promoted fast diffusion of P3:Ni^{2+} through the headgroups.

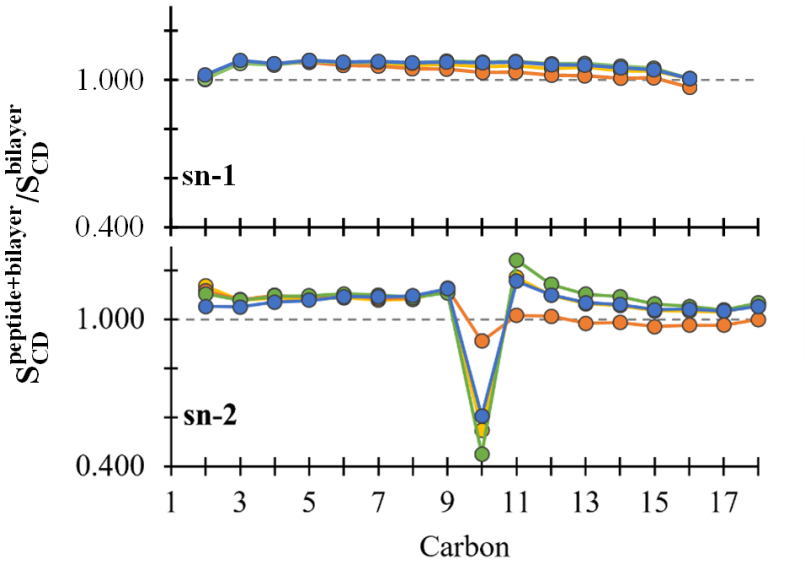

Figure 13. Average $S_{CD}^{peptide+bilayer}/S_{CD}^{bilayer}$ for the (top) sn-1 and (bottom) sn-2 lipid acyl chains in the presence of P1 (yellow), P3 (orange), P1-Ni^{2+} (green), and P3-Ni^{2+} (blue).

Deuterium order parameters (S_{CD}) of the carbons in the acyl chains (sn-1 and sn-2 positions of the glycerol core) indicate how straight (larger values) or kinked (smaller values) a lipid tail is, and usually are affected by peptide insertion. The ratio between S_{CD} of the systems with piscidin and that of bilayer alone is plotted separately for sn-1 (saturated) and sn-2 (unsaturated) chains in Figure 13. A value above 1 for the S_{CD} ratio indicates an increase in order

in the presence of the piscidin peptides. As previously reported,[214] sn-1 and sn-2 chains do not share the same ratio, an indication of different responses to the peptide. In the presence of peptides, the sn-1 chains exhibit a slight increase in the order of carbons near the headgroups and a continuous reduction with the lower carbons. There is no discrimination for a particular isoform (P1 or P3) or state (apo or Ni^{2+}-bound) in the S_{CD} values for these tails. The disorder of the sp^3 carbon in the saturated chain slightly increases in the presence of apo P3 but does not change with the other peptides. The sn-2 chain unexpectedly displays a greater packing order for all carbons except C10, the 2^{nd} sp^2 carbon, (indicative of kinked tails at this position) when piscidin, especially P1-Ni^{2+}, is present. P3 being the least inserted into the bilayer induces little change in S_{CD} of the carbons after the double bond (C9-C10, sn-2 chain) and only a modest decrease in the case of C10. These smaller values for C10 could account for the decreased K_A in the peptide-containing systems where P1-Ni^{+} induces the highest reduction.

MD simulations of piscidins in POPC/POPG/aldo-PC bilayers

MD simulations were performed on POPC/POPG/aldo-PC bilayer alone for comparison with the POPC/POPG bilayer. Both peptide-free membranes are in the fluid phase and well equilibrated since the calculated A_L for the POPC/POPG and POPC/POPG/aldo-PC bilayer alone agree well with the experimental A_L values for the pure POPC bilayer (Tables 1 and 3). While almost identical A_L values were obtained for the two membranes, smaller V_L (1183 vs 1206 $Å^3$) and thicknesses (thinning by ~1 Å for both h(P-P) and h(C2-C2)) were calculated for the aldo-PC-containing bilayer consistent with the shortened acyl chain of aldo-PC. The lower K_A for the POPC/POPG/ aldo-PC *versus* POPC/POPG bilayer (243 ± 88 vs 254 ± 114) suggests that the presence of 10% aldo-PC increases the fluidity of the membrane and reduces the interactions between the headgroup constituents (Figure 14). This observation is further supported by the S_{CD}

parameters which indicate that the disorder of the lipid acyl chains in the presence of aldo-PC steadily increases starting with the first sp^2 carbon (Figure 15C). Interestingly, C10 of the sn-2 chain is the only carbon where the lipid tails experience a straighter, more ordered position in the aldo-PC-containing bilayer, in contrast to the piscidin-bound POPC/POPG membranes (Figure 9). The carbonyl functionalized chains often reorient to reach the headgroup region contributing to the destabilization of the bilayer (Figure 15B). Similar interfacial conformations were previously reported from the simulation of 25% aldo-PC in POPC.[213] Thus, a more fluid (liquid-like) membrane (lower K_A and S_{CD}), which contains more kinked lipid tails (smaller S_{CD}) in the presence of aldo-PC is consistent with the ability of oxPLs to disrupt membrane bulk proprieties and exhibit enhanced permeabilization.[207,211,212]

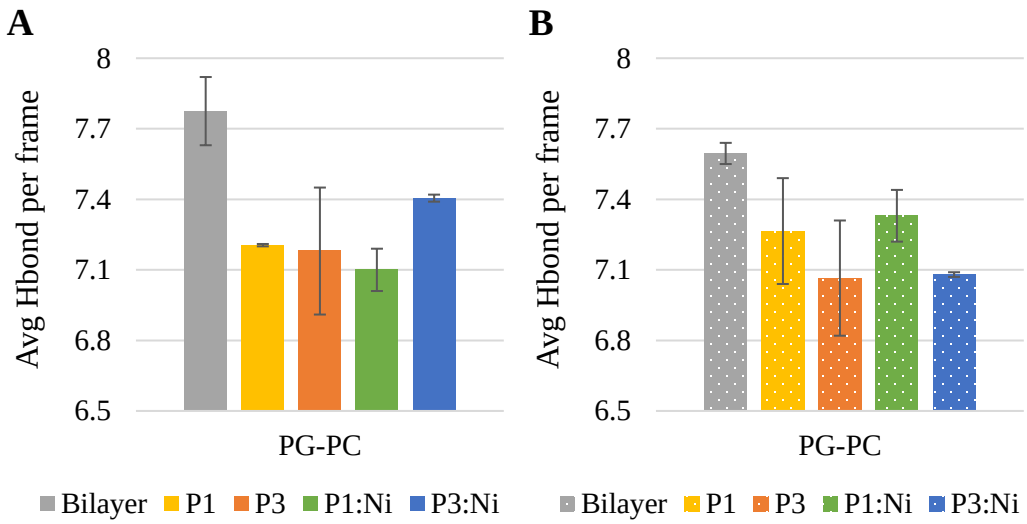

Figure 14. Average hydrogen bonds per frame between PC and PG headgroups in (A) POPC/POPG and (B) POPC/POPG/aldo-PC bilayer.

Table 3. Average structural properties over two trials of the POPC/POPG/aldo-PC bilayer system simulations, where V_L is volume per lipid, A_L - area per lipid, K_A - isothermal area expansion modulus, h(P-P) – headgroup-to-headgroup thickness and h(C2-C2) – hydrophobic thickness

POPC/POPG/ aldo-PC	V_L (Å^3)	A_L (Å^2)	K_A (mNm^{-1})	h(P–P) (Å)	h(C2–C2) (Å)
Exp	*1256**[227] *1265*[§228]	*64.3*,65.3*[§228] *68.3**[227]	*180-330**[229]	*37.0**[227] *36.0*[§228]	
MD	1183 ± 0	67.7 ± 0.6	243 ± 88	36.4 ± 0.2	26.3 ± 0.3
+ P1	1267 ± 0	72.5 ± 0.5	185 ± 81	36.3 ± 0.3	26.3 ± 0.5
+ P3	1264 ± 0	72.1 ± 0.5	198 ± 95	36.3 ± 0.4	26.4 ± 0.5
+ P1-Ni^{2+}	1267 ± 0	72.2 ± 0.4	222 ± 93	36.5 ± 0.3	26.6 ± 0.3
+ P3-Ni^{2+}	1264 ± 0	71.9 ± 0.5	212 ± 86	36.5 ± 0.3	26.5 ± 0.4

The experimental value for pure POPC at (*) 303K and (§) 313K

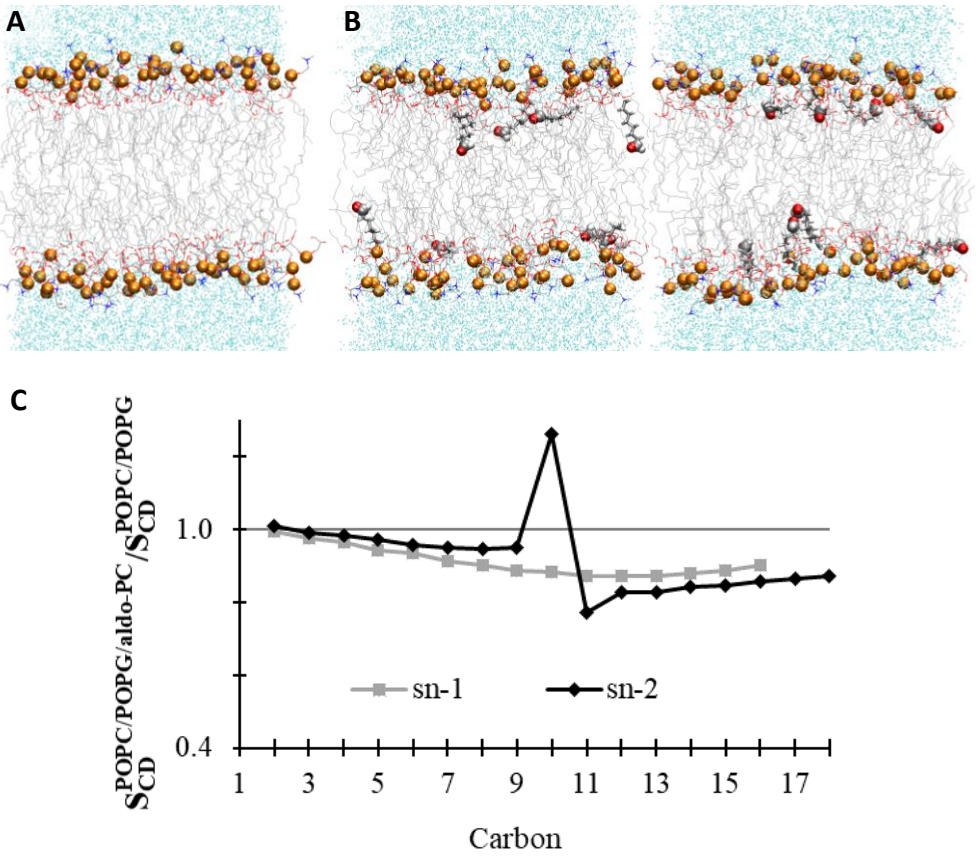

Figure 15. Comparison between POPC/POPG and POPC/POPG/aldo-PC bilayer alone. Snapshots from MD simulations of (A) POPC/POPG and (B) POPC/POPG/aldo-PC. Aldo sn-2 acyl chains are represented as licorice and the carbonyl group as spheres. Phosphorous atoms are depicted as orange spheres while the rest of the phospholipid atoms except hydrogens are depicted as lines colored as follows: carbon – gray, oxygen – red, and nitrogen – blue. Water molecules are represented as cyan points. (C) Average $S_{CD}^{POPC/POPG/aldo-PC}/S_{CD}^{POPC/POPG}$ for the sn-1 and sn-2 lipid acyl chains.

All-atom MD simulations for apo and metallated P1 and P3 in 2.6:1:0.4 POPC/POPG/aldo-PC bilayer were performed to study the membrane-bound piscidins in the

presence of oxPLs. As previously observed, A_L increases upon the addition of piscidin peptides to the bilayer with a slightly more pronounced expansion for the P1 isoform (Table 3). A greater change in A_L is associated with a more dynamic diffusion of the peptide molecules into the bilayer. Since the A_L increase is lower in the presence of metal-bound peptides, one may assume that the net loss of one positive charge upon metallation leads to reduced electrostatic interactions with the headgroup regions, hence a less dynamic diffusion. The calculated V_L share a similar trend with the A_L, but contrary to the latter, are slightly smaller when compared with the POPC/POPG bilayers due to the shortened functionalized sn-2 chain (Table 1 and 3). Upon insertion, the peptides induce a disruption within the phospholipid chain packing that promotes membrane fluidity as shown by the ~9-24% drop in K_A (Table 3). The apo peptides have lower K_A than the metallated piscidins with P1:Ni^{2+} displaying the lowest decrease in K_A among the tested peptides, in contrast to its performance in the POPC/POPG bilayer. As in the case of P3:Ni^{2+} in POPC/POPG, the smaller K_A change induced by Ni^{2+}-bound piscidins may be the result of faster peptide diffusion into the membrane in agreement with the calculated A_L values. This fast diffusion in conditions of aldo-PC and Ni^{2+} ions should yield minimum disruption of the interactions (e.g., hydrogen bonding) between the lipid headgroup constituents. Figure 14 shows that while the average number of hydrogen bonds generally lowers in the presence of piscidin, P1:Ni^{2+} (and P3:Ni^{2+} in POPC/POPG) induced only a slight decrease in hydrogen bonding.

The ratio of S_{CD} for the piscidin-containing systems and bilayer alone is plotted separately for sn-1, sn-2, and sn-2 (aldo-PC) in Figure 16. The trends in the S_{CD} ratios of the sn-1 and sn-2 chains, which generally react differently to the peptide insertion, are not significantly influenced by the presence of aldo-PC. The sn-2 chains (except for the C10 carbon) also have a

greater packing order than the sn-1 ones in the presence of piscidins. Here, apo P3 is positioned farthest from the bilayer center and induces the least amount of change to the order of the sp^2 carbon and the subsequent carbons; but it is not as distinguishable from the other peptides as in the POPC/POPG membrane. Generally, sn-2 carbons following C10 are less kinked (higher S_{CD}) in the presence of Ni^{2+}-bound piscidins which agrees with the smaller K_A change in these systems. The aldo-functionalized sn-2 tails have a unique behavior in the presence of the peptides. They occasionally reorient to expose the carbonyl groups to the water phase in addition to positioning at the phosphate interface (Figure 17B and C). Such a reversal is expected to influence membrane structure more strongly. The large increase in packing order for the first three (C2-C3-C4) carbons, hence straighter lipid chains, is interrupted at C5 when a sharp drop places the rest of the carbons in a disordered state (more kinked tails).

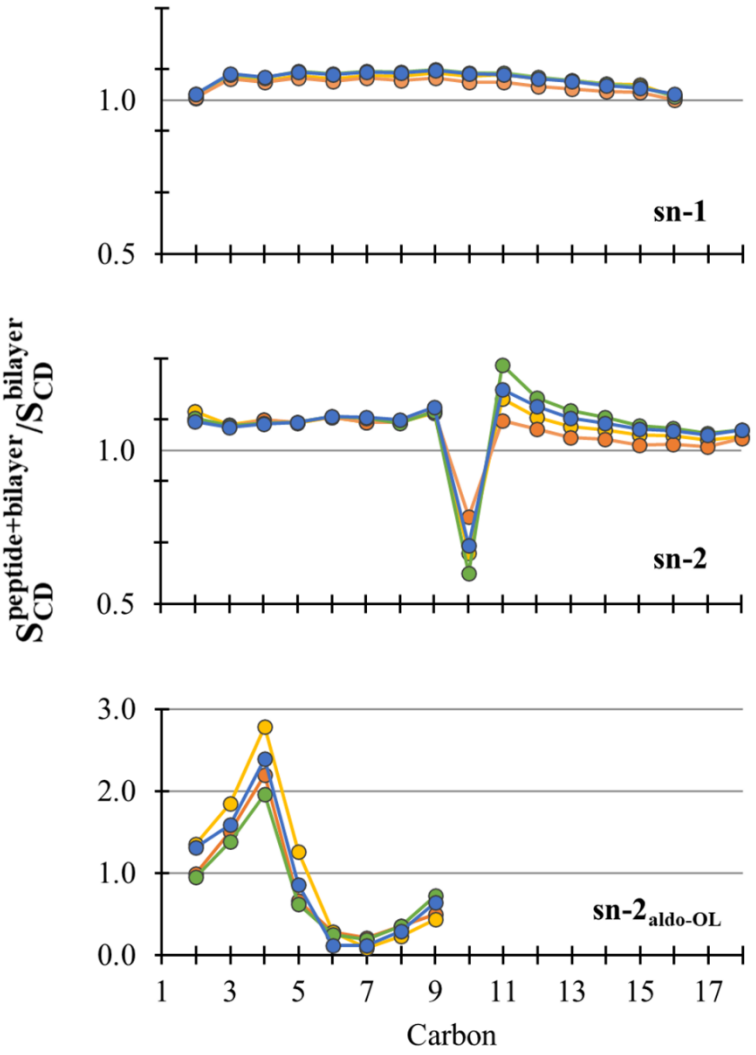

Figure 16. Average $S_{CD}^{peptide+bilayer}/S_{CD}^{bilayer}$ for the (top) sn-1, (middle) sn-2, and (bottom) sn-$2_{aldo\text{-}OL}$ lipid acyl chains in the presence of P1 (yellow), P3 (orange), P1-Ni^{2+} (green) and P3-Ni^{2+} (blue).

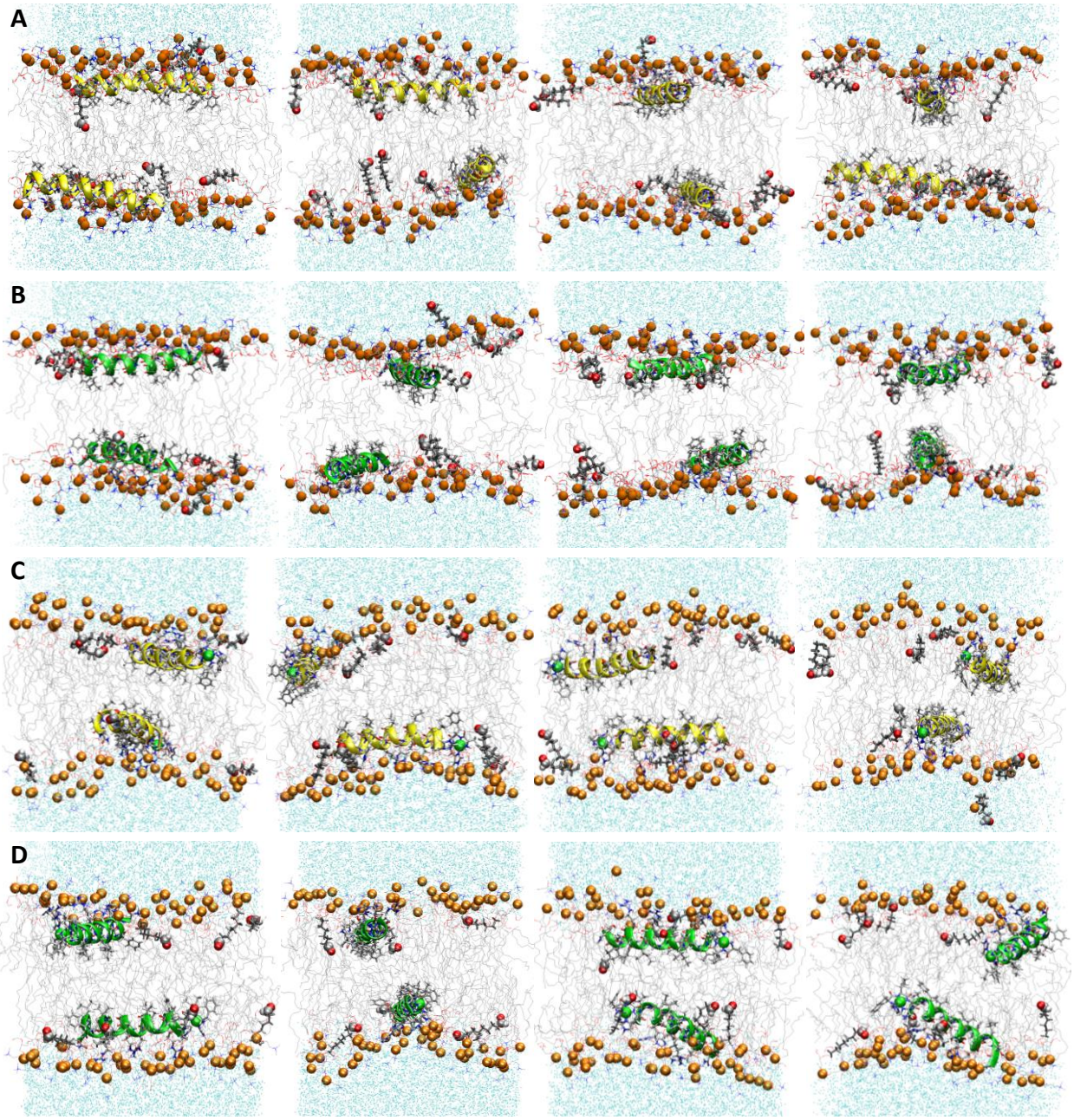

Figure 17. Snapshots from MD simulations of (A) P1, (B) P3, (C) P1:Ni^{2+} and (D) P3:Ni^{2+} in POPC/POPG/aldo-PC. Peptides are represented as yellow (P1 isoforms) or green (P3 isoforms) ribbons and licorice. Ni^{2+} ions and phosphorous atoms are depicted as green and orange spheres, respectively, while the rest of the phospholipid atoms except for hydrogen are depicted as lines colored as follows: carbon – gray, oxygen – red, and nitrogen – blue. Aldo sn-2 acyl chains are represented as licorice, and water molecules as cyan points.

The incorporation of oxPLs into the bilayers does not significantly affect the electron density profiles as they share features with POPC/POPG systems (Figures 9 and 18). Similar changes are observed upon piscidin insertion either in the presence or absence of aldo-PC except for a larger decrease in the PO_4 density peak in the POPC/POPG/aldo-PC bilayers. The headgroup-to-headgroup bilayer thickness (h(P-P)), calculated from the phosphate electron density profiles, is ~10 Å greater than the hydrophobic one (h(C2-C2)) (Table 3). The same difference was observed for POPC/POPG membranes in this study and previously reported by Perrin et al[214]. Apo piscidins slightly reduce the P-P thickness whereas the Ni^{2+}-bound ones have an opposite effect (Table 3). At the same time, the C2-C2 thickness of the POPC/POPG/aldo-PC bilayer widens in the presence of all peptides except apo P1. Generally, an increase in the bilayer (hydrophobic) thickness may be caused by the extension of acyl chains followed by an increase in S_{CD}. The maximum density of P1:Ni^{2+} peptide is on average ~9.3 Å (vs. ~9.9 Å in POPC/POPG) which places it closest to the bilayer center, followed by P3:Ni^{2+} then P1 and P3. As noted for the POPC/POPG systems, peptide position in the membrane deepens with metallation which promotes acyl chain extensions and membrane thickening.

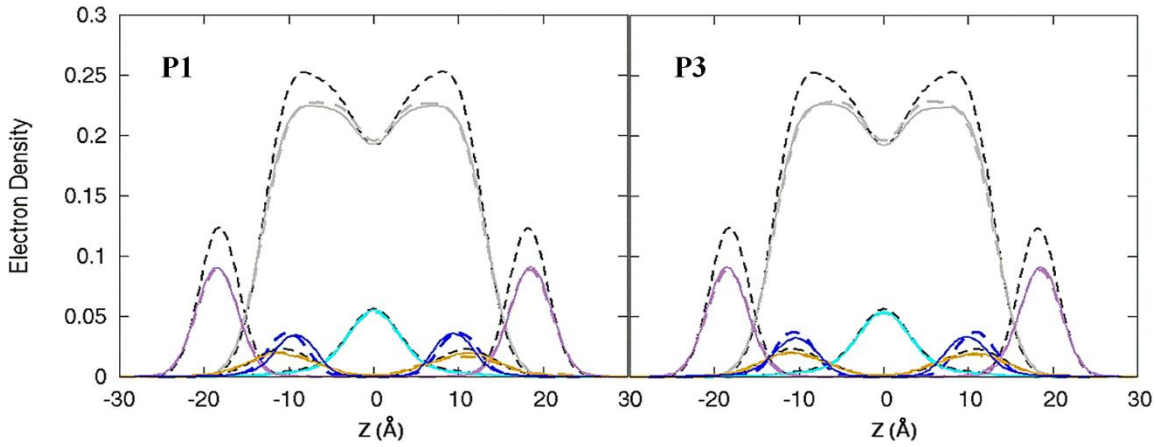

Figure 18. Electron density profiles for P1 and P3 in POPC/POPG/aldo-PC. Profiles are shown for the phosphates (purple), peptides (blue), CH_2 acyl chains (gray), and terminal CH_3 (cyan). Electron density profiles containing membrane and apo or metallated piscidin are in dashed or solid lines, respectively, whereas the systems with only the membrane are in dashed black lines.

The piscidin peptides do not change their flexibility in the presence of aldo-PC as indicated by the analogous backbone heavy-atom root-mean square deviations (RMSDs) for the first 20 residues (RMSD = 0.75/0.78 Å and 0.83/0.89 Å for P1/P1:Ni^{2+} and P3/P3:Ni^{2+}, respectively). The ATCUN residues also maintain low RMSD values in POPC/POPG/aldo-PC (0.20 Å and 0.22 Å for P1:$Ni^{2+}$and P3:Ni^{2+}, respectively). Like in the case of the POPC/POPG systems, both metallated and apo α-helical peptides diffused below the phosphorus plane of the aldo-PC-containing bilayer orienting the hydrophilic residues toward the water-bilayer interface (Figures 10 and 17). The cationic sidechains are well-extended and interact preferentially with the anionic PG headgroups towards the end of the simulation. As in the POPC/POPG bilayer, the apo piscidins orient the N-terminal end on average toward the headgroups (τ = 95°/93) with azimuthal rotation angle (ρ) values of 259° and 249° for P1 and P3, respectively (Table 4).

Table 4. Tilt angles τ (°), azimuthal rotation angles ρ (°) and depths of insertion z (Å) for the backbone atoms of N- (residues 5−10) and C- (residues 14−20) helical segments of each peptide in POPC/POPG/aldo-PC averaged over two trials. Insertion depth for the backbone atoms of the full-length peptide ($z_{1\text{-}22}$) is also reported

	τ_N	τ_C	$\Delta\tau = (\tau_N - \tau_C)$	
P1	95 ± 1	88 ± 1	7.6 ± 1	
P3	93 ± 0	89 ± 1	4.5 ± 1	
P1-Ni^{2+}	90 ± 1	83 ± 1	6.6 ± 1	
P3-Ni^{2+}	85 ± 1	83 ± 1	2.1 ± 1	
	ρ_N	ρ_C	$\Delta\rho = (\rho_N - \rho_C)$	
P1	259 ± 2	240 ± 2	19.0 ± 1	
P3	249 ± 3	228 ± 4	21.0 ± 2	
P1-Ni^{2+}	251 ± 1	234 ± 2	16.3 ± 1	
P3-Ni^{2+}	232 ± 4	216 ± 2	16.0 ± 6	
	z_N	z_C	$\Delta z = (z_N - z_C)$	$z_{1\text{-}22}$
P1	-8.1 ± 0.2	-8.2 ± 0.4	0.2 ± 0.2	-7.7 ± 0.2
P3	-7.6 ± 0.1	-7.6 ± 0.1	0.0 ± 0.0	-7.2 ± 0.1
P1-Ni^{2+}	-9.2 ± 0.3	-8.0 ± 0.3	-1.2 ± 0.1	-8.4 ± 0.3
P3-Ni^{2+}	-8.7 ± 0.2	-6.9 ± 0.2	-1.8 ± 0.2	-7.6 ± 0.1

Metallation decreases the charge of the ATCUN motif by one but does not alter the dynamics of the membrane-bound piscidins (Figure 19). In the presence of aldo-PC, the orientation of the N-terminal end remains parallel to the surface for P1:Ni^{2+} and slightly toward

the bilayer core (τ_N = 85°) for P3:Ni^{2+} (Table 4). The kinked peptides at Gly13 tilt the C-terminal ends toward the bilayer center for the Ni^{2+}-bound piscidins or position it parallel to the surface for the apo piscidins, as observed in the absence of aldo-PC or when bound to membranes of different composition (P1/P3 in DMPC/DMPG and POPE/POPG bilayers)[196]. In terms of the azimuthal rotation angles, the P1 values are affected only by metal binding as P1:Ni^{2+} experience similar ρ in both lipid mixtures, while the P3 ρ values respond to the addition of metal ion and lipid oxidation since ρ_N and ρ_C of P3:Ni^{2+} decrease by 5° and 8°, respectively, and sample a broader range in POPC/POPG/aldo-PC (Tables 2 and 4, and Figure 19). This ρ_C reduction aggravates the uneven distribution of the C-terminal hydrophobic and hydrophilic residues in the bilayer. P3 is the only isoform that slightly changes its Δρ values in the presence of aldo-PC (5.7° and 3.3° increases for the apo and Ni^{2+}-bound piscidin, respectively) and the following Δρ trend is recorded for the studied peptides: P3 > P1 > P1-Ni^{2+} ≈ P3-Ni^{2+}. Increased structural changes of piscidins (i.e., P3) may be due to more interactions with the aldo-PC-containing bilayer which could suggest that P3 is more efficient than P1 at permeabilizing bacterial membranes in the presence of aldo-PC.

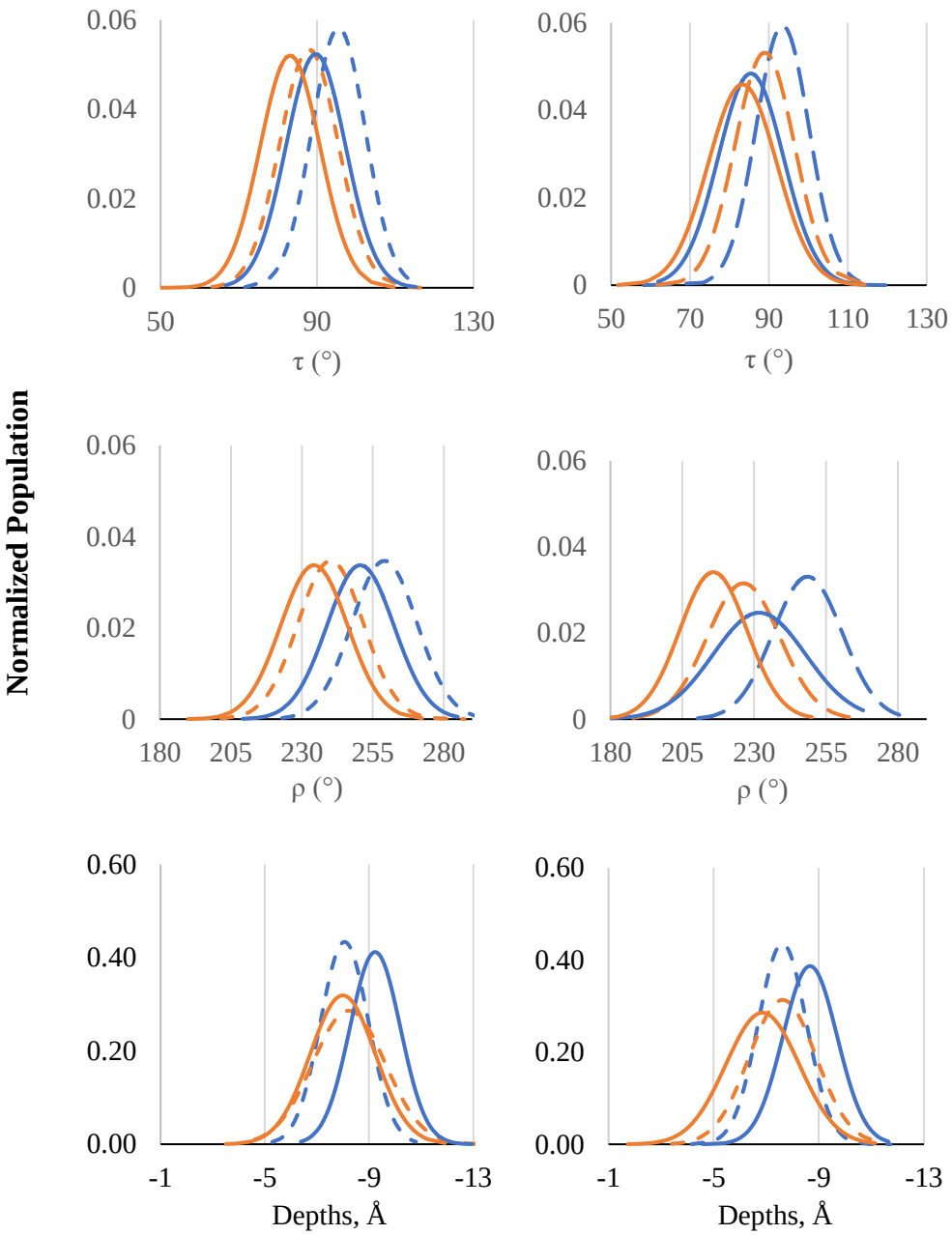

Figure 19. Distribution of tilt angles, azimuthal rotation angles, and depths of insertion sampled by the N- (blue) or C- (orange) terminal residues of P1 (left) or P3 (right) in POPC/POPG/aldo-PC during the 2-μs MD simulations. Curves for apo and metallated piscidins are shown as dashed and solid lines, respectively.

The average insertion depths (z) of piscidin relative to the P atoms of all the headgroups from the same leaflet as the peptide are listed in Table 4 and their distribution is plotted in Figure 19. The peptide backbones are located at similar depths in the POPC/POPG/aldo-PC bilayer as to those in the aldo-PC-free membrane (~7-8 Å below P atoms and just under the C2 atom of the lipids sn-2 acyl chains). As a result, the depth of insertion of the N- (z_N) and C-terminal (z_C) end for both apo and Ni^{2+}-bound piscidins have similar values and distributions in the presence of aldo-PC as in its absence. The two peptide isoforms share alike distribution plots for the insertion depths where the N-termini sample a relatively narrow z_N range compared with the C-termini and downshift upon metallation. P1 inserts its terminal ends into the aldo-PC-containing membrane deeper (by ~0.5 Å) than P3, consistent with their activity in POPC/POPG bilayer reported in this study and previously by Perrin et al[214] (Table 4). Metallation advances the diffusion of the N-terminal ends by ~1.1 Å deeper into the membrane such that the z_N of P1:Ni^{2+} becomes distinguishable from P3:Ni^{2+} in the presence of oxPLs (z_N ~9.2 Å vs. 8.7 Å). Meanwhile, the peptides C-terminal end, particularly of P3:Ni^{2+}, inserts less than their apo counterparts and continue to yield larger $|\Delta z|$. Thus, the formation of the ATCUN complex influences the orientation of the N-terminal end in the bilayer to a greater extent than the C-terminal end, since the latter one is not chemically modified.

^{31}P NMR studies have shown that the PG headgroup region responds more strongly to P1:Ni^{2+}, but not P3:Ni^{2+}, in the presence of aldo-PC and at 1:20 peptide-to-lipid ratio.[205] The interactions between piscidin and headgroups (PC-peptide and PG-peptide) were assessed through hydrogen bond analysis. The absolute values for these interactions do not necessarily reflect the peptide preference for a specific headgroup region since neither the number of each headgroup (60 PC vs 20 PG) in the bilayer nor the number of donor/acceptor sites per molecule

(9 vs 12 in PC and PG, respectively) is equal. Nonetheless, this analysis can offer insights into how aldo-PC changes the interactions patterns of piscidin with the lipid headgroups. As seen in Figure 20, the average number of PG-peptide hydrogen bonding interactions slightly increases for P1:Ni^{2+}, but not for P3:Ni^{2+} in the presence of aldo-PC, in perfect agreement with the experimental data[205]. In the case of apo piscidin, P1 increases its hydrogen bonding with the PC headgroups, and reduces those with PG, whereas P3 follows an opposite trend. Altogether, these results suggest that in the presence of oxPLs, P1:Ni^{2+} may interact more readily with the anionic PG headgroups, which correlates well with the enhanced membrane activity of the peptide on the POPC/POPG/aldo-PC lipid mixture.[205]

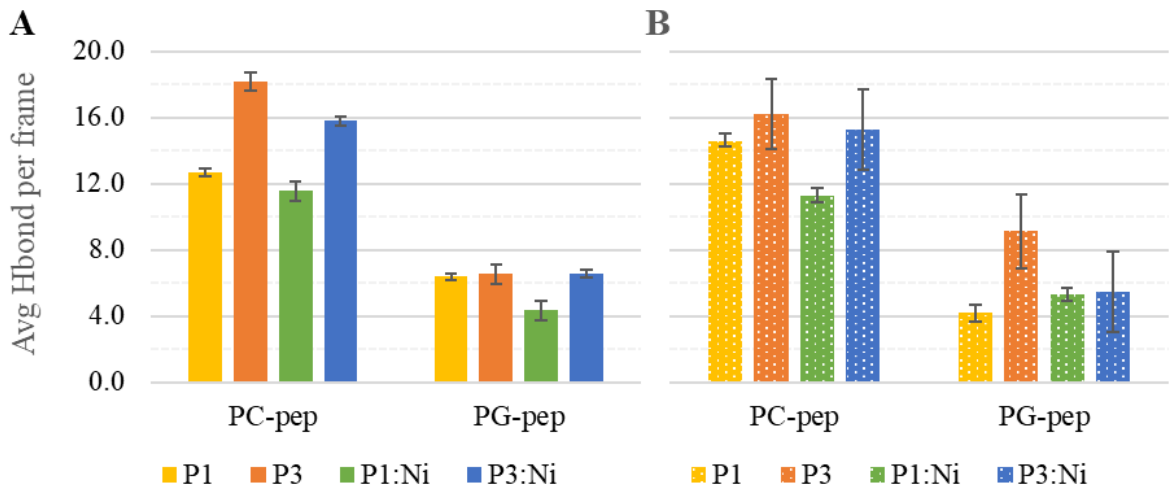

Figure 20. Average hydrogen bonds per frame between piscidin and lipid headgroup constituents in (A) POPC/POPG and (B) POPC/POPG/aldo-PC bilayer.

Conclusions

Piscidins are a promising template for novel antimicrobial and antiviral therapeutics. Their activity is enhanced *in vitro* by the formation of the ATCUN-Ni^{2+} complex and the presence of oxidized lipid species. All-atom MD simulations examined the effect of piscidin metallation and oxidized lipid incorporation on the structural properties of the bacterial membrane and its interactions with the peptides. Apo and metallated P1 and P3 bound to binary (POPC/POPG) or tertiary (POPC/POPG/aldo-PC) lipid mixtures were used as models for this investigation. Piscidins are shown to be flexible in the membrane and insert at distinct depths that depend on the particular isoform (P1 vs P3) and state (free or Ni^{2+}-bound). The magnitude of the insertion depths has been proposed to be indicative of the membrane activity of piscidins. Apo P1 tends to insert deeper than P3 with no preference for a particular terminal end, while both Ni^{2+}-bound piscidins become more tilted and insert their N-terminal ends deeper in the bilayer. Thus, metallation is expected to enhance the membrane activity of these peptides.

Piscidin insertion induces structural changes to the bilayer that could precede complete membrane disruption and bacteria death. Upon peptide insertion, the bilayer becomes more fluid (“liquid-like”) and expands in all directions. Metallated piscidins induce a smaller expansion possible due to faster diffusion into the bilayer as a result of the net loss of a positive charge. The less cationic metal-bound peptides could more readily overcome the electrostatic interactions with the anionic PG headgroups to successfully insert into the bilayer. In the presence of aldo-PC whose functionalized chains reorients towards the aqueous phase, the number of hydrogen bonds between the headgroup constituents is reduced. Such observations support the idea of oxPLs incorporation disrupting the bulk properties of the membrane. The peptides do not significantly

modify their orientations and insertion depths in the presence of oxPLs; but computational evidence for P1:Ni^{2+} prompter association with the bacterial anionic headgroups is shown, which is in agreement with NMR data. Altogether, these results suggest a potential mechanism for the enhanced activity of metallated peptides in the presence of oxPLs considering that a deeper insertion and a preferential association with anionic headgroups may promote the disruption of the bacterial membrane.

CHAPTER III

MOLECULAR DYNAMICS SIMULATIONS OF REDUCED AND OXIDIZED TFIIIA ZINC FINGERS FREE AND INTERACTING WITH 5S RNA[a]

Introduction

Zinc fingers (ZF), one of the largest classes of proteins, are an important subset of zinc-binding proteins that carry out a broad range of cellular functions including transcription, signal transduction, DNA repair, cell proliferation, differentiation, apoptosis, and tumorigenesis.[238–241,94,242–244] ZFs are grouped into three classes based on the combination of Cys and His residues in the tetrahedral coordination sphere of Zn^{2+}: Cys_4, $Cys_2HisCys$, or Cys_2His_2.[93,94] The Zn^{2+} ion is required for proper folding of these domains. The Zn^{2+}-bound Cys_2His_2-type folds into a ββα structure and was initially discovered as a sequence-specific DNA binding motif in transcription factor IIIA (TFIIIA) of *Xenopus laevis*.[245] Cys_2His_2-type ZFs mediate various protein-protein and/or protein-nucleic acids interactions.[246] Examples include the IKAROS family,[247] Kruppel like factors (KLF),[248] specificity proteins (SP)[249] and Zif268/Egr-1.[250] TFIIIA recognizes and binds nucleic acids through nine ZF domains.[251] In addition to two clusters of three-ZFs that bind the 5S DNA, the three or four middle ZFs are selective for 5S RNA binding.

Reactive oxygen species, reducible sulfur/selenium compounds, and other cellular oxidants inhibit ZnS proteins through oxidization of the Cys thiolates.[252–257,96,101,258,100,95,259] The

---

[a] Reprinted with permission from Dreab, A; Bayse, C. A. Molecular Dynamics Simulations of Reduced and Oxidized TFIIIA Zinc Fingers Free and Interacting with 5S RNA. *J. Chem. Inf. Model.* **2022**, *62*, 903-913. Copyright 2022 American Chemical Society. The manuscript can be found online at https://doi.org/10.1021/acs.jcim.1c01272.

disulfide bond, the major oxidation product at pH 7.0, cannot effectively coordinate Zn^{2+} which leads to the unraveling of the tertiary structure required for nucleic acid recognition and binding.[241,257,95,259,260] As a result, Zn^{2+} release is associated with disruption of gene expression and DNA repair, which can prevent tumor growth.[259,261] Inhibition of ZF proteins involved in the survival and proliferation of cancer cells, such as histone lysine methyltransferases G9a and GLP,[115,262] breast cancer-associated protein 2 (BCA2),[263] or transcriptional coactivators p300/CBP[116,117] is a promising strategy for cancer treatment. The transcription factor ZNF143 with seven Cys_2His_2-type ZFs is overexpressed in many tumors and promotes cisplatin resistance.[264–266] Targeted oxidation of ZNF143 could inhibit DNA binding and serve as a potential therapeutic. ZFs oxidation is also a potential mechanism for treating viral infections. For example, disulfiram and ebselen were shown to eject Zn^{2+} from the multiprotein SARS-CoV2 replication and transcription complex and inhibit replication when combined with remdesivir.[98,99]

TFIIIA binds to 5S DNA and 5S RNA via distinct molecular mechanisms.[267] 5S DNA binding by TFIIIA has been modeled computationally, but only one short simulation of ZF456 of TFIIIA - 5S RNA has been reported in the literature.[268–272] TFIIIA promotes the expression of the 5S RNA gene during oogenesis acting as a positive transcription factor.[273–276] TFIIIA also serves as a storage particle when bound to 5S RNA in the cytoplasm forming the 7S ribonucleoprotein (7S RNP).[277,278] Studies suggest that 7S RNP formation depends on the structure and conformation of 5S RNA and many weak protein–RNA sequence-specific interactions.[279–281] TFIIIIA binding to RNA is entropically and enthalpically favored ($K_d \approx 1$ nm) through the formation of approximately five salt bridges between lysine residues and the RNA nucleotide phosphate backbone.[282] Key TFIIIA residues for 5S RNA recognition and the

minimum RNA regions that sustain the binding have been identified by protein mutagenesis and RNA deletion analysis.[278,283–286]

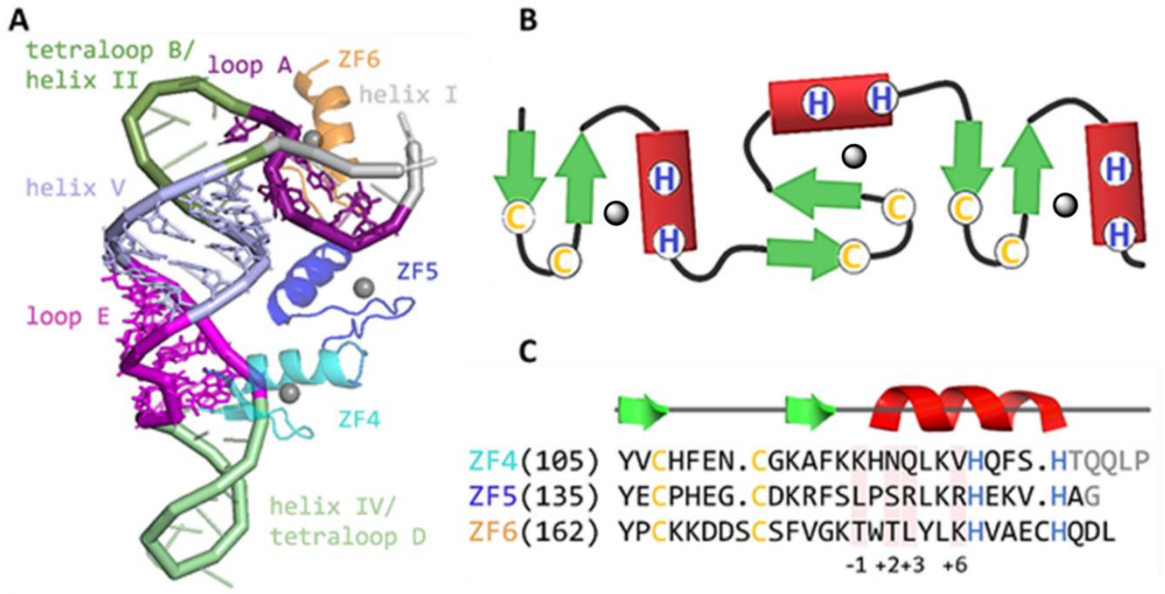

Figure 21. NMR structure and sequence of the ZF456-55mer 5S RNA complex. (A) NMR structure of the ZF456-5S RNA complex (PDB: 2HGH, conformer 2)[287]. The three zinc fingers are depicted as cartoons and colored in cyan (ZF4), blue (ZF5), and orange (ZF6). The gray spheres represent the Zn^{2+} ions. (B) Cartoon representation of ZF456 peptide. (C) Sequence and corresponding secondary structure of ZF456 with the conserved Zn^{2+} binding Cys and His residues shown in yellow and blue, respectively.

ZF456 represents the minimal polypeptide required for high-affinity binding to 5S RNA.[283,288] These ZFs bind similarly to the central core region of 5S RNA (loop B/helix II/loop A/helix V/region E, Figure 21A) either in the full-length TFIIIA molecule or truncated

peptide.[278,283,288] Interactions between ZF456 and loop A, in particular, are required for proper RNA recognition by ZF5 and ZF6.[289] In ZF4-7, simultaneous alanine substitutions of α-helix residues at positions -1, +2, +3, and +6 in ZF4 and ZF6 (the N-terminal residue in the α-helix is at position +1, Figure 21C) reduced the affinity for 5S RNA by 77-fold and 43-fold, respectively.[286] Single mutations at position -1 (e.g., K118A in ZF4-7 and T176I in Zn1-7) lead to more than 36.5-fold reductions in RNA binding.[283,286] Alanine replacement of Trp177 (W177A) resulted in decreased 5S RNA binding in the full-length protein and complete loss of binding in the ZF456 peptide.[278] However, the W177F mutant retained the affinity for 5S RNA in both ZF456 and full-length TFIIIA[278] suggesting that Trp177 is important for RNA recognition through π-stacking with A6.[253,278,290] Substitution of the Thr176-Trp177-Thr178 (TWT) motif with RSD from Wilms tumor suppressor protein WT1 reduced the affinity for 5S RNA by ~11-fold.[285]

NMR and molecular dynamics (MD) studies of ZF456 - 5S RNA complexes have provided additional context for the biochemical, mutagenesis, and crystallographic studies.[268,278,283–285,287–290] For example, hydrogen bonding between the 2′-hydroxyl of G26 hydrogen and Tyr105 could be obstructed by an Mg^{2+} in the crystal structure as an artifact of the buffer solution.[287,290] Additionally, ZF5 appears to be a nonspecific spacer element dependent upon the base-specific contacts made by its neighboring ZFs with RNA despite the enhancement of RNA binding by the interactions of its basic residues with the phosphate backbone.[287,290] Nanosecond scale molecular dynamics (MD) simulations of a ZF456 – 61mer 5S RNA, starting from its crystal structure (PDB: 1UN6)[28] showed that interdomain motions observed upon RNA binding involved burial or exposure of key residues for DNA or RNA binding, respectively (Leu148 and Trp177, respectively).[268]

These experimental and computational studies have provided a picture for interactions of reduced ZFs with RNA, but neither the effect of Cys oxidation on ZF proteins nor the interaction of oxidized ZFs with nucleic acids has been examined at the atomistic level. Here, multi-microsecond MD simulations were performed on ZF456 bound to its cognate 5S RNA and free ZF456 in both reduced and oxidized forms to determine how oxidation of the ZFs affects the conformation of the free and RNA-bound protein. Since structural transitions in biomolecules can require an extended time scale,[291] MD simulations were performed for up to 30 μs; conformation changes that occur on longer timescales may not be observed. Disulfide bond formation is shown to induce significant conformation changes in the free protein that would inhibit RNA binding. In the oxidized ZF456-RNA complex, major hydrogen bonds important to recognition are lost which may lead to dissociation of the oxidized ZFs over longer timescales.

Computational Methods

The initial protein and protein-RNA models were obtained from the solution NMR structure of TFIIIA ZF456 bound to 5S rRNA 55-mer (PDB: 2HGH; residues 104-190, conformer 2).[287] The H++ server[292] was used to inform the assignment of His protonation states in the presence and absence of RNA (protonated His108 and His119 when bound to RNA, unprotonated otherwise, and protonated His139 in both cases). Since NMR data suggests that His119 is protonated upon RNA binding,[287] two sets of protonation states were considered for His outside the Zn^{2+} coordinate sphere (Table 5) to account for the H++ pKa-based prediction and experimental observations. For oxidized ZF models, Zn^{2+} was removed; the hydrogen on the δ-nitrogen of Zn-binding His residues (HID) was relocated to the ε-nitrogen (HIE); and a

disulfide bond was created between the Zn-binding Cys residues (CYX). MD simulations were performed using the PMEMD GPU implementation in AMBER 16/18.[218] The protein and RNA were represented with the *ff14sb* and OL3 force field, respectively.[136,137] Zinc and its coordinated Cys and His residues were modeled with the Zinc AMBER force field (ZAFF).[147] All systems were solvated with a 20 Å rectangular box of TIP3P water. SHAKE constraints were applied to bond lengths to hydrogen atoms. Models were initially heated and equilibrated with constant volume and temperature from 0 to 300 K using Langevin dynamics. The models were then equilibrated in the NPT ensemble, followed by multi-microsecond production simulations.

Table 5. Protonation states of His residues outside the Zn^{2+} coordination sphere (neutral (n) or protonated (p)) and timescales of MD simulations

	H108	**H119**	**H139**	**MD time (μs)**
reduced ZF456 (redZF456) - 5S RNA	p	p	p	12
redZF456	p	p	p	30
	n	n	p	30
oxidized ZF456 (oxZF456)	p	p	p	30
	n	n	p	30
oxZF456 - 5S RNA	p	p	p	30
	n	n	p	30

Hydrogen bond analysis using geometric criteria (acceptor-donor distance ≤ 3.3 Å and angle ≥ 135°) was performed on the complex for comparison to available experimental data.

(Table A1). The Define Secondary Structure of Proteins (DSSP) algorithm[293] was used to estimate the secondary structure propensities of the oxidized ZF456 peptides throughout the simulation. Additional trajectory analysis of MD trajectories was conducted using the TimeScapes package of Python routines.[158,294,295] This method identifies residues that move more quickly than the global dynamics of the biomolecular system by determining pairwise contact events and hinge motions in the backbone. In this approach, the trajectory is analyzed in terms of coarse-grained sidechains rather than Cα motion as in the traditional root-mean square deviations (RMSD). The rates, or activities, of pairwise contact and hinge-pivot events were determined using a crossing buffer of 6.0–7.0 Å. Trajectories were preprocessed by stripping the solvent, hydrogens, Zn^{2+} ions, and RNA, if present, and culling trajectories by extracting frames at 10 ns intervals. RMS fluctuations were calculated using sliding windows of 10 and 25 frames. Contact residue and hinge-pivot activity were evaluated by Pearson projection using 10 and 25 siding windows. Additional details on the TimeScapes routines and their application can be found at http://www.timescapes.biomachina.org/. Images were created with VMD version 1.9.3[296] and PyMol version 2.3.4[297].

Results and Discussion

MD simulations of the reduced ZF456 - 5S RNA complex

The reduced Zn^{2+}-bound ZF456–5S RNA complex is stable over 12 μs with minor conformation changes occurring during the first half of the simulation (Figure 22A, B) similar to previous 50 ns simulations of a ZF456 – 61mer 5S RNA initiated from the crystal structure (PDB: 1UN6).[28] The ZF456-RNA interactions found in the MD simulation are generally

consistent with NMR studies.[287] For example, the ^{117}KKHNQ^{121} sequence at the beginning of the ZF4 α-helix (Figure 21C) and Lys123 recognize loop E through electrostatic interactions with the ribose and the phosphate backbone (Table A1). Hydrogen bonding between the Asn120 backbone and O6 of G26 is significantly populated (~83%) in simulations and supported by additional interactions between the sidechain and the phosphate of G41 and A42 (~7-23%). The His119 backbone donates a hydrogen bond to the G26 N7 atom (~91%) (Figure 23). However, the low population of the hydrogen bond between His119 sidechain and G41 nucleobase (~11-12%) suggests that it may not be structurally important in agreement with the X-ray structure[290]. While the NMR data suggest a potential hydrogen bond network involving the η-hydroxyl of Tyr105, the 2′ hydroxyl of G26, and O6 of G41, which is disrupted by a Mg^{2+} ion in the crystal structure, this interaction has an insignificant population (<3%) in the current simulations.

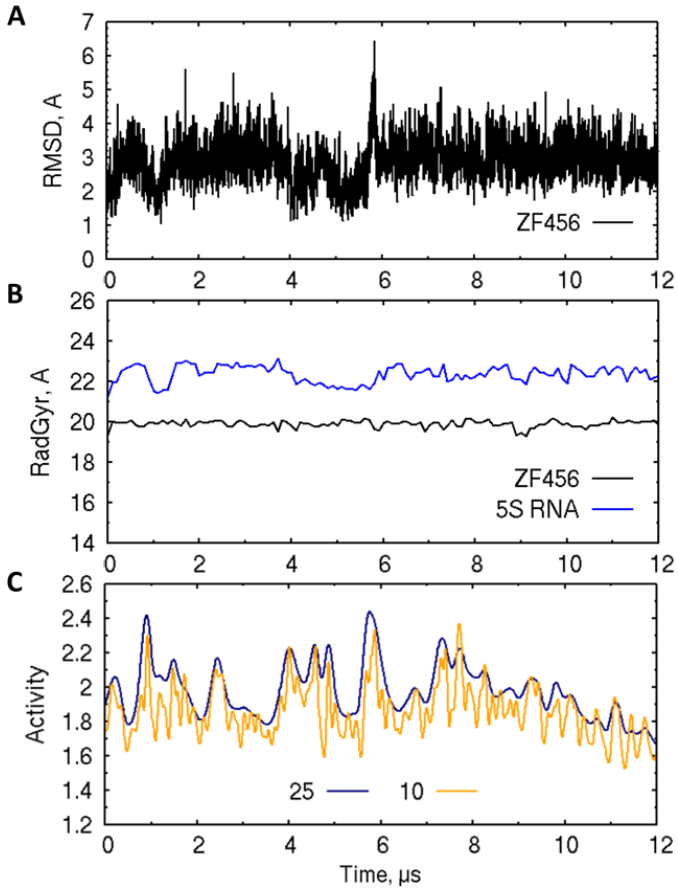

Figure 22. Analysis of the ZF456-5S RNA trajectory. (A) RMSD for ZF456 calculated in terms of Cα. (B) Radius of gyration for ZF456 and 5S RNA. (C) Comparison of filtering on the RMS fluctuations using 25 and 10 sliding windows. TimeScapes trajectory analysis of the ZF456 peptide indicates that the highest portion of events prevails in the first half of the simulations consistent with the RMSD profile for Cα atoms.

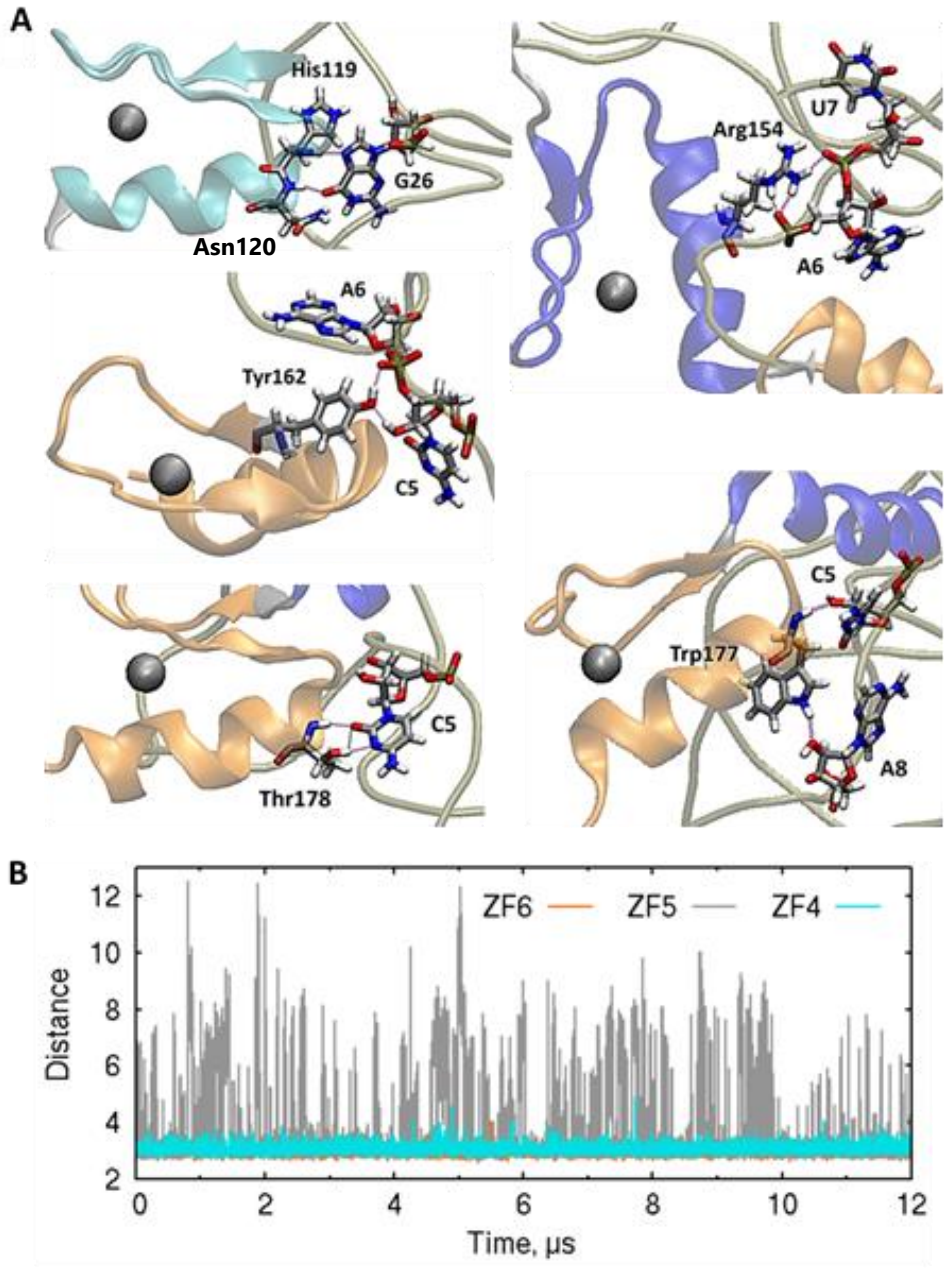

Figure 23. Hydrogen bond analysis for the ZF456-5S RNA complex. (A) MD structures and (B) selected distance measurements for hydrogen bonds that characterize the ZF456-5S RNA complex. The following hydrogen bond distances are plotted for ZF4, ZF5, and ZF6: His119 BB – G26 N7, Arg154 SC – U7 PO_4, and Thr178 BB – C5 O2, respectively.

The basic residues clustered primarily in the α-helix of ZF5 (Lys144, Arg151, Lys153, Arg154, and Lys157) were proposed to interact with the phosphate backbone or ribose hydroxyl groups of helix V and loop A either electrostatically or via hydrogen bonding.[287] In MD simulations, the Arg154 sidechain forms the most populated hydrogen bonds with the phosphates of A6 and U7 in loop A (29-60%, Figure 23, Table A1). The Arg151 guanidine intermittently hydrogen bonds (<28%) with the U20 and G21 phosphates of helix V but seldom interacts with loop A, in contrast to previous MD simulations.[268] Lys157 and Lys144 ε-amino groups form transient hydrogen bonds with the phosphate groups of A6 (or nucleobase) and C19, and C4 and C5, respectively (Table A1). In addition, low-population (~19%) hydrogen bonding between the $N^{\delta}H$ of His155, the first Zn-coordinating histidine in ZF5, and the phosphate of C5 is consistent with NMR observations[287]. However, Lys153 does not participate in any structurally relevant intermolecular hydrogen bonding (<0.2%) despite its proximity to helix V and loop A in NMR studies[287].

ZF6 interacts with three out of four residues of loop A (^{5}**CA**U**A**^{8}) 5S RNA through Tyr162 in addition to Trp177 and Thr178 of the TWT motif (Figure 23, Table A1) in partial agreement with experimental results.[287,290] Tyr162 also donates a hydrogen bond to the A6 phosphate in addition to accepting a hydrogen bond from the C5 ribose as observed by NMR. Trp177 backbone and sidechain hydrogen bond with the C5 and A8 riboses, respectively. The flanking Thr residues, Thr176 and Thr178, donate one and three hydrogen bonds, respectively, to the N3 and O2 atoms of the C5 base in good agreement with the ZF456-5SRNA crystal structure[290] (Figure 23). Thr176 SC's interaction with N3 of C5 was not described in the NMR structure probably due to its intermittent nature (the acceptor-donor distance is ≤ 3.3 Å in only ~30% of the frames). The Thr176 $O^{\gamma}H$ – C5 N3 distance is maintained within 4.5 Å over the

simulation so it can be classified as a native contact consistent with previous MD simulations.[268] Therefore, the ZF456-5S RNA complex relies on fourteen key hydrogen bond interactions (Table A1) which are individually populated for at least 40% of the frames. Half of these bonds involve ZF6, which emphasizes its critical role in 5S RNA binding to TFIIIA.

MD simulations of the free reduced ZF456

MD simulations were performed to determine the conformation dynamics of the free ZF456 peptide. Because NMR studies indicate that His119 becomes protonated upon RNA binding, separate simulations were performed with His119 in the neutral (*ZF456n*) and protonated (*ZF456p*) states. While individual ZF domains remain rigid during simulations as previously reported,[268] the overall ZF456 peptide undergoes significant conformational change (RMSD of ~4 to 16 Å, Figure 24A) due to the reorientation of the ZF regions consistent with the experiment.[268,298] In the TimeScapes trajectory analysis, the transition regions between conformations yield the largest number of events (Figure A2). Pivot angles of the linkers and adjacent residues dominate the hinge-bending motions, confirming the localized nature of the rearrangements and the stability of the Zn^{2+}-bound ββα-fold (Figure A2). While the ZF4-ZF5 linker (^{130}TQQLP^{134}) folds to cap the C-terminus of ZF4 α-helix upon RNA binding, the Phe127-Gln131 hydrogen bond and hydrophobic packing between Phe127 and Leu133 that stabilize the cap become disrupted in free ZF456 (Figure A3) due to ZF5 reorientation. As a result, hydrophobic residues (e.g., Leu148) critical for DNA binding are exposed allowing the peptide to adopt conformations compatible with interactions with both nucleic acids.[268] The Gly161 linker between ZF5 and ZF6 hydrogen bonds to Lys157 which stabilizes the linker structure

together with the hydrophobic packing of Val158, Tyr162, and Thr176.[287] In the absence of RNA, the hydrogen bond is weakened and the hydrophobic packing disrupted (Figure A3).

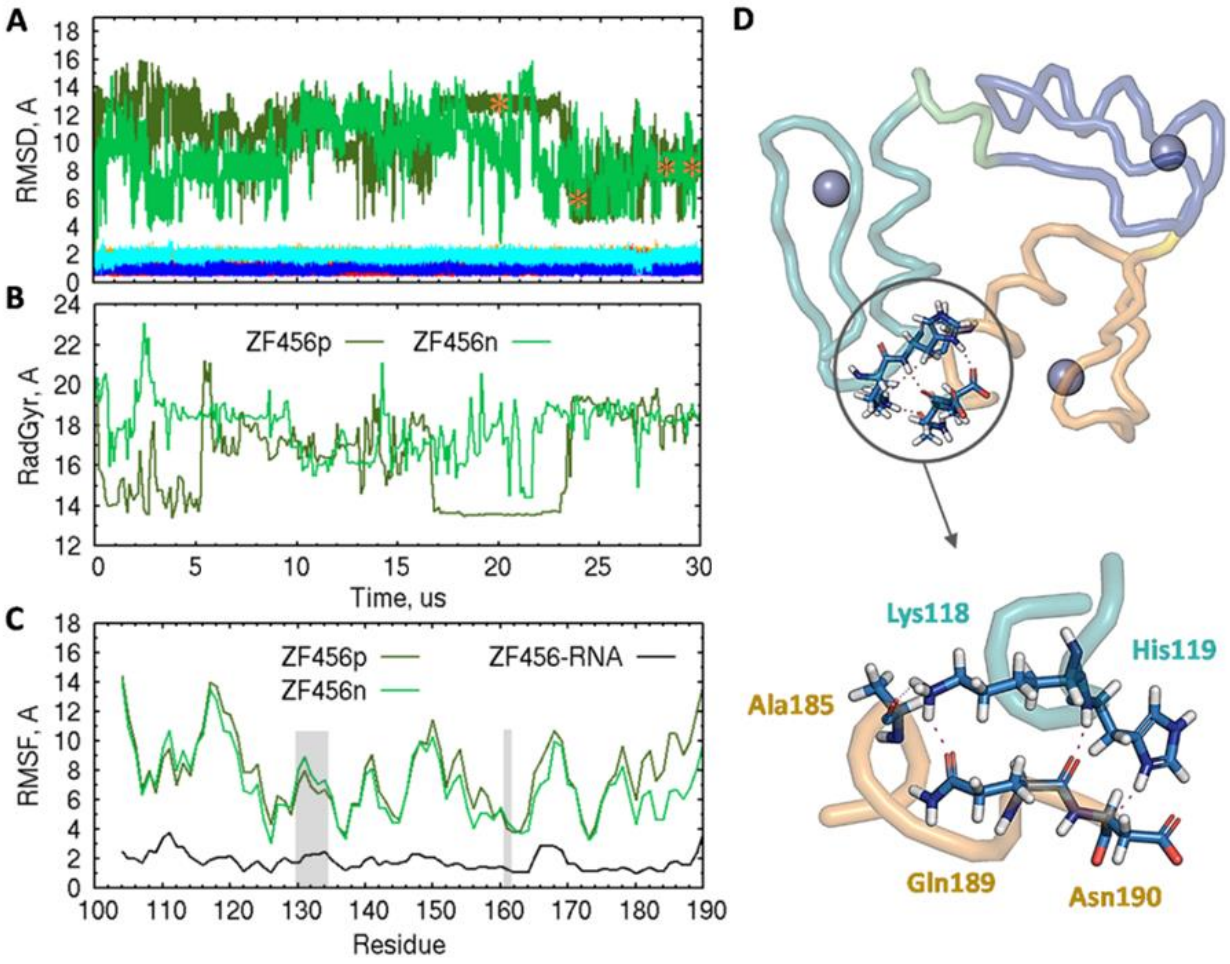

Figure 24. Analysis of trajectories of the free ZF456. (A) RMSD for *ZF456p* and *ZF456n* calculated in terms of Cα atoms. The average RMSD for individual ZFs is ~1-2 Å. The asterisks (*) indicate the time at which the key structures shown in Figure 25 are taken. (B) Radius of gyration and (C) RMSF of Cα for the simulation of *ZF456n* and *ZF456p*. RMSF for ZF456 bound to RNA are significantly less mobile by comparison. The linker residues are in gray boxes

to help distinguish between individual ZF domains. (D) *ZF456p* structure at 20 μs showing interactions between ZF4 residues at position -1 and +1 and ZF6 C-terminus residues.

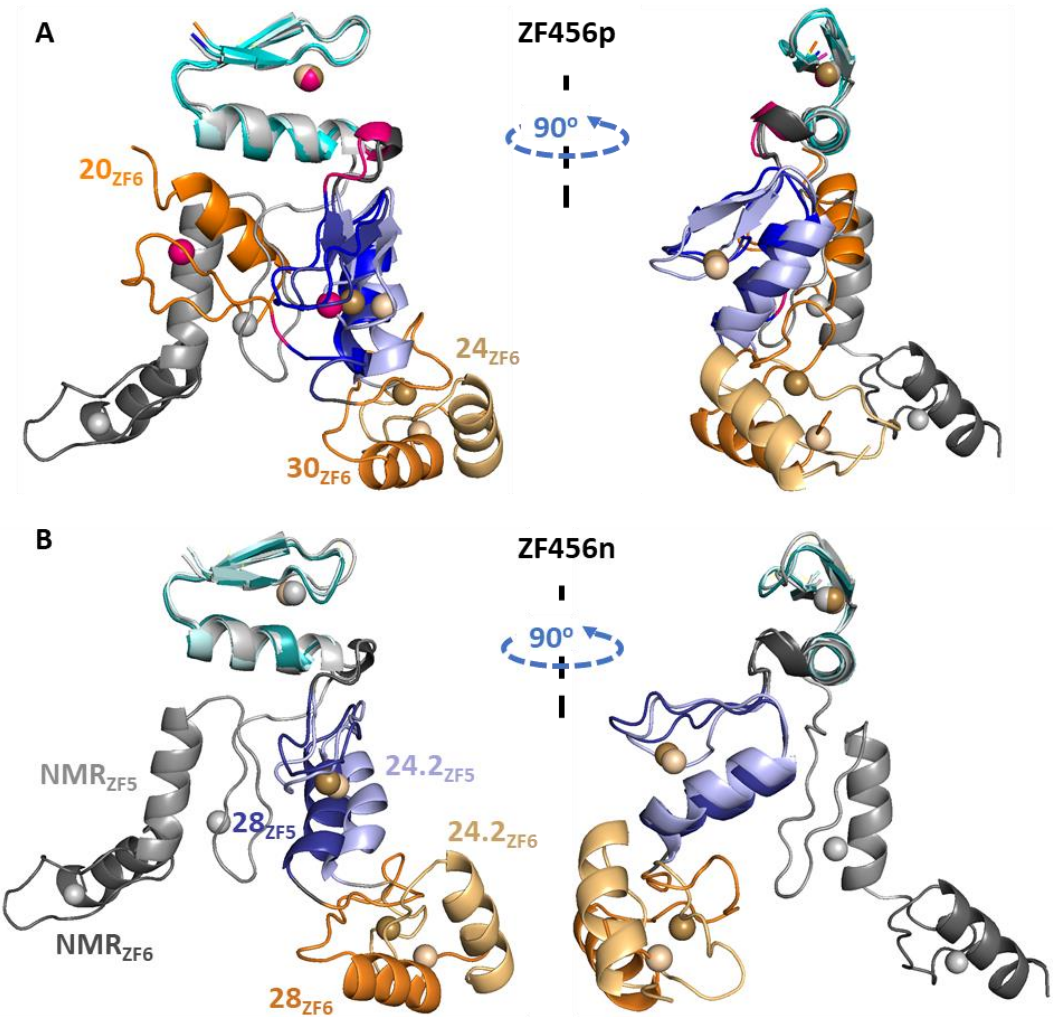

Figure 25. Superimposed (A) *ZF456p* and (B) *ZF456n* structures of key conformations, taken at 24, 30, and 20 μs (p) and 24.2 and 28 μs (n). The conformations of ZF4 were fitted to the NMR structure (gray).

A long-lived conformation of *ZF456p* detected at ~17 μs coincides with the closing of the interface between ZF5 and ZF6 (Figure 24 and A4). An inverse interdomain motion (opening of the ZF5-ZF6 interface) was previously observed during the short MD simulations.[268] Here, the structural organization is accompanied by a sharp decrease in events (Figure A2) and relatively high RMSD values (Figure 24A). This conformation is stabilized by hydrogen bonding interactions between ZF4 α-helix residues at positions -1 (Lys118) and +1 (His119) and ZF6 C-terminal residues Ala185, Gln189, and Asn190 (Figure 24D). An additional hydrogen bond between His139 and the ZF5-ZF6 linker residue Gly161 contributes to a ~30% decrease in the protein's compactness (Figure 24B). This conformation is unstable because ZF45 rotates around Gly161 breaking compactness-promoting hydrogen bonds and increasing protein's radius of gyration as it searches for a more favorable conformation for nucleic acid binding. During the last several microseconds, *ZF456p* appears to alternate between two conformations (Figure 24B and 5), *ZF456p-A* and *ZF456p-B* (i.e., at 24 and 30 μs, respectively) as does *ZF456n* (i.e., *ZF456n-C* and *ZF456n-D at 24.2 and 28 μs, respectively).* The conformations *ZF456p-A/ZF456n-C* and *ZF456p-B/ZF456n-D* are similar between the protonation states (RMSD ~2.4 Å) and rely on a moderate conformation change at the ZF5-ZF6 interface. Regardless of the protonation state of His119, the highest molecular motion occurs within ZF4 (Figure 24C), particularly at the fingertip of the ββα-fold known to interact with RNA (^{117}KKHNQ^{121}) in agreement with trajectory analysis using the TimeScapes package (Figure A2). The least mobility is observed for the β-hairpin of ZF5 and ZF6 and His residues in the Zn^{2+} coordination sphere.

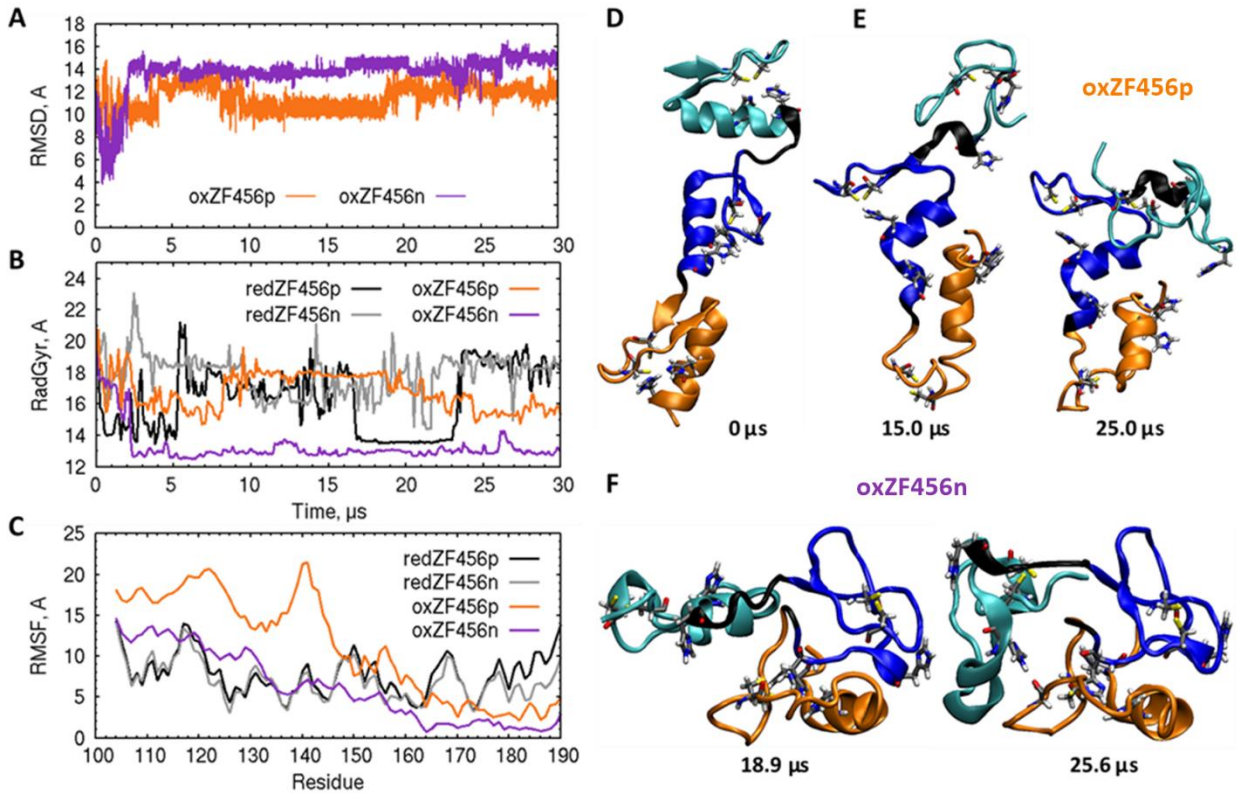

Figure 26. Analysis of the free oxidized ZF456 trajectories. (A) RMSD of Cα for *oxZF456p* and *oxZF456n*. Comparison of (B) radius of gyration and (C) RMSF of Cα for the simulation of oxidized ZF456 and reduced ZF456 peptides. (D) Structure of ZF456 at t = 0 μs. Snapshots from the simulation of (E) *oxZF456p* and (F) *oxZF456n*, all three ZFs lose the β-fold completely during the simulation. The ZFs are depicted as cartoon and colored in cyan (ZF4), blue (ZF5), and orange (ZF6).

MD simulations of the oxidized free ZF456

Oxidized ZF456 peptides are more conformationally dynamic relative to the free Zn^{2+}-bound peptides (Figure 26A). For *oxZF456p* significant changes in the ZF4-ZF5 interface occurs before it equilibrates and widely opens at ~10 μs (Figure A5). ZF4 starts to slowly fold over ZF5

after approximately another seven microseconds, reducing the protein's gyradius (Figure 26B, E). The interface between ZF5 and ZF6 adjusts to a new position as a result of a bent within the ZF5 α-helix (after His155). In contrast, *oxZF456n* becomes globular earlier in the simulation. Association of ZF5 and ZF6 and extension of the TQQLP linker to allow ZF4 to cap the globular shape decreases the protein's gyradius by ~35 % (Figure 26B, F). This conformation is stabilized by interdomain (i.e., Trp180 SC – Glu156 BB and Lys123 BB – Glu161 BB, 93% and 40% population over the last 12 μs, respectively, Figure A6) and intradomain (with a population as high as 94% for Pro163 BB – His188 BB) hydrogen bonding interactions. As a result, the hydrophilic residues in *oxZF46n,* but not in *oxZF456p,* are facing toward the peptide's interior in contrast to a typical/"true" globular structure where these residues are generally surface exposed. However, the key hydrophilic residues for 5S RNA binding are located at the surface but are not positioned to interact properly.

The individual ZF domains of oxidized ZF456 undergo various degrees of unfolding due to the loss of the structural Zn^{2+} ion. These conformational instabilities are reflected in the overall delocalized hinge-pivoting fast motions of the oxidized peptides, in contrast to the reduced ones (Figure A2). In *oxZF456p,* ZF4 and ZF6 which recognize the 5S RNA loop E and A, respectively, reach equilibrium RMSD values of ~7.0 Å. ZF4 loses most of its ββα-fold consistent with its large hinge-bending motions identified in the TimeScapes trajectory analysis (Figures A2 and A7). ZF5 deviates least from the reduced structure (RMSD ~ 3.5 Å) attributed to a decrease in α-helicity. Meanwhile, ZF6 loses its β-folds containing the key Tyr162 residue and increases its α-helical region toward the N-terminus to Gly174 from β-sheet (Figure A7). In *oxZF456n,* where His119 is in the NMR-suggested protonation state for the unbound protein,[287] all three ZFs undergo significant structural change (RMSD of ~6–8 Å). The β-hairpin in ZF4 and

ZF6 unfolds completely, and the α-helix content is diminished at the termini where key RNA-binding residues (i.e., His119 and Trp177) are positioned. ZF5 retains half of its β-folds intact but loses its α-helical structure whose residues would interact with the RNA phosphate backbone (Figure A7).

MD simulations of the oxidized ZF456 - 5S RNA complex

To determine how disulfide formation and loss of Zn^{2+} could affect the ZF456 interaction with RNA, simulations were initiated from a bound conformation of the reduced Zn^{2+}-bound ZF456 – 5S RNA complex (PDB: 2HGH). Over the course of 30 μs simulations, the oxidized ZF456 peptides *oxZF456n* and *oxZF456p* lose the stabilizing hydrogen bonds that bind the reduced peptide to RNA. As a result, both peptides become more elastic in their interactions with RNA with *oxZF456p* experiencing fewer conformational changes compared to *oxZF456n* (average RMSD = ~5 Å vs ~10-11 Å, Figure 27B). ZF4 in *oxZF456p* loses its β-hairpin and a half-turn of the α-helix but becomes stabilized by new hydrogen bonds between the Met104 and Val106 BBs and Gln126 SC. ZF4 residues lose their secondary structure to dominate the hinge-bending motions of *oxZF456p* peptide (Figure A8 and 28D). ZF5 retains its ββα-fold whereas the ZF6 C-terminus residues partially lose their α-helical structure (Figure A8). However, the hydrogen bonds within the β-hairpin of ZF5 and ZF6 are present throughout the simulation. Consistently, *oxZF456p*'s radius of gyration decreases by up to 8% in the first 10 μs of the simulation before returning to its initial compactness by the 15th microsecond (Figure 27C). On the other hand, *oxZF456n* continuously rearranges such that no long-lived conformation is detected during the 30-μs simulation. *OxZF456n*'s compactness is similar to *oxZF456p* during

the first ~19 μs, but it fluctuates significantly afterward for radii of gyration ranging from 15.1 Å (-22 %) to 22.0 Å (+14 %) (Figure 27C).

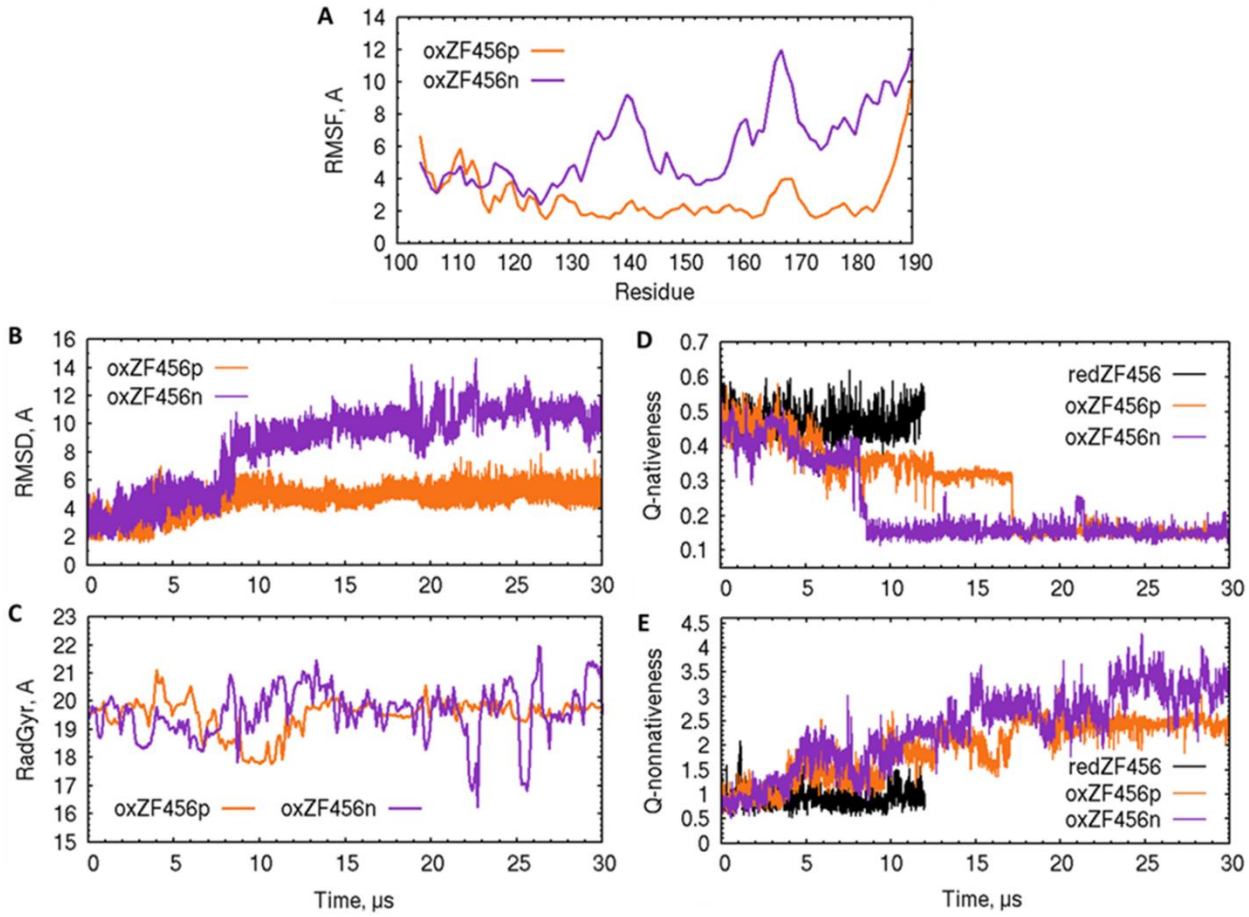

Figure 27. Analysis of the oxidized ZF456 trajectories in the presence of 5S RNA. (A) RMSF of Cα, (B) RMSD of Cα, and (C) radius of gyration for the simulation of oxidized ZF456. Comparison of the (D) native-ness and(E) nonnative-ness Q-values of the reduced and oxidized ZF456-5S RNA.

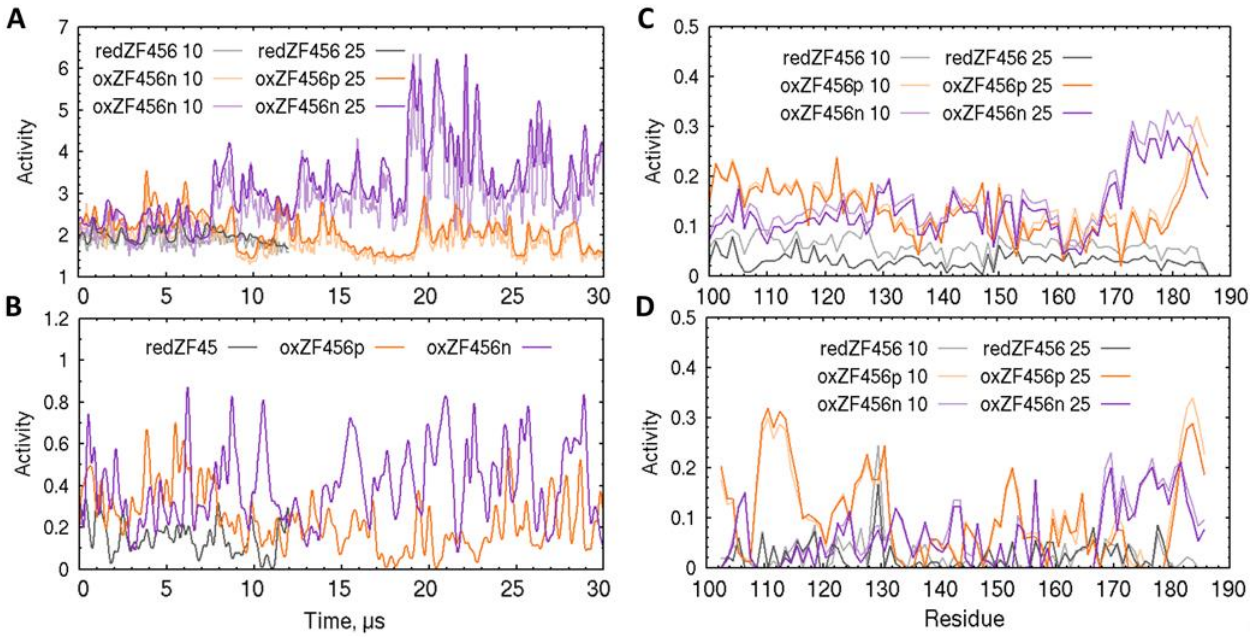

Figure 28. TimeScapes trajectory analysis of reduced and oxidized ZF456 in the presence of 5S RNA. (A) Comparison of filtering on the RMS fluctuations using 25 and 10 sliding windows. (B) Event detection activity determined by cutoff- (6.0–7.0 Å crossing buffer) screening using the 25-frame screened trajectory. (C) Contact residue and (D) pivot angle activity determined by Pearson projection using 25 and 10 sliding windows.

TimeScapes trajectory analysis detected greater event activity in the simulation of *oxZF456n* than *oxZF456p* consistent with the trends in RMSD (Figure 28B). The RMS fluctuations profile of *oxZF456n* (Figure 28A) reflects the dynamic nature of the peptide starting at ~19 μs associated with loss of the ZF5 β-hairpin (Figure 27C and A8). ZF4 in *oxZF456n* succeeds at maintaining almost intact its ββα-fold (one intra-strand hydrogen bond is lost) coinciding with low RMSD (~2 Å), contact residue, and pivot angle activity (Figure A9 and 28C, D). The α-helical content of ZF5 drops early in the simulation, whereas the β-sheet is retained for

the first ~19 μs. ZF6 undergoes a high degree of unfolding, reflected in the contact residue activity and associated with rearrangement of residues at positions -3, -2, and -1 from β-strand (Gly174) or bend (Arg175 and Thr176), respectively, into a destabilized α-helix (Figure 28C and A8). Both *oxZF456p* and *oxZF456n* follow different trends in RMSD profiles of individual ZFs (Figure A9). In the former, ZF4 is the most flexible (RMSD ~ 4.5 Å at equilibrium), followed by ZF6 which adopts fewer conformations. The RMSD for ZF5 stays constant and averages ~1.3 Å over the simulation. For *oxZF456n*, ZF5 and ZF6 fluctuate significantly with RMSD values up to 12.0-14.0 Å, while ZF4 remains constant similar to ZF5 in o*xZF456p* averaging ~1.8 Å.

These conformation changes shown in RMSD profiles (Figure A9) are related to the disruption of most key hydrogen bonding interactions between ZF456 and 5S RNA upon disulfide bond formation (Table A1). In *oxZF456p*, the hydrogen bonds between RNA and ZF4 and ZF5 drastically weaken over the first 12 μs (the population drops by 28-74%). ZF4 retains the His119 BB – G26 N7 hydrogen bond (although the population drops by 54.9%). The loss of Asn120 BB interaction with G26 O6 at ~6.0 μs is compensated with the formation of new ones between Asn120 SC and adjacent Lys and loop E/helix V phosphate backbone (~40-48% population during the first 12 μs, Table A2). Within ZF5, Arg154 guanidine loses its interactions with A6 but retains those with the U7 phosphate. The disruption of the hydrogen bonds between ZF5 and RNA phosphates is due to the shift of ZF5 relative to the RNA than to any conformational variations within this finger. In contrast, ZF6 loses only one out of the seven hydrogen bonds present in the reduced Zn^{2+}-bound form (Table A1). The interaction between Thr178 $O^{\gamma}H$ and C5 O2 strengthens by 36% (89.5% vs 65.8% population) at the expense of the Thr178 $O^{\gamma}H$ - C5 N3 bond, which forms in 50% fewer frames in comparison with the reduced system. During the last 12 μs, all key hydrogen bonds are lost (Table A1). The base-specific

interactions of ZF4 and ZF6 with loop E and A, respectively, are replaced by nonspecific interactions. For example, ZF4 Lys residues, Tyr105 and Gly113 BB hydrogen bonds to loop E and the adjacent RNA helixes (Table A2). His119 and Asn120 form interactions of <40% population with G26 N7 and U23 phosphate, respectively. Arg residues within the shifted ZF5 make contacts with the helix V phosphate backbone. ZF6 Trp177 and Thr178 backbones interact with the A6 phosphates throughout at least 85% of the last 12 μs and each side chain forms a highly populated interaction with loop A C9 sugar (76.9%) and A6 phosphate backbone (96.6%), respectively (Table A2).

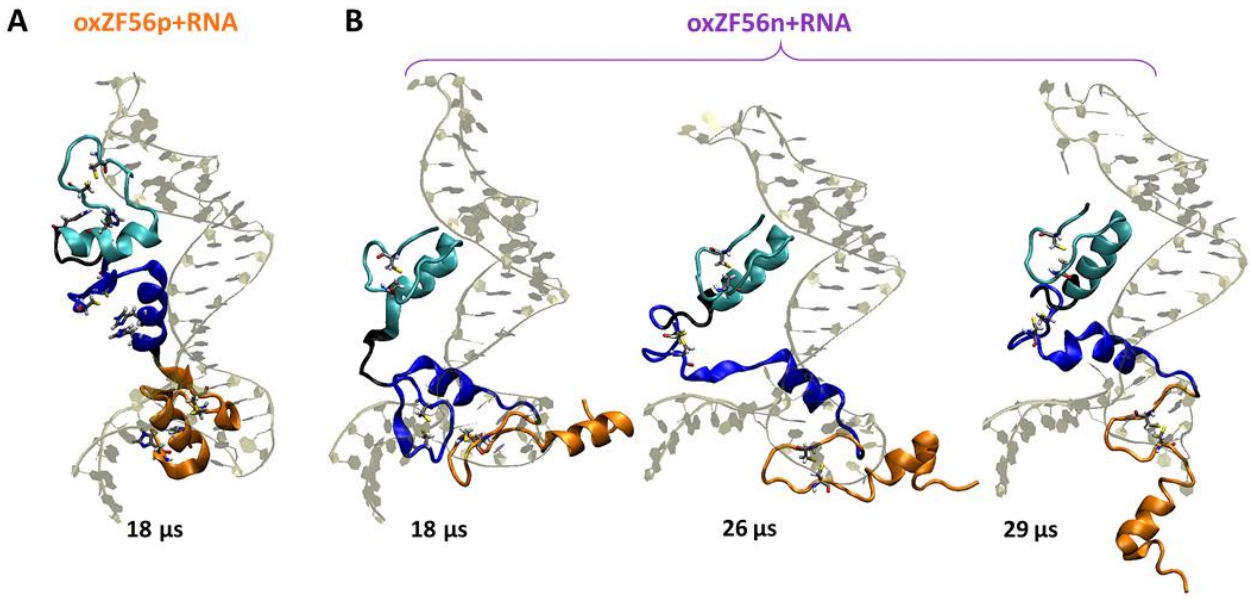

Figure 29. Snapshots from the simulation of (A) *oxZF456p* - 5S RNA and (B) *oxZF456n* - 5S RNA. The three zinc fingers are depicted as cartoon and colored in cyan (ZF4), blue (ZF5), and orange (ZF6). 5S RNA is shown in tan.

In *ox-ZF456n,* ZF4 retains its hydrogen bonds with G26 and maintains the RNA binding through multiple nonspecific interactions from the sidechain of Lys117, Lys123, and Gln121 to loop E/helix V (Tables A1 and A3) during the first 12 μs. In contrast, the population of all key hydrogen bonds between ZF5 and ZF6 and loop A decline by ~30-61% over the course of the first 12 μs. Only Arg154 in ZF5 forms new interactions with the loop A phosphate backbone, though with different groups than in the reduced environment ($N^{\eta 1}H$ and $N^{\eta 2}H$ vs $N^{\eta 2}H$ and $N^{\varepsilon}H$). Additionally, several transient hydrogen bonds develop between Arg and Lys residues and loop A/helix V to support the RNA binding by ZF5. ZF6 residues do not form new interactions with 5S RNA to compensate for the weakening of its key hydrogen bonds in the first 12 μs (Tables A1 and A3). In contrast to *oxZF456p,* ZF6, not ZF4 undergoes the greatest conformational changes and loses the most hydrogen bonds (Table A1 and Figure A9). Over the last 12 μs, the population of key His119 BB – G26 N7 interaction decreases to ~62% (vs 91%) but the Asn120 BB – G26 O6 hydrogen bond strengthens (~%97 vs ~83% population). All interactions of ZF4 newly formed in the first 12 μs are maintained throughout the simulation. Additionally, three hydrogen bonds between Lys114, Asn120, Gln121 SC and loop E/helix V contribute to >40% of the frames (Table A3). ZF5 and ZF6 lose their key hydrogen bonds to the loop A phosphate and nucleobases, respectively by the end of the simulation (Table A1). The side chains of Lys and Arg residues within the α-helix of ZF5 form nine highly populated hydrogen bonds with the phosphate backbone of loop A/helix V that are not found in the reduced peptide – RNA complex. Within ZF6, new interactions involving Tyr162 and two residues within the β-turn, Lys166 and Asp167, are established with loop A and helix V instead (Table A3). Presumably, these three hydrogen bonds assist the other two ZFs in maintaining RNA bound to the ZF456 peptide. Disulfide formation and Zn^{2+} loss forces ZF6, the important finger

for RNA binding, to lose its secondary structure and ability to interact with RNA. In contrast, despite losing the proper ββα fold, ZF5 can still play its role as a spacer-element in the RNA binding process. ZF5 non-specific but secure interactions may allow ZF4 to lock in place and maintain its base-specific interactions despite being partially unfolded (Figure 29B and A8).

To gain a broader understanding of the interactions between oxZF456 and 5S RNA, the native contacts were tracked for the course of the simulations for comparison with the reduced Zn^{2+}-bound RNA complex. Any protein-RNA contact within 4.5 Å in the initial (NMR) structure was defined as a native contact. Any new protein-RNA contact meeting the distance cutoff (4.5 Å) that formed during the simulations was defined as non-native. Using the initial number of these contacts, the fraction of (non)native contacts or Q-(non)nativeness was calculated throughout the simulations (Figure 27D, E). The *oxZF456p* peptide loses approximately 20% (in comparison to reduced *ZF456p*) of native contacts with RNA after 6 μs coinciding with the first significant reduction in its compactness (Figure 27C, D). An additional ~20% of contacts are lost at 17.5 μs when a short-lived conformation, defined by RMSD of the highest values and radius of gyration at a local minimum, is detected. The native contacts of *oxZF456n* are gradually lost in the first 8 μs followed by a rapid decline of 30% consistent with a sharp increase in RMSD (Figure 27B, D). Despite failing to retain most native contacts, both *oxZF456p* and *oxZF456n* do not dissociate from RNA over the timescale of the simulation (Figure 29) due to the increase in non-native contacts (Figure 27E) and non-specific hydrogen bonds throughout the simulations. Full dissociation might be observed over longer time scales given a solvent box capable of accommodating separated ZF456 and RNA.

Conclusions

ZFs are an important class of proteins that participate in the regulation of several cellular processes. Targeting ZF proteins involved in the survival and progression of cancer cells or part of viral replication and transcription mechanisms is a promising strategy for cancer treatment or viral inhibition. Multi-μs MD simulations examined the effect of Cys oxidation on ZF proteins and the interaction of oxidized ZFs with nucleic acids at the atomistic level. The central zinc finger sequence (ZF456) of TFIIIA interacting with 5S RNA was used as a model for this study and two sets of protonation states were included for the His residues outside the Zn^{2+}-coordination sphere.

In the absence of RNA, the reduced ZF456 peptides undergo conformational changes involving the linker and adjacent residues as shown by trajectory analysis. Individual ZF domains remain rigid and the ββα-fold intact, but the interactions within the linker structures (^{130}TQLLP^{134} and Gly161) are disrupted. Additionally, a long-lived compact conformation of *ZF456p* detected about halfway through the simulation and characterized by interdomain hydrogen bonding is incompatible with nucleic acid binding. Potential pH dependence in the conformation dynamics of reduced ZFs could be addressed through explicit solvation constant pH MD simulations. However, late in the simulation, *ZF456n* and *ZF456p* alternate between two conformations consisting of an extended chain of ZF domains compatible with both 5S RNA and DNA binding.

Upon Zn^{2+} loss and disulfide bond formation, conformational dynamics within the free oxidized ZF456 peptides increases considerably to populate conformation incapable of RNA recognition. The interfaces between ZF domains in *oxZF456p* fluctuate significantly prior to ZF4 folding over ZF5 and ZF6 adopting a new position relative to ZF5. However, the ZF domains in

oxZF456n associate into a globular structure early in the simulation assisted by highly populated inter- and intra-domain hydrogen bonds (i.e., Trp180 SC – Glu156 BB and Pro163 BB – His188 BB. The individual ZFs unfold in both peptides to various degrees resulting in delocalized hinge-pivoting fast motion. Most of the ββα-fold unravels in fingers that make base-specific interactions with RNA – ZF4 and ZF6, but ZF5 loses only the α-helix which forms the non-specific interactions. Due to this unfolding, the peptides lack the secondary structure to recognize nucleic acids.

In the reduced Zn^{2+}-bound ZF456-5S RNA complex, the hydrogen bond analysis agrees well with the experimental data showing that ZF456 uses Tyr162, Trp177, and Thr178 in ZF6 (seven hydrogen bonds), Arg154 in ZF5 (three hydrogen bonds), and His119 and Asn120 in ZF4 (four hydrogen bonds) to interact with the 5S RNA. However, some variations from the experimental results are found. NMR-suggested interactions of ZF4 with G41 and ZF5 Lys residues with helix V/loop A appear transiently in the MD simulation and may not be relevant to the 5S RNA binding of TFIIIA. Also, Arg151 does not make hydrogen bonds with loop A as seen in the previous short MD simulations, but an interaction between ZF6 Tyr162 and the A6 phosphate appears to be important to the binding. The X-ray proposed interaction between Thr176 SC and C5 N3, but absent in the NMR studies, forms intermittently throughout the simulation. Disulfide formation and Zn^{2+} loss diminish the ability of the oxidized ZF456 peptides to recognize RNA. All ZF domains except ZF4 in *oxZF456n* lose key hydrogen bonds and native contacts found in the reduced Zn^{2+}-bound ZF456-RNA complex consistent with reduced binding affinity and impaired recognition. This loss of key protein – RNA interactions and the conformational flexibility of the oxidized peptide demonstrate the structural importance of Zn^{2+} to the ZF secondary structure and ZF recognition mechanisms.

CHAPTER IV

DFT MODELING OF THE PREVENTION OF FE(II)-MEDIATED REDOX DAMAGE BY IMIDAZOLE-BASED THIONES AND SELONES[a]

Introduction

Reactive oxygen species (ROS) are byproducts of cellular respiration and act as messengers at low concentrations.[103,299–301] If not controlled, these species damage cellular components including proteins, lipids, and nucleic acids.[208,300,302–307] Lipids and proteins are rapidly replaced during cellular maintenance, but recovery of lost information stored in DNA is difficult which makes it a critical biological issue. Despite numerous cellular DNA repair mechanisms, cumulative DNA damage contributes to aging, Alzheimer's disease, cardiovascular disease, and various forms of cancer.[308–315] Accordingly, the behavior of free radicals in biological systems has been a recent area of significant interest.[316–318] The most damaging ROS is the hydroxyl radical (·OH)[319] produced by Fenton and Fenton-like chemistry between hydrogen peroxide and transition metal ions such as Fe(II) and Cu(I) (eq. 14).[118,320] Density functional theory (DFT) studies have examined several pathways for Fe(II)-mediated generation of hydroxyl radicals.[321–324]

$$M^{n+} + H_2O_2 \rightarrow M^{(n+1)+} + OH^- + \cdot OH \qquad (14)$$

---

[a] Reprinted with permission from Dreab, A.; Brewer, M.I.; Bayse, C.A. DFT modeling of the prevention of Fe(II)-mediated redox damage by imidazole-based thiones and selones. *J. Inorg. Biochem.* **2019**, *193*, 9-14. Copyright 2019 Elsevier. The manuscript can be found online at https://doi.org/10.1016/j.jinorgbio.2018.12.015.

Metal-mediated ·OH generation is proposed as a major cause of DNA damage and cell death through apoptosis.[325–328] Single-strand break and nucleobase oxidation are commonly studied types of Fe(II)-mediated DNA damage.[329] Fe(II) is believed to travel along the phosphate backbone to coordinate to DNA at N7 of guanine,[330] the most easily oxidized nucleobase.[331] The intermediate product 8-oxo-deoxyguanine is commonly used as an oxidative damage marker because it can be detected in the femtomolar range.[329] Fe(II)-mediated DNA damage occurs preferentially at certain sequences (i.e., RGGG or RTGR).[330,332,333] Lee et al. have shown that GTGR is also a sensitive sequence for oxidative damage.[334] Radical scavengers such as ethanol and dimethyl sulfoxide inhibit Fe(II)-mediated DNA damage in vitro, by preventing hydroxyl radical-induced nicking of the phosphate backbone or oxidation of guanine.[335] Enzymatic radical scavenging has limited effectiveness in combating hydroxyl radicals formed in locations too hindered for effective access by scavenging systems.[320,336] As a result, prevention of metal-mediated radical formation may be a superior approach to protecting against oxidative damage.[337]

In vitro studies have shown that sulfur and selenium compounds protect DNA from metal-mediated damage.[107,124,337–341] Seven of nine selenium compounds tested prevented Cu(I)-mediated oxidative DNA damage, while only five inhibited Fe(II)-mediated damage.[119–121] Interestingly, only N,N′-dimethylimidazole selone (**3Se**) prevented significant Fe(II)-mediated DNA damage within selenium's biological range (3.2 μM).[337] In contrast, eight of eleven sulfur compounds tested inhibited Cu(I)-mediated DNA damage with IC_{50} values from 3.34 to 1550 μM, but only three compounds prevented Fe(II)-mediated DNA damage, among which glutathione inhibited only 23% of damage.[337] N,N′-dimethylimidazole thione (**3s**) inhibited Cu(I)-mediated damage at a substantially higher concentration than **3Se** (IC_{50}: 1550 μM vs. 240

μM).[337] Ergothioneine has shown significant free radical scavenging capacity but has not been tested for the prevention of metal-mediated DNA damage.[342] Overall, sulfur and selenium-containing compounds have shown greater inhibition of Cu(I) over Fe(II)-mediated DNA damage. Thione and selone derivatives are a notable exception with **3S** and **3Se** about 17.3 and 75 times more effective, respectively, against inhibition of Fe(II)-mediated DNA damage.[337]

Since scavenging of the short-lived hydroxyl radical by sulfur and selenium compounds seems unlikely,[10,343] metal coordination has been proposed as the primary mechanism by which these antioxidants prevent DNA damage.[118–121] Protection would occur through sacrificial oxidation of the coordinated thione/selone[122,123] rather than through the direct ROS scavenging observed for a broad range of sulfur and selenium compounds.[124–126] Thiones and selones prefer to coordinate through the zwitterionic resonance form[123,124,344–346] which allows these ligands to be classified as potential π-donors similar to other anionic chalcogen ligands such as thiolates and selenolates.[123,347] The zwitterionic resonance structures suggest that thiones/selones will have longer C–E bonds than "true" chalcogenones, E will carry a partial negative charge, and the heterocyclic ring will be partially positive. Thione/selone coordination to Fe(II) results in higher ligand-based oxidation potentials and significantly more negative Fe(III/II) -derived reduction potentials indicating that thiones/selones would more easily undergo oxidation.[123]

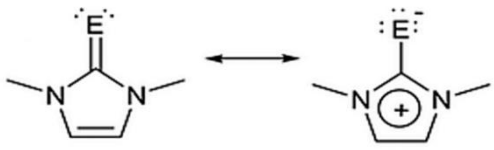

Scheme 1. Chalcogenone resonance structures (E = S/Se).

The effect of thione/selone coordination on the prevention of DNA damage by Fe(II) was investigated through DFT studies of the free ligands and their complexes with Fe(II) coordinated to water and guanine. The contribution of the zwitterionic character of the thiones/selones to the stability of the complexes was analyzed through changes in the C–E bond distances and the relative energies of ligand substitution. The highest occupied molecular orbital (HOMO) character of Fe(II) complexes indicates that localization of the electron density on the ligands rather than the metal provides a potential antioxidant mechanism through sacrificial oxidation of the coordinated thiones/selones.

Computational Methods

Density functional theory (DFT) optimized geometries were calculated using Gaussian 09[164] and the mPW1PW91[160,161] exchange correlation functional. Iron was represented by the Wachters-Hay all-electron basis set.[348] The Wadt-Hay relativistic effective core potential basis set[349,350] augmented with diffuse and polarization functions was used for sulfur and selenium. Carbon, nitrogen, oxygen, and hydrogen basis sets were triple-ζ quality augmented with diffuse and polarization functions. All structures were confirmed as minima on the potential energy surface through inspection of their vibrational frequencies. Wiberg bond indices (WBIs)[162] and Natural Population Analysis (NPA) charges were calculated using Natural Bond Orbital (NBO) version 3.1.[163]

Results and Discussion

DFT geometry optimizations were performed on a series of imidazole-based thiones and selones with increasing methyl substitution (Figure 30). The electron-donating effect of the methyl groups stabilizes the zwitterionic resonance structure (Scheme 1),[123,124,345] resulting in longer C–E bonds and more negative NPA charges on E for the series of five thione/selone derivatives (Figure 31a). The average C–E bond increases by 0.014 Å (thiones) and 0.017 Å (selones) in tetra-substituted compounds compared to **1**s and **1**$_{Se}$, respectively. The NPA charge on E decreases by 0.009-0.016e and 0.007-0.014e with the addition of each methyl group to the thione and selone compounds, respectively. In general, the sulfur of thione derivatives is more partially negative than the selenium centers of their selone counterparts (q_S(**3**s) = -0.281e; q_{Se}(**3**$_{Se}$) = -0.261e). However, the Wiberg bond orders of the selones (**3**$_{Se}$: $WBI_{C=Se}$ = 1.338) are smaller than the thiones (**3**s: $WBI_{C=S}$ = 1.433) indicating that the selenium compounds have a more zwitterionic character in agreement with previous studies.[344,351,352] The HOMOs of methylated thiones/selones are also destabilized (i.e., **1**$_{Se}$ vs **5**$_{Se}$ = -0.19934 a.u. vs -0.18564 a.u.) (Figure 31b), consistent with increased Lewis basicity and stronger metal coordination.

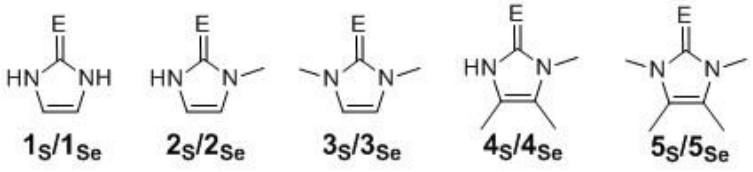

Figure 30. The series of imidazole-based thiones and selones included in this study.

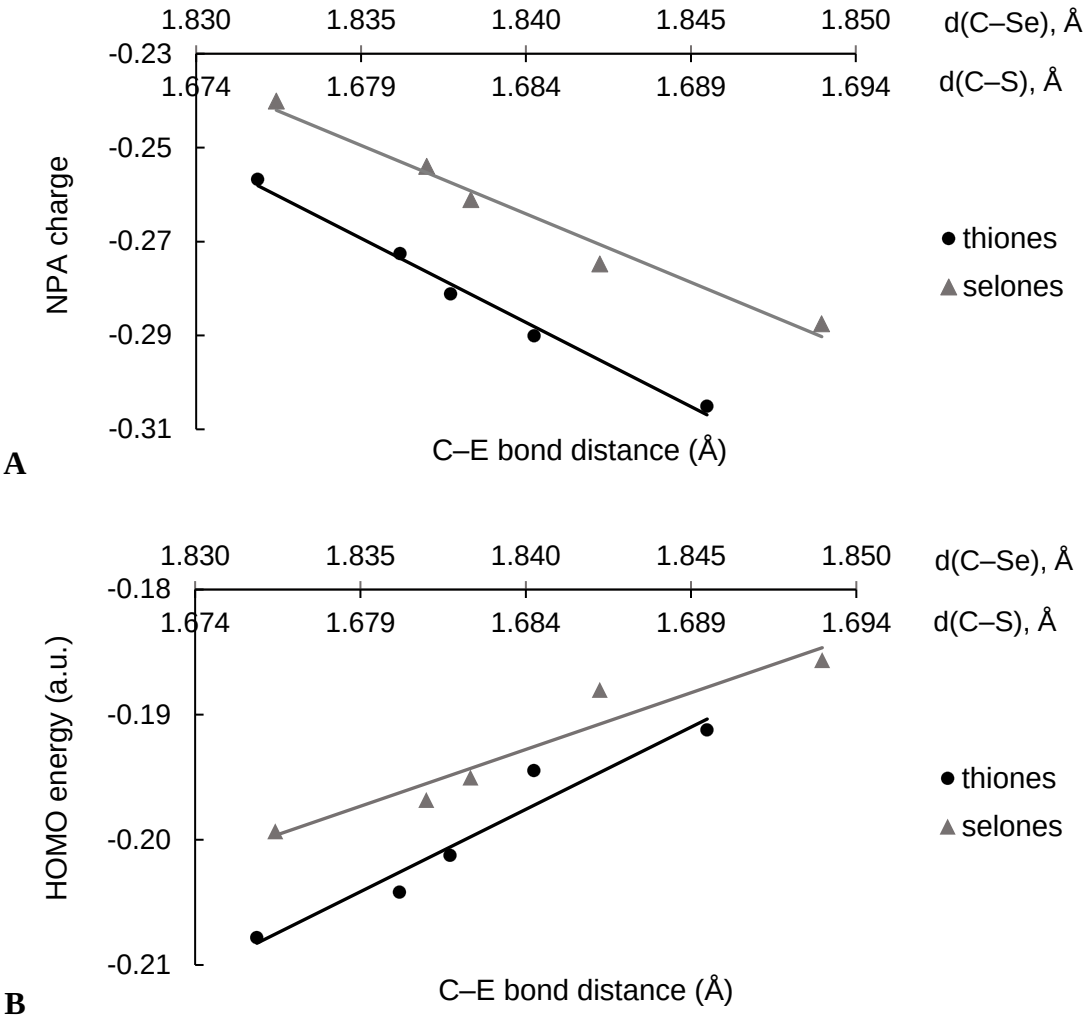

Figure 31. C—E bond distance vs (A) NPA charge on E and (A) HOMO energy of free ligands.

Inhibition of DNA damage may result from the effect of thione/selone coordination on the electronic structure and reduction potential of Fe(II) either as aquated ions or coordinated to guanine. The relative energy of substitution of a water ligand of $[Fe(OH_2)_6]^{2+}$ by a thione/selone according to reaction (15) was calculated to determine trends in the effect of electron-donating methyl groups on the affinity of L for the Fe(II) center.

$$[Fe(OH_2)_6]^{2+} + L \rightarrow [Fe(OH_2)_5L]^{2+} + H_2O \quad (15)$$

The DFT structures of the $[Fe(OH_2)_5L]^{2+}$ (L= thione/selone) complexes were optimized assuming octahedral coordination and a high-spin Fe(II) center. Previously synthesized Fe(II)-thione/selone complexes adopted a distorted tetrahedral coordination geometry, preferred by the two or more weak-field thione/selone ligands (i.e $[Fe(\mathbf{3_{Se}})_2Cl_2]$).[123] For thiones/selones interacting with free Fe(II) at low concentrations, we expect that water, as a small σ-donor ligand, will fill the coordination sphere at low L substitution and favor 6-coordination. However, there is some experimental indication of tetrahedrally coordinated disubstituted Fe(II) ions (i.e., $[Fe(OH_2)_2L_2]^{2+}$)(J.L. Brumaghim, *personal communication*). The optimized structures are roughly octahedral with E-Fe-O_{eq} bond angles ranging from 83.4° to 107.3° (thiones) and from 88.2° to 109.1° (selones). $[Fe(OH_2)_5L]^{2+}$ complexes with L containing an NH group (i.e., **2**s), are stabilized by intramolecular hydrogen bonding with the oxygen of a water ligand (N_L–$H_L\cdots O_{aq}$) (Figure 32a). The longer C–E bonds in $[Fe(OH_2)_5L]^{2+}$ (i.e., for $\mathbf{3_{Se}}$: d(C–Se) = 1.893 Å) vs the free ligand (d(C–Se) = 1.838 Å) are consistent with stabilization of the zwitterionic resonance form of the thione/selone through coordination to Fe(II).

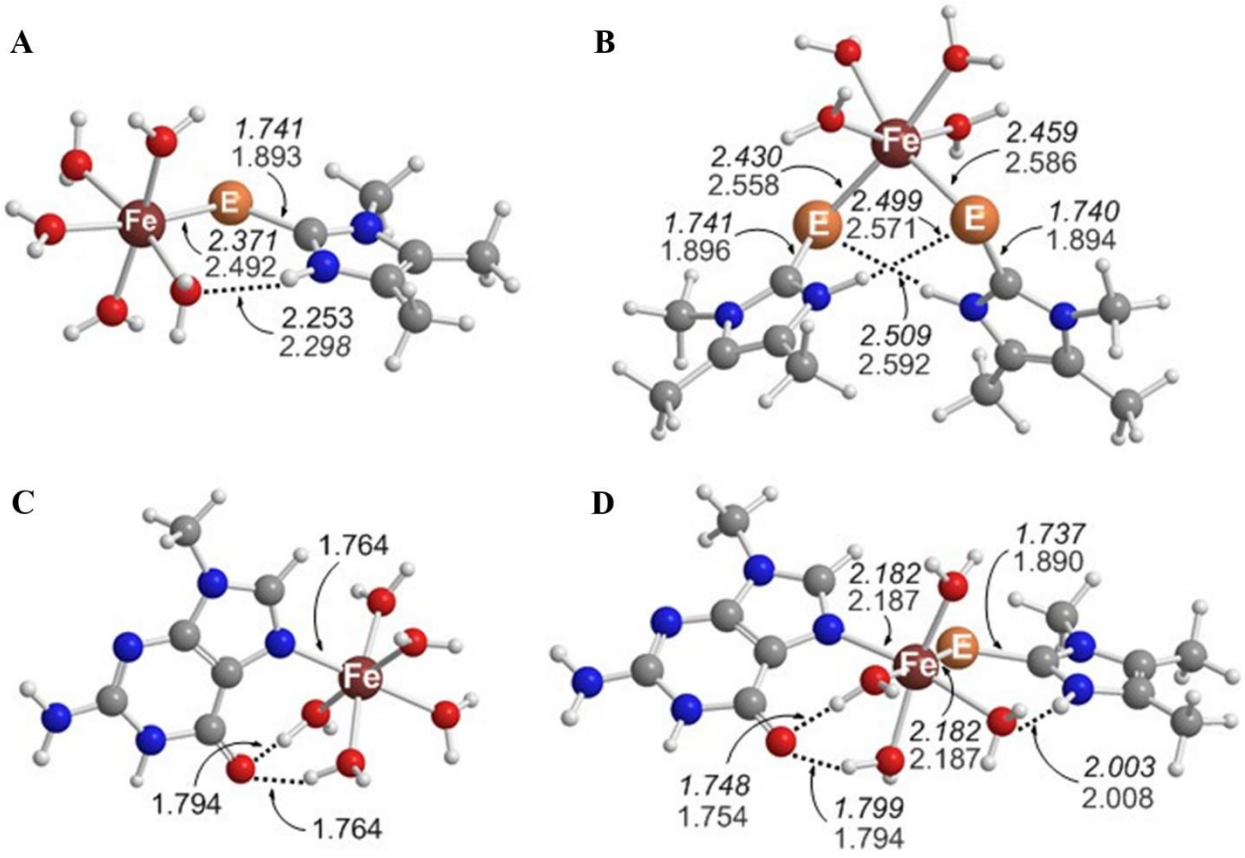

Figure 32. Representative intramolecular bonds lengths (Å) in (A) $[Fe(OH_2)_5L]^{2+}$, (B) $Fe(OH_2)_4L_2]^{2+}$, (C) $[Fe(OH_2)_5G]^{2+}$, and (D) $Fe(OH_2)_4GL]^{2+}$ complexes (L = **4S**/**4Se**; G = guanine).

Substitution of an aqua ligand by L (15) is more energetically favorable with increasing methylation and for selone derivatives relative to the thiones (Table 6), consistent with the trends in the zwitterionic properties of the free ligand. Intramolecular H–bonding (N_L–H···O_{aq}) stabilizes the complexes more than N-methylation (i.e., compare **1S**/**1Se** and **2S**/**2Se** in Table 6). Methylation at C-positions while preserving the N_L–H···O_{aq} bond offers a greater stability of ~3 kcal/mol per methyl group (i.e., **4S**/**4Se** versus **2S**/**2Se**, Table 6). Due to this combination of the effects of hydrogen bonding and methylation, the most stable $[Fe(OH_2)_5L]^{2+}$ complexes are those

of **4S**/**4Se** rather than **5S**/**5Se**, the most zwitterionic free ligands. **4S**/**4Se** have the shortest Fe–E bonds, while **3S**/**3Se** and **5S**/**5Se** have the longest due to the steric bulk of the ligand.

$$[Fe(OH_2)_5L]^{2+} + L \rightarrow [Fe(OH_2)_4L_2]^{2+} + H_2O \quad (16)$$

Table 6. **Relative energies of substitution of water ligands at the Fe(II) center by thione/ selone (L) and guanine (G) calculated from the reactions in Eqs. (15), (16), (18) and (19).**[a]

Ligand	ΔE + ZPE, kcal/mol			
	$[Fe(H_2O)_5L]^{2+}$ Eq. (15)	$[Fe(H_2O)_4L_2]^{2+}$ Eq. (16)	$[Fe(H_2O)_4GL]^{2+}$ Eq. (18)	Eq. (19)
thiones				
1S	-26.05	-26.24	-20.69	-46.70
2S	-27.14	-29.21	-22.25	-47.17
3S	-27.70	-22.85	-18.65	-43.01
4S	-33.70	-31.72	-26.37	-44.73
5S	-33.53	-25.95	-23.56	-42.08
Selones				
1Se	-27.38	-27.21	-21.95	-46.63
2Se	-27.85	-30.27	-23.45	-47.66
3Se	-29.33	-23.58	-21.24	-43.98
4Se	-34.75	-32.34	-27.51	-44.82
5Se	-34.51	-27.30	-25.79	-43.34

[a] Eq. (17): ΔE + ZPE = -52.06 kcal/mol

The IC_{50} values reported by Brumaghim[337] suggest that thiones and selones coordinate to Fe(II) in varying ratios. The optimized structures of bis-thione/selone $[Fe(OH_2)_4L_2]^{2+}$ complexes preserve the distorted octahedral geometry of the Fe(II) center. Complexes with L containing NH groups are stabilized by intramolecular hydrogen bonds between N–H of one L and the S/Se atom of the other (Figure 32b) instead of intramolecular hydrogen bonds to water ligands found in $[Fe(OH2)5L]^{2+}$. This interaction is the major factor that stabilizes the bis-thione Fe(II) complexes followed by degree of methylation, such that the order of complex stability (eq. 16) is: **3**$_S$/**3**$_{Se}$ < **5**$_S$/**5**$_{Se}$ ~ **1**$_S$/**1**$_{Se}$ < **2**$_S$/**2**$_{Se}$ < **4**$_S$/**4**$_{Se}$. Overall, the substitution of a second L is generally less energetically favorable than the first due to steric interactions between the ligands.

The replacement of an aqua ligand of $[Fe(OH_2)_6]^{2+}$ by guanine (G) (eq. 17) was modeled to mimic the proposed biological interaction of Fe(II) and DNA.[330,333,353,354] The substitution of G is more favorable than substitution by L in eq. (15) by -17 – -26 kcal/mol (Table 6), due to the preference of the borderline acid Fe(II) for the borderline nitrogenic base. The optimized $[Fe(OH_2)_5G]^{2+}$ complex has a distorted octahedral coordination and is stabilized by two internal hydrogen bonds between water ligands and the guanine carbonyl oxygen (Figure 32c). The energetic favorability of substitution of G over L (eq. 15 vs 17) could suggest that the mechanism by which thiones/selones protect against Fe(II)-mediated damage may occur after initial metal coordination to DNA. However, kinetics studies of the relative rates of substitution would be required to confirm these conclusions.

$$[Fe(OH_2)_6]^{2+} + G \rightarrow [Fe(OH_2)_5G]^{2+} + H_2O \quad (17)$$

$$[Fe(OH_2)_5G]^{2+} + L \rightarrow [Fe(OH_2)_4GL]^{2+} + H_2O \quad (18)$$

$$[Fe(OH_2)_5L]^{2+} + G \rightarrow [Fe(OH_2)_4GL]^{2+} + H_2O \quad (19)$$

The formation of the tetraaquairon(II) guanine thione/selone complex $[Fe(OH_2)_4GL]^{2+}$ was modeled along two possible pathways of initial G or L coordination. Coordination of L to $[Fe(OH_2)_5G]^{2+}$ (18) may be more biologically relevant, since sterics may prevent Fe(II)-thione/selone complexes from effectively approaching DNA (modeled by eq. 19). The ΔE+ZPE of ($[Fe(OH_2)_4GL]^{2+}$ complexes by these two pathways follows the trend in the $[Fe(OH_2)_4L_2]^{2+}$ series. In both di-substituted series, trends are reported for the cis complexes only, which are more stable than the trans (Table 6 and Figure 32d). The relative energy of substitution of G on $[Fe(OH_2)_5L]^{2+}$ is almost independent of the nature of L, but less favorable than initial coordination of G in $[Fe(OH_2)_5G]^{2+}$ due to steric interactions with L. Fe(II)-guanine thione/selone complexes are stabilized by two hydrogen bonds from water ligands to the guanine carbonyl oxygen and, if applicable, one hydrogen bond from water ligand to N-H of thione/selone. These results may explain the different outcomes of the experimental studies examining the ability of inorganic selenium compounds to prevent Fe(II)-mediated DNA damage.[355] The lesser protection by inorganic selenium compounds added after incubation of Fe(II) and DNA may be due to reduced accessibility of the selenium species to the DNA-bound Fe(II). In contrast, the addition of Fe(II) and selenium species prior to the addition of DNA was more successful in preventing DNA damage.

Thiones and selones are proposed to prevent oxidative DNA damage by coordinating to the metal and undergoing oxidation more easily than the metal center.[122,356] In this targeted ROS scavenging,[337] the thione/selone ligands sacrifice their electrons to prevent Fe(II) oxidation and DNA damage. Assuming that electrons will be lost from the HOMO in an oxidative process, we examined the character of the frontier orbitals of the Fe(II) complexes to understand how thiones/selones protect against DNA damage. The HOMO of $[Fe(OH_2)_6]^{2+}$ is the metal-centered

eg* orbital with antibonding character between the metal and water ligands (Figure 33). From these results, we can conclude that aquated (i.e., “free”) Fe(II) ions undergo oxidation at the metal center consistent with Fenton-type chemistry. In contrast, the HOMO of $[Fe(OH_2)_5G]^{2+}$ is localized on the nucleobase (Figure 33). Therefore, when Fe(II) coordinates to DNA through the N7 of guanine, damage may occur by direct oxidation of the metallated nucleobase. Likewise, the HOMOs of $[Fe(OH_2)_5L]^{2+}$ are similarly ligand-based and localized on an E-type lone pair of the thione/selone (Figure 33).

Therefore, in agreement with the previous modeling of Cu(I) complexes of thiones/selones,[122,337] the ligands would be preferentially oxidized to protect the iron center. $[Fe(OH_2)_4L_2]^{2+}$ complexes maintain the same HOMO character as the mono- complexes, being predominately composed of delocalized p orbitals of the two L ligands (Figure 33). So, bis-thione/selone Fe(II) complexes are similarly predicted to oxidize at L in preference to the Fe(II) center. In the model of the L-protected Fe(II)-guanine complex $[Fe(OH_2)_4GL]^{2+}$, the HOMO is also L based with similar to the $[Fe(OH_2)_5L]^{2+}$ complexes (Figure 33). As a result, protection of DNA from Fe(II)-mediated oxidative damage is consistent with a mechanism of secondary coordination of a thione/selone ligand which is preferentially and sacrificially oxidized over Fe(II) or the nucleobase. The hydroxyl radical scavenging capacity of ergothioneine,[342] a thione similar to the ligands in this study, may be due to a similar shift in HOMO character if metal coordination is involved in the prevention of ROS production. Given the smaller field splitting in tetrahedral coordination, the same trends in HOMO character are expected if Fe(II) species are four-coordinate rather than the six- as modeled.

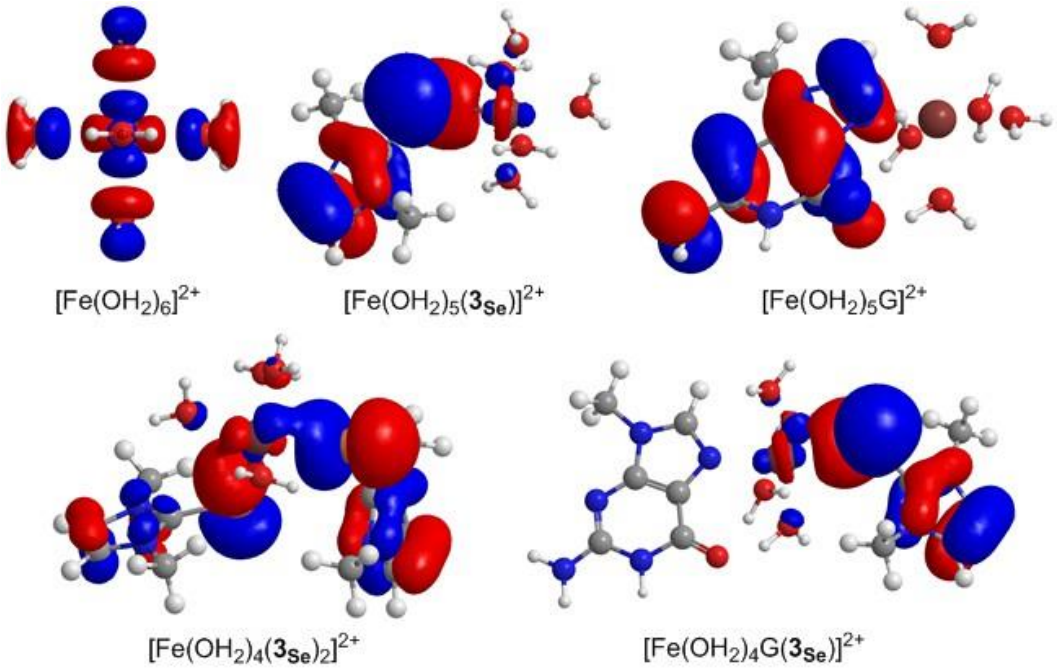

Figure 33. HOMOs of the representative Fe(II) complexes. $\mathbf{3_{Se}}$ was chosen as an example for all Fe(II)-L complexes, since the HOMOs of the thione complexes have the same character as the selones.

Conclusions

DFT calculations were performed for a series of thione/selone derivatives as free ligands and coordinated to aquated Fe(II) ions. The zwitterion character of the selone/thione ligands increased with substitution of electron-donating methyl groups, as shown in longer C–E bonds in the free ligand and more energetically favorable complexes with Fe(II). Selone derivatives have more zwitterionic character and coordinate more strongly to Fe(II), consistent with their greater effectiveness against Fe(II)-mediated DNA damage experimentally. Examination of the HOMO of the Fe(II) complexes indicates that Fe(II) binding to guanine makes the DNA more prone to

oxidative cleavage. However, the localization of the HOMO character of the Fe(II)-guanine complex changes upon thione/selone coordination from nucleobase- to thione/selone-centered. This shift in character is consistent with preferential oxidation at the thione/selone and protecting the metal and nucleobase. However, unlike other biochalcogen-based antioxidants, this protection is non-catalytic and DNA damage would be expected to resume once thiones/selones are exhausted unless the process could be coupled with a reductant. This modification explains the antioxidant activity of S/Se compounds in preventing Fe(II)-mediated redox DNA damage. Although our modeling has focused on six-coordinate complexes of Fe(II), the same trends are expected if the metal prefers tetrahedral coordination.

CHAPTER V

CONCLUSIONS

In this dissertation, computational methods were employed to address three different aspects of metal ions in biology. First, MD simulations were used to model the ability of Ni^{2+}-bound piscidins 1 and 3, naturally occurring antimicrobial peptides, to insert and induce structural changes to lipid bilayers in the presence and absence of oxidized lipid species. Upon metallation, P1:Ni^{2+} and P3:Ni^{2+} insert the N-termini deeper into the membrane and modify their orientations (τ and ρ) to enhance the hydrophobic and electrostatic interactions. The insertion of the ATCUN- Ni^{2+} complex is aided by the partial shielding of the metal center by His4 coordination or aromatic sidechains. The membrane reacts to the peptide insertion by slightly increasing the hydrophobic thickness and the packing order of the lipid chains. In the presence of 10% aldo-PC, the lipid bilayer thins, reduces the interactions between the PC and PG headgroups, and increases the disorder of acyl chains. These changes are indicative of potential disruption of membrane bulk properties. P1:Ni^{2+} increases its hydrogen bonding interactions with the PG headgroups in the presence of oxPLs, in agreement with experimental data. Since deeper insertion and a preferential association with anionic headgroups may promote disruption of the bacterial membrane, the results of this investigation help explain the enhanced activity *in vitro* of metallated peptides in the presence of aldo-PC.

Second, multi-microsecond MD simulations were employed to study the effects of cysteine oxidation on ZFs, an important class of proteins that participate in the regulation of several cellular processes, and the interactions of oxidized ZFs with nucleic acids. The central zinc finger sequence (ZF456) of TFIIIA interacting with 5S RNA was used as a model for this study. The individual ZF domains in the reduced ZF456 peptides remain rigid and the $\beta\beta\alpha$-fold

intact, being compatible with both 5S RNA and DNA binding. Upon oxidation, the free oxidized ZF456 peptides become considerably more dynamic and adopt conformations incapable of RNA recognition. The individual ZFs unfold to various degrees with the most ββα-fold unraveling in fingers that make base-specific interactions with RNA – ZF4 and ZF6. Such unfolded peptides lack the secondary structure to recognize nucleic acids. The ability of oxidized ZF456 peptides to recognize and bind RNA is diminished in RNA-bound oxidized ZF456 systems because of the loss of key hydrogen bonds and native contacts found in the reduced ZF456-RNA complex. The conformational flexibility of the oxidized ZF456 peptides accompanied by the loss of key protein – RNA interactions demonstrate the structural importance of Zn^{2+} to the ZF secondary structure and ZF recognition mechanisms.

Finally, DFT studies were performed to investigate the prevention of Fe^{2+}-mediated DNA damage by the coordination of imidazole-based thiones and selones. Substitution of electron-donating methyl groups in a series of thione/selone derivatives yields longer C–E bonds in the free ligand, hence more zwitterion character, and more energetically favorable complexes with Fe(II). Since the selone derivatives have elongated C–E bonds and such more zwitterionic character, they coordinate more strongly to Fe(II). Experimentally, the selones have greater effectiveness against Fe(II)-mediated DNA damage than the thione counterparts. Upon thione/selone coordination the HOMO character of the Fe(II)-guanine complex shifts from the nucleobase to thione/selone. This change in HOMO localization is consistent with preferential oxidation at the thione/selone protecting the metal and nucleobase. These results explain the antioxidant activity of S/Se compounds in preventing Fe(II)-mediated redox DNA damage.

In future work, extending these computational studies on other metallopeptides and/or membrane-active peptides that share similar features may help to design novel therapeutics for

antibiotic-resistant infections. MD simulations of metal-bound piscidins in alternative lipid mixtures commonly used as bacteria membrane mimics (e.g., 1:1 POPG/POPE) and in the presence of various amounts (e.g., 25% oxPLs) and products of lipid oxidation (e.g., carboxyl functionalized PLs) will provide additional characteristics of their mechanism of action including change in orientation, depth of insertion, preferred lipid constituent for interactions and potential structural modifications within the bilayer. Additionally, a higher protein to lipid ratio may aid the comparison between the computational and biochemical data for a better understanding of the piscidin mechanism of action. MD simulations of ZF proteins interacting with oxidants (e.g., reducible sulfur and selenium compounds) will provide mechanistic details to the ZF oxidation process for the efficient targeting of ZF proteins involved in the survival and progression of cancer cells or part of viral replication and transcription mechanisms. These investigations may provide experimentalists with additional means to explain the *in vitro/vivo* effects of metal-binding (e.g., enhanced antimicrobial activity) or removal (e.g., inhibition of viral replication) to facilitate the successful and efficient design of novel therapeutics.

REFERENCES

(1) Frausto da Silva, J. J. R.; Williams, R. J. P. *The Biological Chemistry of the Elements: The Inorganic Chemistry of Life*, 2nd ed.; Oxford University Press: New York, NY, 2001.

(2) Andreini, C.; Bertini, I.; Cavallaro, G.; Holliday, G. L.; Thornton, J. M. Metal Ions in Biological Catalysis: From Enzyme Databases to General Principles. *J. Biol. Inorg. Chem.* **2008**, *13*, 1205–1218.

(3) Sigel, H.; Sigel, A. The Bio-Relevant Metals of the Periodic Table of the Elements. *Z. Naturforsch. B* **2019**, *74*, 461–471.

(4) Bertini, I.; Sigel, A. *Handbook on Metalloproteins*; CRC Press: Boca Raton, 2014.

(5) Freisinger, E.; Sigel, R. K. O. The Bioinorganic Periodic Table. *Chimia* **2019**, *73*, 185–185.

(6) Sigel, A.; Sigel, H.; Sigel, R. K. O. *Interrelations between Essential Metal Ions and Human Diseases*; Metal Ions in Life Sciences; Springer Netherlands: Dordrecht, 2013; Vol. 13.

(7) Kaim, W.; Schwederski, B. *Bioinorganic Chemistry: Inorganic Elements in the Chemistry of Life*, 1st ed.; John Wiley & Sons: Chichester, U.K., 2004.

(8) Andrews, N. C. Forging a Field: The Golden Age of Iron Biology. *Blood* **2008**, *112*, 219–230.

(9) Waldron, K. J.; Rutherford, J. C.; Ford, D.; Robinson, N. J. Metalloproteins and Metal Sensing. *Nature* **2009**, *460*, 823–830.

(10) Emerit, J.; Beaumont, C.; Trivin, F. Iron Metabolism, Free Radicals, and Oxidative Injury. *Biomed. Pharmacother.* **2001**, *55*, 333–339.

(11) Enzymes/Proteins with Known Structure. In *Handbook on Metalloproteins*; Bertini, I., Sigel, A., Eds.; CRC Press: Boca Raton, 2001.

(12) Gohara, D. W.; Di Cera, E. Molecular Mechanisms of Enzyme Activation by Monovalent Cations. *J. Biol. Chem.* **2016**, *291*, 20840–20848.

(13) Di Cera, E. A Structural Perspective on Enzymes Activated by Monovalent Cations*. *J. Biol. Chem.* **2006**, *281*, 1305–1308.

(14) Boyer, P. D.; Lardy, H. A.; Phillips, P. H. The Role oF Potassium in Muscle Phosphorylations. *J. Biol. Chem.* **1942**, *146*, 673–682.

(15) Machius, M.; Chuang, J. L.; Wynn, R. M.; Tomchick, D. R.; Chuang, D. T. Structure of Rat BCKD Kinase: Nucleotide-Induced Domain Communication in a Mitochondrial Protein Kinase. *Proc. Natl. Acad. Sci. U.S.A.* **2001**, *98*, 11218–11223.

(16) Kato, M.; Chuang, J. L.; Tso, S.-C.; Wynn, R. M.; Chuang, D. T. Crystal Structure of Pyruvate Dehydrogenase Kinase 3 Bound to Lipoyl Domain 2 of Human Pyruvate Dehydrogenase Complex. *EMBO J.* **2005**, *24*, 1763–1774.

(17) Lainé-Cessac, P.; Allain, P. Kinetic Studies of the Effects of K+, Na+ and Li+ on the Catalytic Activity of Human Erythrocyte Pyridoxal Kinase. *Enzyme Protein* **1996**, *49*, 291–304.

(18) Villeret, V.; Huang, S.; Fromm, H. J.; Lipscomb, W. N. Crystallographic Evidence for the Action of Potassium, Thallium, and Lithium Ions on Fructose-1,6-Bisphosphatase. *Proc. Natl. Acad. Sci. U.S.A.* **1995**, *92*, 8916–8920.

(19) Mudd, S. H.; Cantoni, G. L. Activation of Methionine for Transmethylation. III. The Methionine-Activating Enzyme of Bakers' Yeast. *J. Biol. Chem.* **1958**, *231*, 481–492.
(20) Hall, D. R.; Leonard, G. A.; Reed, C. D.; Watt, C. I.; Berry, A.; Hunter, W. N. The Crystal Structure of Escherichia Coli Class II Fructose-1, 6-Bisphosphate Aldolase in Complex with Phosphoglycolohydroxamate Reveals Details of Mechanism and Specificity. *J. Mol. Biol.* **1999**, *287*, 383–394.
(21) Hall, D. R.; Bond, C. S.; Leonard, G. A.; Watt, C. I.; Berry, A.; Hunter, W. N. Structure of Tagatose-1,6-Bisphosphate Aldolase. Insight into Chiral Discrimination, Mechanism, and Specificity of Class II Aldolases. *J. Biol. Chem.* **2002**, *277*, 22018–22024.
(22) Andersson, C. E.; Mowbray, S. L. Activation of Ribokinase by Monovalent Cations11Edited by R. Huber. *J. Mol. Biol.* **2002**, *315*, 409–419.
(23) Hohenester, E.; Keller, J. W.; Jansonius, J. N. An Alkali Metal Ion Size-Dependent Switch in the Active Site Structure of Dialkylglycine Decarboxylase. *Biochemistry* **1994**, *33*, 13561–13570.
(24) Yamada, T.; Komoto, J.; Takata, Y.; Ogawa, H.; Pitot, H. C.; Takusagawa, F. Crystal Structure of Serine Dehydratase from Rat Liver. *Biochemistry* **2003**, *42*, 12854–12865.
(25) Sundararaju, B.; Antson, A. A.; Phillips, R. S.; Demidkina, T. V.; Barbolina, M. V.; Gollnick, P.; Dodson, G. G.; Wilson, K. S. The Crystal Structure of Citrobacter Freundii Tyrosine Phenol-Lyase Complexed with 3-(4'-Hydroxyphenyl)Propionic Acid, Together with Site-Directed Mutagenesis and Kinetic Analysis, Demonstrates That Arginine 381 Is Required for Substrate Specificity. *Biochemistry* **1997**, *36*, 6502–6510.
(26) Isupov, M. N.; Antson, A. A.; Dodson, E. J.; Dodson, G. G.; Dementieva, I. S.; Zakomirdina, L. N.; Wilson, K. S.; Dauter, Z.; Lebedev, A. A.; Harutyunyan, E. H. Crystal Structure of Tryptophanase. *J. Mol. Biol.* **1998**, *276*, 603–623.
(27) Peracchi, A.; Mozzarelli, A.; Rossi, G. L. Monovalent Cations Affect Dynamic and Functional Properties of the Tryptophan Synthase Alpha 2 Beta 2 Complex. *Biochemistry* **1995**, *34*, 9459–9465.
(28) Dang, Q. D.; Di Cera, E. Residue 225 Determines the Na(+)-Induced Allosteric Regulation of Catalytic Activity in Serine Proteases. *Proc. Natl. Acad. Sci. U.S.A.* **1996**, *93*, 10653–10656.
(29) AEvarsson, A.; Chuang, J. L.; Wynn, R. M.; Turley, S.; Chuang, D. T.; Hol, W. G. Crystal Structure of Human Branched-Chain Alpha-Ketoacid Dehydrogenase and the Molecular Basis of Multienzyme Complex Deficiency in Maple Syrup Urine Disease. *Structure* **2000**, *8*, 277–291.
(30) Jorgensen, P. L.; Hakansson, K. O.; Karlish, S. J. D. Structure and Mechanism of Na,K-ATPase: Functional Sites and Their Interactions. *Annu. Rev. Physiol.* **2003**, *65*, 817–849.
(31) Irving, H.; Williams, R. J. P. Order of Stability of Metal Complexes. *Nature* **1948**, *162*, 746–747.
(32) Romani, A. M. P. Cellular Magnesium Homeostasis. *Arch. Biochem. Biophys.* **2011**, *512*, 1–23.
(33) Yamanaka, R.; Shindo, Y.; Oka, K. Magnesium Is a Key Player in Neuronal Maturation and Neuropathology. *Int. J. Mol. Sci.* **2019**, *20*, 3439.
(34) Vashishtha, A. K.; Wang, J.; Konigsberg, W. H. Different Divalent Cations Alter the Kinetics and Fidelity of DNA Polymerases. *J. Biol. Chem.* **2016**, *291*, 20869–20875.
(35) Brini, M.; Calì, T.; Ottolini, D.; Carafoli, E. Neuronal Calcium Signaling: Function and Dysfunction. *Cell. Mol. Life Sci.* **2014**, *71*, 2787–2814.

(36) Carafoli, E.; Krebs, J. Why Calcium? How Calcium Became the Best Communicator. *J. Biol. Chem.* **2016**, *291*, 20849–20857.
(37) Burgoyne, R. D. Neuronal Calcium Sensor Proteins: Generating Diversity in Neuronal Ca2+ Signalling. *Nat. Rev. Neurosci.* **2007**, *8*, 182–193.
(38) Christianson, D. W.; Cox, J. D. Catalysis By Metal-Activated Hydroxide in Zinc and Manganese Metalloenzymes. *Annu. Rev. Biochem.* **1999**, *68*, 33–57.
(39) Hider, R. C.; Kong, X. Iron: Effect of Overload and Deficiency. In *Interrelations between Essential Metal Ions and Human Diseases*; Sigel, A., Sigel, H., Sigel, R. K. O., Eds.; Metal Ions in Life Sciences; Springer Netherlands: Dordrecht, 2013; pp 229–294.
(40) Guengerich, F. P. Introduction to Metals in Biology 2017: Iron Transport, Storage, and the Ramifications. *J. Biol. Chem.* **2017**, *292*, 12725–12726.
(41) Fernandes, M. A.; Hanck-Silva, G.; Baveloni, F. G.; Oshiro Junior, J. A.; de Lima, F. T.; Eloy, J. O.; Chorilli, M. A Review of Properties, Delivery Systems and Analytical Methods for the Characterization of Monomeric Glycoprotein Transferrin. *Crit. Rev. Anal. Chem.* **2021**, *51*, 399–410.
(42) Zhang, C.; Zhang, X.; Zhao, G. Ferritin Nanocage: A Versatile Nanocarrier Utilized in the Field of Food, Nutrition, and Medicine. *Nanomaterials* **2020**, *10*, 1894.
(43) Li, S.; Yang, Y.; Li, W. Human Ferroportin Mediates Proton-Coupled Active Transport of Iron. *Blood Adv.* **2020**, *4*, 4758–4768.
(44) Olson, J. S. Lessons Learned from 50 Years of Hemoglobin Research: Unstirred and Cell-Free Layers, Electrostatics, Baseball Gloves, and Molten Globules. *Antioxid. Redox Signal.* **2020**, *32*, 228–246.
(45) Kaila, V. R. I.; Verkhovsky, M. I.; Wikström, M. Proton-Coupled Electron Transfer in Cytochrome Oxidase. *Chem. Rev.* **2010**, *110*, 7062–7081.
(46) Zeida, A.; Trujillo, M.; Ferrer-Sueta, G.; Denicola, A.; Estrin, D. A.; Radi, R. Catalysis of Peroxide Reduction by Fast Reacting Protein Thiols. *Chem. Rev.* **2019**, *119*, 10829–10855.
(47) Nandi, A.; Yan, L.-J.; Jana, C. K.; Das, N. Role of Catalase in Oxidative Stress- and Age-Associated Degenerative Diseases. *Oxid. Med. Cell. Longev.* **2019**, *2019*, e9613090.
(48) Johnson, D. C.; Dean, D. R.; Smith, A. D.; Johnson, M. K. Structure, Function, and Formation of Biological Iron-Sulfur Clusters. *Annu. Rev. Biochem.* **2005**, *74*, 247–281.
(49) Kräutler, B. In My Element: Cobalt. *Chem. Eur. J.* **2019**, *25*, 4870–4870.
(50) Yamada, K. Cobalt: Its Role in Health and Disease. In *Interrelations between Essential Metal Ions and Human Diseases*; Sigel, A., Sigel, H., Sigel, R. K. O., Eds.; Metal Ions in Life Sciences; Springer Netherlands: Dordrecht, 2013; pp 295–320.
(51) Matthews, R. G. Cobalamin- and Corrinoid-Dependent Enzymes. *Met. Ions Life Sci.* **2009**, *6*, 53–114.
(52) Scheiber, I.; Dringen, R.; Mercer, J. F. B. Copper: Effects of Deficiency and Overload. *Met. Ions Life Sci.* **2013**, *13*, 359–387.
(53) Maret, W. Zinc and the Zinc Proteome. *Met. Ions Life Sci.* **2013**, *12*, 479–501.
(54) Fukai, T.; Ushio-Fukai, M.; Kaplan, J. H. Copper Transporters and Copper Chaperones: Roles in Cardiovascular Physiology and Disease. *Am. J. Physiol. Cell Physiol.* **2018**, *315*, C186–C201.
(55) Prigge, S. T.; Mains, R. E.; Eipper, B. A.; Amzel, L. M. New Insights into Copper Monooxygenases and Peptide Amidation: Structure, Mechanism and Function. *Cell. Mol. Life Sci.* **2000**, *57*, 1236–1259.

(56) Finney, J.; Moon, H.-J.; Ronnebaum, T.; Lantz, M.; Mure, M. Human Copper-Dependent Amine Oxidases. *Arch. Biochem. Biophys.* **2014**, *546*, 19–32.
(57) Erxleben, A. Mechanistic Studies of Homo- and Heterodinuclear Zinc Phosphoesterase Mimics: What Has Been Learned? *Front. Chem.* **2019**, *7*, 82.
(58) Mendel, R. R. The Molybdenum Cofactor. *J. Biol. Chem.* **2013**, *288*, 13165–13172.
(59) Schwarz, G.; Mendel, R. R.; Ribbe, M. W. Molybdenum Cofactors, Enzymes and Pathways. *Nature* **2009**, *460*, 839–847.
(60) Mendel, R. R.; Bittner, F. Cell Biology of Molybdenum. *Biochim. Biophys. Acta Mol. Cell Res.* **2006**, *1763*, 621–635.
(61) Battelli, M. G.; Polito, L.; Bortolotti, M.; Bolognesi, A. Xanthine Oxidoreductase in Drug Metabolism: Beyond a Role as a Detoxifying Enzyme. *Curr. Med. Chem.* **2016**, *23*, 4027–4036.
(62) Mendel, R. R. Metabolism of Molybdenum. *Met. Ions Life Sci.* **2013**, *12*, 503–528.
(63) Rehder, D. Vanadium. Its Role for Humans. *Met. Ions Life Sci.* **2013**, *13*, 139–169.
(64) Winter, J. M.; Moore, B. S. Exploring the Chemistry and Biology of Vanadium-Dependent Haloperoxidases. *J. Biol. Chem.* **2009**, *284*, 18577–18581.
(65) Ragsdale, S. W. Nickel-Based Enzyme Systems. *J. Biol. Chem.* **2009**, *284*, 18571–18575.
(66) Xu, Y.; Morel, F. M. M. Cadmium in Marine Phytoplankton. In *Cadmium: From Toxicity to Essentiality*; Sigel, A., Sigel, H., Sigel, R. K., Eds.; Metal Ions in Life Sciences; Springer Netherlands: Dordrecht, 2013; pp 509–528.
(67) Trachootham, D.; Lu, W.; Ogasawara, M. A.; Valle, N. R.-D.; Huang, P. Redox Regulation of Cell Survival. *Antioxid. Redox Signal.* **2008**, *10*, 1343–1374.
(68) Hodgkinson, V.; Petris, M. J. Copper Homeostasis at the Host-Pathogen Interface. *J. Biol. Chem.* **2012**, *287*, 13549–13555.
(69) La Fontaine, S.; Mercer, J. F. B. Trafficking of the Copper-ATPases, ATP7A and ATP7B: Role in Copper Homeostasis. *Arch. Biochem. Biophys.* **2007**, *463*, 149–167.
(70) Li, Y.; Jiao, Q.; Xu, H.; Du, X.; Shi, L.; Jia, F.; Jiang, H. Biometal Dyshomeostasis and Toxic Metal Accumulations in the Development of Alzheimer's Disease. *Front. Mol. Neurosci.* **2017**, *10*.
(71) Turski, M. L.; Thiele, D. J. New Roles for Copper Metabolism in Cell Proliferation, Signaling, and Disease. *J. Biol. Chem.* **2009**, *284*, 717–721.
(72) Kambe, T.; Andrews, G. K. Novel Proteolytic Processing of the Ectodomain of the Zinc Transporter ZIP4 (SLC39A4) during Zinc Deficiency Is Inhibited by Acrodermatitis Enteropathica Mutations. *Mol. Cell. Biol.* **2009**, *29*, 129–139.
(73) Harford, C.; Sarkar, B. Amino Terminal Cu(II)- and Ni(II)-Binding (ATCUN) Motif of Proteins and Peptides: Metal Binding, DNA Cleavage, and Other Properties. *Acc. Chem. Res.* **1997**, *30*, 123–130.
(74) Joyner, J. C.; Reichfield, J.; Cowan, J. A. Factors Influencing the DNA Nuclease Activity of Iron, Cobalt, Nickel, and Copper Chelates. *J. Am. Chem. Soc.* **2011**, *133*, 15613–15626.
(75) Joyner, J. C.; Cowan, J. A. Target-Directed Catalytic Metallodrugs. *Braz. J. Med. Biol. Res.* **2013**, *46*, 465–485.
(76) Neupane, K. P.; Aldous, A. R.; Kritzer, J. A. Metal-Binding and Redox Properties of Substituted Linear and Cyclic ATCUN Motifs. *J. Inorg. Biochem.* **2014**, *139*, 65–76.

(77) Libardo, M. D.; Cervantes, J. L.; Salazar, J. C.; Angeles-Boza, A. M. Improved Bioactivity of Antimicrobial Peptides by Addition of Amino-Terminal Copper and Nickel (ATCUN) Binding Motifs. *ChemMedChem* **2014**, *9*, 1892–1901.
(78) Melino, S.; Santone, C.; Nardo, P. D.; Sarkar, B. Histatins: Salivary Peptides with Copper(II)- and Zinc(II)-Binding Motifs. *FEBS J.* **2014**, *281*, 657–672.
(79) Wende, C.; Kulak, N. Fluorophore ATCUN Complexes: Combining Agent and Probe for Oxidative DNA Cleavage. *Chem. Commun.* **2015**, *51*, 12395–12398.
(80) Kimoto, E.; Tanaka, H.; Gyotoku, J.; Morishige, F.; Pauling, L. Enhancement of Antitumor Activity of Ascorbate against Ehrlich Ascites Tumor Cells by the Copper:Glycylglycylhistidine Complex. *Cancer Res.* **1983**, *43*, 824–828.
(81) Gokhale, N. H.; Bradford, S.; Cowan, J. A. Catalytic Inactivation of Human Carbonic Anhydrase I by a Metallopeptide−Sulfonamide Conjugate Is Mediated by Oxidation of Active Site Residues. *J. Am. Chem. Soc.* **2008**, *130*, 2388–2389.
(82) Deng, D.; Liu, L.; Bu, Y.; Liu, X.; Wang, X.; Zhang, B. Electrochemical Sensing Devices Using ATCUN-Cu(II) Complexes as Electrocatalysts for Water Oxidation. *Sens. and Actuators B Chem.* **2018**, *269*, 189–194.
(83) Kandemir, B.; Kubie, L.; Guo, Y.; Sheldon, B.; Bren, K. L. Hydrogen Evolution from Water under Aerobic Conditions Catalyzed by a Cobalt ATCUN Metallopeptide. *Inorg. Chem.* **2016**, *55*, 1355–1357.
(84) Guo, Y.; Stroka, J. R.; Kandemir, B.; Dickerson, C. E.; Bren, K. L. Cobalt Metallopeptide Electrocatalyst for the Selective Reduction of Nitrite to Ammonium. *J. Am. Chem. Soc.* **2018**, *140*, 16888–16892.
(85) Maiti, B. K.; Govil, N.; Kundu, T.; Moura, J. J. G. Designed Metal-ATCUN Derivatives: Redox- and Non-Redox-Based Applications Relevant for Chemistry, Biology, and Medicine. *iScience* **2020**, *23*, 101792.
(86) Alexander, J. L.; Thompson, Z.; Cowan, J. A. Antimicrobial Metallopeptides. *ACS Chem. Biol.* **2018**, *13*, 844–853.
(87) Libardo, M. D. J.; Paul, T. J.; Prabhakar, R.; Angeles-Boza, A. M. Hybrid Peptide ATCUN-Sh-Buforin: Influence of the ATCUN Charge and Stereochemistry on Antimicrobial Activity. *Biochimie* **2015**, *113*, 143–155.
(88) Libardo, M. D. J.; Nagella, S.; Lugo, A.; Pierce, S.; Angeles-Boza, A. M. Copper-Binding Tripeptide Motif Increases Potency of the Antimicrobial Peptide Anoplin via Reactive Oxygen Species Generation. *Biochem. Biophys. Res. Commun.* **2015**, *456*, 446–451.
(89) Joyner, J. C.; Hodnick, W. F.; Cowan, A. S.; Tamuly, D.; Boyd, R.; Cowan, J. A. Antimicrobial Metallopeptides with Broad Nuclease and Ribonuclease Activity. *Chem. Commun.* **2013**, *49*, 2118–2120.
(90) Andreini, C.; Banci, L.; Bertini, I.; Rosato, A. Counting the Zinc-Proteins Encoded in the Human Genome. *J. Proteome Res.* **2006**, *5*, 196–201.
(91) Miller, J.; McLachlan, A. D.; Klug, A. Repetitive Zinc-Binding Domains in the Protein Transcription Factor IIIA from Xenopus Oocytes. *EMBO J.* **1985**, *4*, 1609–1614.
(92) Klug, A. The Discovery of Zinc Fingers and Their Development for Practical Applications in Gene Regulation and Genome Manipulation. *Q. Rev. Biophys.* **2010**, *43*, 1–21.
(93) Krishna, S. S.; Majumdar, I.; Grishin, N. V. Structural Classification of Zinc Fingers: Survey and Summary. *Nucleic Acids Res.* **2003**, *31*, 532–550.

(94) Maret, W. Zinc Coordination Environments in Proteins as Redox Sensors and Signal Transducers. *Antioxid. Redox Signal.* **2006**, *8*, 1419–1441.
(95) Kluska, K.; Adamczyk, J.; Krężel, A. Metal Binding Properties, Stability and Reactivity of Zinc Fingers. *Coord. Chem. Rev.* **2018**, *367*, 18–64.
(96) Larabee, J. L.; Hocker, J. R.; Hanas, J. S. Mechanisms of Inhibition of Zinc-Finger Transcription Factors by Selenium Compounds Ebselen and Selenite. *J. Inorg. Biochem.* **2009**, *103*, 419–426.
(97) Larabee, J. L.; Hocker, J. R.; Hanas, R. J.; Kahn, F. M.; Hanas, J. S. Inhibition of Zinc Finger Protein–DNA Interactions by Sodium Selenite. *Biochem. Pharmacol.* **2002**, *64*, 1757–1765.
(98) Sargsyan, K.; Lin, C.-C.; Chen, T.; Grauffel, C.; Chen, Y.-P.; Yang, W.-Z.; Yuan, H. S.; Lim, C. Multi-Targeting of Functional Cysteines in Multiple Conserved SARS-CoV-2 Domains by Clinically Safe Zn-Ejectors. *Chem. Sci.* **2020**, *11*, 9904–9909.
(99) Chen, T.; Fei, C.-Y.; Chen, Y.-P.; Sargsyan, K.; Chang, C.-P.; Yuan, H. S.; Lim, C. Synergistic Inhibition of SARS-CoV-2 Replication Using Disulfiram/Ebselen and Remdesivir. *ACS Pharmacol. Transl. Sci.* **2021**, *4*, 898–907.
(100) Lutz, P. B.; Bayse, C. A. Chalcogen Bonding Interactions between Reducible Sulfur and Selenium Compounds and Models of Zinc Finger Proteins. *J. Inorg. Biochem.* **2016**, *157*, 94–103.
(101) A. Bayse, C.; M. Whitty, S.; Antony, S. Oxidation of Zinc-Sulfur Centers by Reducible Organoselenium Compounds: A Review and Bonding Perspective. *Curr. Chem. Biol.* **2013**, *7*, 57–64.
(102) Antony, S.; Bayse, C. A. Density Functional Theory Study of the Attack of Ebselen on a Zinc-Finger Model. *Inorg. Chem.* **2013**, *52*, 13803–13805.
(103) Schieber, M.; Chandel, N. S. ROS Function in Redox Signaling and Oxidative Stress. *Curr. Biol.* **2014**, *24*, R453–R462.
(104) Prousek, J. Fenton Chemistry in Biology and Medicine. *Pure Appl. Chem.* **2009**, *79*, 2325–2338.
(105) Kasprzak, K. S. Oxidative DNA and Protein Damage in Metal-Induced Toxicity and Carcinogenesis. *Free Radic. Biol. Med.* **2002**, *32*, 958–967.
(106) Angel, I.; Bar, A.; Horovitz, T.; Taler, G.; Krakovsky, M.; Resnitsky, D.; Rosenberg, G.; Striem, S.; Friedman, J. E.; Kozak, A. Metal Ion Chelation in Neurodegenerative Disorders. *Drug Dev. Res.* **2002**, *56*, 300–309.
(107) Battin, E. E.; Brumaghim, J. L. Antioxidant Activity of Sulfur and Selenium: A Review of Reactive Oxygen Species Scavenging, Glutathione Peroxidase, and Metal-Binding Antioxidant Mechanisms. *Cell Biochem. Biophys.* **2009**, *55*, 1–23.
(108) Nielsen, P.; Fischer, R.; Buggisch, P.; Janka-Schaub, G. Effective Treatment of Hereditary Haemochromatosis with Desferrioxamine in Selected Cases. *Br. J. Haematol.* **2003**, *123*, 952–953.
(109) Hoffbrand, A. V.; Cohen, A.; Hershko, C. Role of Deferiprone in Chelation Therapy for Transfusional Iron Overload. *Blood* **2003**, *102*, 17–24.
(110) Zheng, Y.; Li, X.-K.; Wang, Y.; Cai, L. The Role of Zinc, Copper and Iron in the Pathogenesis of Diabetes and Diabetic Complications: Therapeutic Effects by Chelators. *Hemoglobin* **2008**, *32*, 135–145.
(111) Ramchandani, D.; Berisa, M.; Tavarez, D. A.; Li, Z.; Miele, M.; Bai, Y.; Lee, S. B.; Ban, Y.; Dephoure, N.; Hendrickson, R. C.; Cloonan, S. M.; Gao, D.; Cross, J. R.; Vahdat, L.

T.; Mittal, V. Copper Depletion Modulates Mitochondrial Oxidative Phosphorylation to Impair Triple Negative Breast Cancer Metastasis. *Nat. Commun.* **2021**, *12*, 7311.

(112) Hauck, A. K.; Bernlohr, D. A. Oxidative Stress and Lipotoxicity. *J. Lipid Res.* **2016**, *57*, 1976–1986.

(113) Moravec, A. R.; Siv, A. W.; Hobby, C. R.; Lindsay, E. N.; Norbash, L. V.; Shults, D. J.; Symes, S. J. K.; Giles, D. K. Exogenous Polyunsaturated Fatty Acids Impact Membrane Remodeling and Affect Virulence Phenotypes among Pathogenic Vibrio Species. *Appl. Environ. Microbiol.* **2017**, *83*, e01415-17.

(114) Baker, L. Y.; Hobby, C. R.; Siv, A. W.; Bible, W. C.; Glennon, M. S.; Anderson, D. M.; Symes, S. J.; Giles, D. K. Pseudomonas Aeruginosa Responds to Exogenous Polyunsaturated Fatty Acids (PUFAs) by Modifying Phospholipid Composition, Membrane Permeability, and Phenotypes Associated with Virulence. *BMC Microbiol.* **2018**, *18*, 117.

(115) Rahman, Z.; Bazaz, Mohd. R.; Devabattula, G.; Khan, Mohd. A.; Godugu, C. Targeting H3K9 Methyltransferase G9a and Its Related Molecule GLP as a Potential Therapeutic Strategy for Cancer. *J. Biochem. Mol. Toxicol.* **2021**, *35*, e22674.

(116) Cook, K. M.; Hilton, S. T.; Mecinović, J.; Motherwell, W. B.; Figg, W. D.; Schofield, C. J. Epidithiodiketopiperazines Block the Interaction between Hypoxia-Inducible Factor-1α (HIF-1α) and P300 by a Zinc Ejection Mechanism. *J. Biol. Chem.* **2009**, *284*, 26831–26838.

(117) Jayatunga, M. K. P.; Thompson, S.; McKee, T. C.; Chan, M. C.; Reece, K. M.; Hardy, A. P.; Sekirnik, R.; Seden, P. T.; Cook, K. M.; McMahon, J. B.; Figg, W. D.; Schofield, C. J.; Hamilton, A. D. Inhibition of the HIF1α-P300 Interaction by Quinone- and Indandione-Mediated Ejection of Structural Zn(II). *Eur. J. Med. Chem.* **2015**, *94*, 509–516.

(118) Battin, E. E.; Brumaghim, J. L. Metal Specificity in DNA Damage Prevention by Sulfur Antioxidants. *J. Inorg. Biochem.* **2008**, *102*, 2036–2042.

(119) Battin, E. E.; Perron, N. R.; Brumaghim, J. L. The Central Role of Metal Coordination in Selenium Antioxidant Activity. *Inorg. Chem.* **2006**, *45*, 499–501.

(120) E. Battin, E.; T. Zimmerman, M.; R. Ramoutar, R.; E. Quarles, C.; L. Brumaghim, J. Preventing Metal-Mediated Oxidative DNA Damage with Selenium Compounds. *Metallomics* **2011**, *3*, 503–512.

(121) Ramoutar, R. R.; Brumaghim, J. L. Effects of Inorganic Selenium Compounds on Oxidative DNA Damage. *J. Inorg. Biochem.* **2007**, *101*, 1028–1035.

(122) Kimani, M. M.; Bayse, C. A.; Stadelman, B. S.; Brumaghim, J. L. Oxidation of Biologically Relevant Chalcogenones and Their Cu(I) Complexes: Insight into Selenium and Sulfur Antioxidant Activity. *Inorg. Chem.* **2013**, *52*, 11685–11687.

(123) S. Stadelman, B.; M. Kimani, M.; A. Bayse, C.; D. McMillen, C.; L. Brumaghim, J. Synthesis, Characterization, DFT Calculations, and Electrochemical Comparison of Novel Iron(Ii) Complexes with Thione and Selone Ligands. *Dalton Trans.* **2016**, *45*, 4697–4711.

(124) Stadelman, B. S.; Brumaghim, J. L. Thione- and Selone-Containing Compounds, Their Late First Row Transition Metal Coordination Chemistry, and Their Biological Potential. In *Biochalcogen Chemistry: The Biological Chemistry of Sulfur, Selenium, and Tellurium*; Bayse, Craig A., Brumaghim, Julia L., Eds.; ACS Symposium Series; American Chemical Society: Washington D.C., 2013; pp 33–70.

(125) Orian, L.; Toppo, S. Organochalcogen Peroxidase Mimetics as Potential Drugs: A Long Story of a Promise Still Unfulfilled. *Free Radic. Biol. Med.* **2014**, *66*, 65–74.
(126) Prabhu, P.; Singh, B. G.; Noguchi, M.; Phadnis, P. P.; Jain, V. K.; Iwaoka, M.; Priyadarsini, K. I. Stable Selones in Glutathione-Peroxidase-like Catalytic Cycle of Selenonicotinamide Derivative. *Org. Biomol. Chem.* **2014**, *12*, 2404–2412.
(127) Vanommeslaeghe, K.; Guvench, O.; MacKerell, A. D. Molecular Mechanics. *Curr. Pharm. Des.* **2014**, *20*, 3281–3292.
(128) Durrant, J. D.; McCammon, J. A. Molecular Dynamics Simulations and Drug Discovery. *BMC Biol.* **2011**, *9*, 71.
(129) Jones, J. E.; Chapman, S. On the Determination of Molecular Fields. —II. From the Equation of State of a Gas. *Proc. R. Soc. Lond. A Math Phys. Sci.* **1924**, *106*, 463–477.
(130) Allinger, N. L.; Zhou, X.; Bergsma, J. Molecular Mechanics Parameters. *J. Mol. Struc. THEOCHEM* **1994**, *312*, 69–83.
(131) Halgren, T. A. MMFF VII. Characterization of MMFF94, MMFF94s, and Other Widely Available Force Fields for Conformational Energies and for Intermolecular-Interaction Energies and Geometries. *J. Comput. Chem.* **1999**, *20*, 730–748.
(132) Jorgensen, W. L.; Tirado-Rives, J. The OPLS [Optimized Potentials for Liquid Simulations] Potential Functions for Proteins, Energy Minimizations for Crystals of Cyclic Peptides and Crambin. *J. Am. Chem. Soc.* **1988**, *110*, 1657–1666.
(133) Weiner, S. J.; Kollman, P. A.; Nguyen, D. T.; Case, D. A. An all atom force field for simulations of proteins and nucleic acids. *J. Comput. Chem.* **1986**, *7*, 230–252.
(134) Brooks, B. R.; Bruccoleri, R. E.; Olafson, B. D.; States, D. J.; Swaminathan, S.; Karplus, M. CHARMM: A Program for Macromolecular Energy, Minimization, and Dynamics Calculations. *J. Comput. Chem.* **1983**, *4*, 187–217.
(135) Wang, J.; Wolf, R. M.; Caldwell, J. W.; Kollman, P. A.; Case, D. A. Development and Testing of a General Amber Force Field. *J. Comput. Chem.* **2004**, *25*, 1157–1174.
(136) Maier, J. A.; Martinez, C.; Kasavajhala, K.; Wickstrom, L.; Hauser, K. E.; Simmerling, C. Ff14SB: Improving the Accuracy of Protein Side Chain and Backbone Parameters from Ff99SB. *J. Chem. Theory Comput.* **2015**, *11*, 3696–3713.
(137) Zgarbová, M.; Otyepka, M.; Šponer, J.; Mládek, A.; Banáš, P.; Cheatham, T. E.; Jurečka, P. Refinement of the Cornell et al. Nucleic Acids Force Field Based on Reference Quantum Chemical Calculations of Glycosidic Torsion Profiles. *J. Chem. Theory Comput.* **2011**, *7*, 2886–2902.
(138) Gould, I.; Skjevik, A.; Dickson, C.; Madej, B.; Walker, R. Lipid17: A Comprehensive AMBER Force Field for the Simulation of Zwitterionic and Anionic Lipids. *Manuscript in preparation* **2018**.
(139) Li, P.; Merz, K. M. MCPB.Py: A Python Based Metal Center Parameter Builder. *J. Chem. Inf. Model.* **2016**, *56*, 599–604.
(140) Li, P.; Merz, K. M. Metal Ion Modeling Using Classical Mechanics. *Chem. Rev.* **2017**, *117*, 1564–1686.
(141) Hancock, R. D. Molecular Mechanics Calculations and Metal Ion Recognition. *Acc. Chem. Res.* **1990**, *23*, 253–257.
(142) Stote, R. H.; Karplus, M. Zinc Binding in Proteins and Solution: A Simple but Accurate Nonbonded Representation. *Proteins* **1995**, *23*, 12–31.
(143) Åqvist, J.; Warshel, A. Computer Simulation of the Initial Proton Transfer Step in Human Carbonic Anhydrase I. *J. Mol. Biol.* **1992**, *224*, 7–14.

(144) Pang, Y. P. Successful Molecular Dynamics Simulation of Two Zinc Complexes Bridged by a Hydroxide in Phosphotriesterase Using the Cationic Dummy Atom Method. *Proteins* **2001**, *45*, 183–189.
(145) Norrby, P.; Liljefors, T. Automated Molecular Mechanics Parameterization with Simultaneous Utilization of Experimental and Quantum Mechanical Data. *J. Comput. Chem.* **1998**, *19*, 1146–1166.
(146) Norrby, P.-O.; Brandt, P. Deriving Force Field Parameters for Coordination Complexes. *Coord. Chem. Rev.* **2001**, *212*, 79–109.
(147) Peters, M. B.; Yang, Y.; Wang, B.; Füsti-Molnár, L.; Weaver, M. N.; Merz, K. M. Structural Survey of Zinc-Containing Proteins and Development of the Zinc AMBER Force Field (ZAFF). *J. Chem. Theory Comput.* **2010**, *6*, 2935–2947.
(148) Ishiyama, S.; Nishiyama, A.; Saeki, Y.; Moritsugu, K.; Morimoto, D.; Yamaguchi, L.; Arai, N.; Matsumura, R.; Kawakami, T.; Mishima, Y.; Hojo, H.; Shimamura, S.; Ishikawa, F.; Tajima, S.; Tanaka, K.; Ariyoshi, M.; Shirakawa, M.; Ikeguchi, M.; Kidera, A.; Suetake, I.; Arita, K.; Nakanishi, M. Structure of the Dnmt1 Reader Module Complexed with a Unique Two-Mono-Ubiquitin Mark on Histone H3 Reveals the Basis for DNA Methylation Maintenance. *Mol. Cell* **2017**, *68*, 350-360.e7.
(149) Gaspari, R.; Rechlin, C.; Heine, A.; Bottegoni, G.; Rocchia, W.; Schwarz, D.; Bomke, J.; Gerber, H.-D.; Klebe, G.; Cavalli, A. Kinetic and Structural Insights into the Mechanism of Binding of Sulfonamides to Human Carbonic Anhydrase by Computational and Experimental Studies. *J. Med. Chem.* **2016**, *59*, 4245–4256.
(150) Koppisetti, R. K.; Fulcher, Y. G.; Jurkevich, A.; Prior, S. H.; Xu, J.; Lenoir, M.; Overduin, M.; Van Doren, S. R. Ambidextrous Binding of Cell and Membrane Bilayers by Soluble Matrix Metalloproteinase-12. *Nat. Commun.* **2014**, *5*, 5552.
(151) Chen, J.; Wang, J.; Zhu, W. Zinc Ion-Induced Conformational Changes in New Delphi Metallo-β-Lactamase 1 Probed by Molecular Dynamics Simulations and Umbrella Sampling. *Phys. Chem. Chem. Phys.* **2017**, *19*, 3067–3075.
(152) Lee, C. W.; Chakravorty, D. K.; Chang, F.-M. J.; Reyes-Caballero, H.; Ye, Y.; Merz, K. M.; Giedroc, D. P. Solution Structure of Mycobacterium Tuberculosis NmtR in the Apo State: Insights into Ni(II)-Mediated Allostery. *Biochemistry* **2012**, *51*, 2619–2629.
(153) Schneider, R.; Sharma, A. R.; Rai, A. Introduction to Molecular Dynamics. In *Computational Many-Particle Physics*; Fehske, H., Schneider, R., Weiße, A., Eds.; Lecture Notes in Physics; Springer: Berlin, Heidelberg, 2008; pp 3–40.
(154) Case, D. A.; Cheatham III, T. E.; Darden, T.; Gohlke, H.; Luo, R.; Merz Jr., K. M.; Onufriev, A.; Simmerling, C.; Wang, B.; Woods, R. J. The Amber Biomolecular Simulation Programs. *J. Comput. Chem.* **2005**, *26*, 1668–1688.
(155) Nelson, M. T.; Humphrey, W.; Gursoy, A.; Dalke, A.; Kalé, L. V.; Skeel, R. D.; Schulten, K. NAMD: A Parallel, Object-Oriented Molecular Dynamics Program. *Int. J. Supercomp. Appl. High Perform. Comput.* **1996**, *10*, 251–268.
(156) Berendsen, H. J. C.; van der Spoel, D.; van Drunen, R. GROMACS: A Message-Passing Parallel Molecular Dynamics Implementation. *Comp. Phys. Commun.* **1995**, *91*, 43–56.
(157) Roe, D. R.; Cheatham, T. E. PTRAJ and CPPTRAJ: Software for Processing and Analysis of Molecular Dynamics Trajectory Data. *J. Chem. Theory Comput.* **2013**, *9*, 3084–3095.
(158) Wriggers, W. *TimeScapes Analytics Package*; https://timescapes.biomachina.org/; 2017.

(159) Wu, E. L.; Cheng, X.; Jo, S.; Rui, H.; Song, K. C.; Dávila-Contreras, E. M.; Qi, Y.; Lee, J.; Monje-Galvan, V.; Venable, R. M.; Klauda, J. B.; Im, W. CHARMM-GUI Membrane Builder toward Realistic Biological Membrane Simulations. *J. Comput. Chem.* **2014**, *35*, 1997–2004.

(160) Perdew, J. P. Unified Theory of Exchange and Correlation beyond the Local Density Approximation. In *Electronic Structure of Solids '91*; Ziesche P, Eschrig H, Eds.; Akademie Verlag: Berlin, 1991; Vol. 17, pp 11–20.

(161) Adamo, C.; Barone, V. Exchange Functionals with Improved Long-Range Behavior and Adiabatic Connection Methods without Adjustable Parameters: The MPW and MPW1PW Models. *J. Chem. Phys.* **1998**, *108*, 664–675.

(162) Wiberg, K. B. Application of the Pople-Santry-Segal CNDO Method to the Cyclopropylcarbinyl and Cyclobutyl Cation and to Bicyclobutane. *Tetrahedron* **1968**, *24*, 1083–1096.

(163) Reed, A. E.; Curtiss, L. A.; Weinhold, F. Intermolecular Interactions from a Natural Bond Orbital, Donor-Acceptor Viewpoint. *Chem. Rev.* **1988**, *88*, 899–926.

(164) M. J. Frisch, G. W. Trucks, H. B. Schlegel, G. E. Scuseria,; M. A. Robb, J. R. Cheeseman, G. Scalmani, V. Barone,; B. Mennucci, G. A. Petersson, H. Nakatsuji, M. Caricato,; X. Li, H. P. Hratchian, A. F. Izmaylov, J. Bloino, G. Zheng,; J. L. Sonnenberg, M. Hada, M. Ehara, K. Toyota,; R. Fukuda, J. Hasegawa, M. Ishida, T. Nakajima,; Y. Honda, O. Kitao, H. Nakai, T. Vreven, J. A. Montgomery,; Jr., J. E. Peralta, F. Ogliaro, M. Bearpark, J. J. Heyd,; E. Brothers, K. N. Kudin, V. N. Staroverov, R. Kobayashi,; J. Normand, K. Raghavachari, A. Rendell, J. C. Burant,; S. S. Iyengar, J. Tomasi, M. Cossi, N. Rega, M. J. Millam,; M. Klene, J. E. Knox, J. B. Cross, V. Bakken, C. Adamo,; J. Jaramillo, R. Gomperts, R. E. Stratmann, O. Yazyev,; A. J. Austin, R. Cammi, C. Pomelli, J. W. Ochterski,; R. L. Martin, K. Morokuma, V. G. Zakrzewski, G. A. Voth,; P. Salvador, J. J. Dannenberg, S. Dapprich, A. D. Daniels,; Ö. Farkas, J. B. Foresman, J. V. Ortiz, J. Cioslowski and; D. J. Fox,. *Gaussian 09, Revision D.01, Gaussian, Inc., Wallingford, CT, 2009.*

(165) CDC. The biggest antibiotic-resistant threats in the U.S. https://www.cdc.gov/drugresistance/biggest-threats.html (accessed 2020 -03 -06).

(166) Nelson, R. E.; Hatfield, K. M.; Wolford, H.; Samore, M. H.; Scott, R. D., II; Reddy, S. C.; Olubajo, B.; Paul, P.; Jernigan, J. A.; Baggs, J. National Estimates of Healthcare Costs Associated with Multidrug-Resistant Bacterial Infections Among Hospitalized Patients in the United States. *Clin. Infect. Dis.* **2021**, *72*, S17–S26.

(167) Kraker, M. E. A. de; Stewardson, A. J.; Harbarth, S. Will 10 Million People Die a Year Due to Antimicrobial Resistance by 2050? *PLoS Med.* **2016**, *13*, e1002184.

(168) Dijksteel, G. S.; Ulrich, M. M. W.; Middelkoop, E.; Boekema, B. K. H. L. Review: Lessons Learned from Clinical Trials Using Antimicrobial Peptides (AMPs). *Front. Microbiol.* **2021**, *12*, 616979.

(169) Di Somma, A.; Moretta, A.; Canè, C.; Cirillo, A.; Duilio, A. Antimicrobial and Antibiofilm Peptides. *Biomolecules* **2020**, *10*.

(170) Mahlapuu, M.; Björn, C.; Ekblom, J. Antimicrobial Peptides as Therapeutic Agents: Opportunities and Challenges. *Crit. Rev. Biotechnol.* **2020**, *40*, 978–992.

(171) Parai, D.; Dey, P.; Mukherjee, S. K. Antimicrobial Peptides: An Approach to Combat Resilient Infections. *Curr. Drug Discov. Technol.* **2020**, *17*, 542–552.

(172) Mwangi, J.; Hao, X.; Lai, R.; Zhang, Z.-Y. Antimicrobial Peptides: New Hope in the War against Multidrug Resistance. *Zool. Res.* **2019**, *40*, 488–505.
(173) Kumar, P.; Kizhakkedathu, J. N.; Straus, S. K. Antimicrobial Peptides: Diversity, Mechanism of Action and Strategies to Improve the Activity and Biocompatibility In Vivo. *Biomolecules* **2018**, *8*, E4.
(174) Zelezetsky, I.; Tossi, A. Alpha-Helical Antimicrobial Peptides—Using a Sequence Template to Guide Structure–Activity Relationship Studies. *Biochim. Biophys. Acta Biomembr.* **2006**, *1758*, 1436–1449.
(175) Rončević, T.; Vukičević, D.; Ilić, N.; Krce, L.; Gajski, G.; Tonkić, M.; Goić-Barišić, I.; Zoranić, L.; Sonavane, Y.; Benincasa, M.; Juretić, D.; Maravić, A.; Tossi, A. Antibacterial Activity Affected by the Conformational Flexibility in Glycine–Lysine Based α-Helical Antimicrobial Peptides. *J. Med. Chem.* **2018**, *61*, 2924–2936.
(176) Dubos, R. J. Studies on a Bactericidal Agent Extracted from a Soil Bacillus: I. Preparation of the Agent. Its Activity in Vitro. *J. Exp. Med.* **1939**, *70*, 1–10.
(177) Dubos, R. J. Studies on a Bactericidal Agent Extracted from a Soil Bacillus: II. Protective Effect of the Bactericidal Agent against Experimental Pneumococcus Infections in Mice. *J. Exp. Med.* **1939**, *70*, 11–17.
(178) Dubos, R. J.; Cattaneo, C. Studies on a Bactericidal Agent Extracted from a Soil Bacillus: III. Preparation and Activity of a Protein-Free Fraction. *J. Exp. Med.* **1939**, *70*, 249–256.
(179) Makhlynets, O. V.; Caputo, G. A. Characteristics and Therapeutic Applications of Antimicrobial Peptides. *Biophys. Rev.* **2021**, *2*, 011301.
(180) Hirsch, J. G. Phagocytin: A Bactericidal Substance from Polymorphonuclear Leucocytes. *J. Exp. Med.* **1956**, *103*, 589–611.
(181) Ganz, T.; Selsted, M. E.; Szklarek, D.; Harwig, S. S.; Daher, K.; Bainton, D. F.; Lehrer, R. I. Defensins. Natural Peptide Antibiotics of Human Neutrophils. *J. Clin. Invest.* **1985**, *76*, 1427–1435.
(182) Zhang, L.; Gallo, R. L. Antimicrobial Peptides. *Curr. Biol.* **2016**, *26*, R14–R19.
(183) Matsuzaki, K. Membrane Permeabilization Mechanisms. In *Antimicrobial Peptides: Basics for Clinical Application*; Matsuzaki, K., Ed.; Advances in Experimental Medicine and Biology; Springer: Singapore, 2019; pp 9–16.
(184) Nguyen, L. T.; Haney, E. F.; Vogel, H. J. The Expanding Scope of Antimicrobial Peptide Structures and Their Modes of Action. *Trends Biotechnol.* **2011**, *29*, 464–472.
(185) Epand, R. M. Anionic Lipid Clustering Model. In *Antimicrobial Peptides: Basics for Clinical Application*; Matsuzaki, K., Ed.; Advances in Experimental Medicine and Biology; Springer: Singapore, 2019; pp 65–71.
(186) Lohner, K. Membrane-Active Antimicrobial Peptides as Template Structures for Novel Antibiotic Agents. *Curr. Top. Med. Chem.* **2017**, *17*, 508–519.
(187) Hancock, R. E. W.; Sahl, H.-G. Antimicrobial and Host-Defense Peptides as New Anti-Infective Therapeutic Strategies. *Nat. Biotechnol.* **2006**, *24*, 1551–1557.
(188) Yeaman, M. R.; Yount, N. Y. Mechanisms of Antimicrobial Peptide Action and Resistance. *Pharmacol. Rev.* **2003**, *55*, 27–55.
(189) Lau, J. L.; Dunn, M. K. Therapeutic Peptides: Historical Perspectives, Current Development Trends, and Future Directions. *Bioorg. Med. Chem.* **2018**, *26*, 2700–2707.
(190) Mihailescu, M.; Sorci, M.; Seckute, J.; Silin, V. I.; Hammer, J.; Perrin, B. S.; Hernandez, J. I.; Smajic, N.; Shrestha, A.; Bogardus, K. A.; Greenwood, A. I.; Fu, R.; Blazyk, J.;

Pastor, R. W.; Nicholson, L. K.; Belfort, G.; Cotten, M. L. Structure and Function in Antimicrobial Piscidins: Histidine Position, Directionality of Membrane Insertion, and PH-Dependent Permeabilization. *J. Am. Chem. Soc.* **2019**, *141*, 9837–9853.

(191) Silphaduang, U.; Noga, E. J. Peptide Antibiotics in Mast Cells of Fish. *Nature* **2001**, *414*, 268–269.

(192) Hayden, R. M.; Goldberg, G. K.; Ferguson, B. M.; Schoeneck, M. W.; Libardo, M. D. J.; Mayeux, S. E.; Shrestha, A.; Bogardus, K. A.; Hammer, J.; Pryshchep, S.; Lehman, H. K.; McCormick, M. L.; Blazyk, J.; Angeles-Boza, A. M.; Fu, R.; Cotten, M. L. Complementary Effects of Host Defense Peptides Piscidin 1 and Piscidin 3 on DNA and Lipid Membranes: Biophysical Insights into Contrasting Biological Activities. *J. Phys. Chem. B* **2015**, *119*, 15235–15246.

(193) Shai, Y. Mode of Action of Membrane Active Antimicrobial Peptides. *Pept. Sci.* **2002**, *66*, 236–248.

(194) Guha, S.; Ghimire, J.; Wu, E.; Wimley, W. C. Mechanistic Landscape of Membrane-Permeabilizing Peptides. *Chem. Rev.* **2019**, *119*, 6040–6085.

(195) Libardo, M. D. J.; Bahar, A. A.; Ma, B.; Fu, R.; McCormick, L. E.; Zhao, J.; McCallum, S. A.; Nussinov, R.; Ren, D.; Angeles-Boza, A. M.; Cotten, M. L. Nuclease Activity Gives an Edge to Host-Defense Peptide Piscidin 3 over Piscidin 1, Rendering It More Effective against Persisters and Biofilms. *FEBS J.* **2017**, *284*, 3662–3683.

(196) Perrin, B. S.; Tian, Y.; Fu, R.; Grant, C. V.; Chekmenev, E. Y.; Wieczorek, W. E.; Dao, A. E.; Hayden, R. M.; Burzynski, C. M.; Venable, R. M.; Sharma, M.; Opella, S. J.; Pastor, R. W.; Cotten, M. L. High-Resolution Structures and Orientations of Antimicrobial Peptides Piscidin 1 and Piscidin 3 in Fluid Bilayers Reveal Tilting, Kinking, and Bilayer Immersion. *J. Am. Chem. Soc.* **2014**, *136*, 3491–3504.

(197) Chekmenev, E. Y.; Vollmar, B. S.; Cotten, M. Can Antimicrobial Peptides Scavenge around a Cell in Less than a Second? *Biochim. Biophys. Acta Biomembr.* **2010**, *1798*, 228–234.

(198) Lauth, X.; Shike, H.; Burns, J. C.; Westerman, M. E.; Ostland, V. E.; Carlberg, J. M.; Van Olst, J. C.; Nizet, V.; Taylor, S. W.; Shimizu, C.; Bulet, P. Discovery and Characterization of Two Isoforms of Moronecidin, a Novel Antimicrobial Peptide from Hybrid Striped Bass. *J. Biol. Chem.* **2002**, *277*, 5030–5039.

(199) Sung, W. S.; Lee, J.; Lee, D. G. Fungicidal Effect of Piscidin on Candida Albicans: Pore Formation in Lipid Vesicles and Activity in Fungal Membranes. *Biol. Pharm. Bull.* **2008**, *31*, 1906–1910.

(200) Menousek, J.; Mishra, B.; Hanke, M. L.; Heim, C. E.; Kielian, T.; Wang, G. Database Screening and in Vivo Efficacy of Antimicrobial Peptides against Meticillin-Resistant Staphylococcus Aureus USA300. *Int. J. Antimicrob. Agents* **2012**, *39*, 402–406.

(201) Wang, G.; Watson, K. M.; Peterkofsky, A.; Buckheit, R. W. Identification of Novel Human Immunodeficiency Virus Type 1-Inhibitory Peptides Based on the Antimicrobial Peptide Database. *Antimicrob. Agents Chemother.* **2010**, *54*, 1343–1346.

(202) Lin, H.-J.; Huang, T.-C.; Muthusamy, S.; Lee, J.-F.; Duann, Y.-F.; Lin, C.-H. Piscidin-1, an Antimicrobial Peptide from Fish (Hybrid Striped Bass Morone Saxatilis x M. Chrysops), Induces Apoptotic and Necrotic Activity in HT1080 Cells. *Zool. Sci.* **2012**, *29*, 327–332.

(203) Libardo, M. D. J.; Gorbatyuk, V. Y.; Angeles-Boza, A. M. Central Role of the Copper-Binding Motif in the Complex Mechanism of Action of Ixosin: Enhancing Oxidative Damage and Promoting Synergy with Ixosin B. *ACS Infect. Dis.* **2016**, *2*, 71–81.
(204) Rai, R. K.; De Angelis, A.; Greenwood, A.; Opella, S. J.; Cotten, M. L. Metal-Ion Binding to Host Defense Peptide Piscidin 3 Observed in Phospholipid Bilayers by Magic Angle Spinning Solid-State NMR. *ChemPhysChem* **2019**, *20*, 295–301.
(205) Paredes, S. D.; Kim, S.; Rooney, M. T.; Greenwood, A. I.; Hristova, K.; Cotten, M. L. Enhancing the Membrane Activity of Piscidin 1 through Peptide Metallation and the Presence of Oxidized Lipid Species: Implications for the Unification of Host Defense Mechanisms at Lipid Membranes. *Biochim. Biophys. Acta Biomembr.* **2020**, 183236.
(206) Mattila, J.-P.; Sabatini, K.; Kinnunen, P. K. J. Oxidized Phospholipids as Potential Molecular Targets for Antimicrobial Peptides. *Biochim. Biophys. Acta Biomembr.* **2008**, *1778*, 2041–2050.
(207) Ayala, A.; Muñoz, M. F.; Argüelles, S. Lipid Peroxidation: Production, Metabolism, and Signaling Mechanisms of Malondialdehyde and 4-Hydroxy-2-Nonenal. *Oxid. Med. Cell Longev.* **2014**, *2014*.
(208) Avery, S. V. Molecular Targets of Oxidative Stress. *Biochem. J.* **2011**, *434*, 201–210.
(209) Moravec, A. R.; Siv, A. W.; Hobby, C. R.; Lindsay, E. N.; Norbash, L. V.; Shults, D. J.; Symes, S. J. K.; Giles, D. K. Exogenous Polyunsaturated Fatty Acids Impact Membrane Remodeling and Affect Virulence Phenotypes among Pathogenic Vibrio Species. *Appl. Environ. Microbiol.* **2017**, *83*.
(210) Wang, L.-H.; Zeng, X.-A.; Wang, M.-S.; Brennan, C. S.; Gong, D. Modification of Membrane Properties and Fatty Acids Biosynthesis-Related Genes in Escherichia Coli and Staphylococcus Aureus: Implications for the Antibacterial Mechanism of Naringenin. *Biochim. Biophys. Acta Biomembr.* **2018**, *1860*, 481–490.
(211) Wallgren, M.; Beranova, L.; Pham, Q. D.; Linh, K.; Lidman, M.; Procek, J.; Cyprych, K.; Kinnunen, P. K. J.; Hof, M.; Gröbner, G. Impact of Oxidized Phospholipids on the Structural and Dynamic Organization of Phospholipid Membranes: A Combined DSC and Solid State NMR Study. *Faraday Discuss.* **2013**, *161*, 499–513; discussion 563-589.
(212) Smith, H. L.; Howland, M. C.; Szmodis, A. W.; Li, Q.; Daemen, L. L.; Parikh, A. N.; Majewski, J. Early Stages of Oxidative Stress-Induced Membrane Permeabilization: A Neutron Reflectometry Study. *J. Am. Chem. Soc.* **2009**, *131*, 3631–3638.
(213) Khandelia, H.; Mouritsen, O. G. Lipid Gymnastics: Evidence of Complete Acyl Chain Reversal in Oxidized Phospholipids from Molecular Simulations. *Biophys. J.* **2009**, *96*, 2734–2743.
(214) Perrin, B. S.; Sodt, A. J.; Cotten, M. L.; Pastor, R. W. The Curvature Induction of Surface-Bound Antimicrobial Peptides Piscidin 1 and Piscidin 3 Varies with Lipid Chain Length. *J. Membr. Biol.* **2015**, *248*, 455–467.
(215) Perrin, B. S.; Fu, R.; Cotten, M. L.; Pastor, R. W. Simulations of Membrane-Disrupting Peptides II: AMP Piscidin 1 Favors Surface Defects over Pores. *Biophys. J.* **2016**, *111*, 1258–1266.
(216) Kinnunen, P. K. J.; Kaarniranta, K.; Mahalka, A. K. Protein-Oxidized Phospholipid Interactions in Cellular Signaling for Cell Death: From Biophysics to Clinical Correlations. *Biochim. Biophys. Acta Biomembr.* **2012**, *1818*, 2446–2455.

(217) Wallgren, M.; Lidman, M.; Pham, Q. D.; Cyprych, K.; Gröbner, G. The Oxidized Phospholipid PazePC Modulates Interactions between Bax and Mitochondrial Membranes. *Biochim. Biophys. Acta Biomembr.* **2012**, *1818*, 2718–2724.
(218) Case, D. A. et al. *AMBER 18 (AMBER 16)*; 2018.
(219) Jo, S.; Kim, T.; Iyer, V. G.; Im, W. CHARMM-GUI: A Web-Based Graphical User Interface for CHARMM. *J. Comput. Chem.* **2008**, *29*, 1859–1865.
(220) Wang, J.; Wang, W.; Kollman, P. A.; Case, D. A. Antechamber, an Accessory Software Package for Molecular Mechanical Calculations. *J. Am. Chem. Soc.* **2001**, *222*, U403.
(221) Jorgensen, W. L.; Chandrasekhar, J.; Madura, J. D.; Impey, R. W.; Klein, M. L. Comparison of Simple Potential Functions for Simulating Liquid Water. *J. Chem. Phys.* **1983**, *79*, 926–935.
(222) Joung, I. S.; Cheatham, T. E. Determination of Alkali and Halide Monovalent Ion Parameters for Use in Explicitly Solvated Biomolecular Simulations. *J. Phys. Chem. B* **2008**, *112*, 9020–9041.
(223) Salomon-Ferrer, R.; Götz, A. W.; Poole, D.; Le Grand, S.; Walker, R. C. Routine Microsecond Molecular Dynamics Simulations with AMBER on GPUs. 2. Explicit Solvent Particle Mesh Ewald. *J. Chem. Theory Comput.* **2013**, *9*, 3878–3888.
(224) J. Dickson, C.; Rosso, L.; M. Betz, R.; C. Walker, R.; R. Gould, I. GAFFlipid: A General Amber Force Field for the Accurate Molecular Dynamics Simulation of Phospholipid. *Soft Matter* **2012**, *8*, 9617–9627.
(225) Rosso, L.; Gould, I. R. Structure and Dynamics of Phospholipid Bilayers Using Recently Developed General All-Atom Force Fields. *J. Comput. Chem.* **2008**, *29*, 24–37.
(226) Skjevik, Å. A.; Madej, B. D.; Dickson, C. J.; Lin, C.; Teigen, K.; Walker, R. C.; Gould, I. R. Simulation of Lipid Bilayer Self-Assembly Using All-Atom Lipid Force Fields. *Phys. Chem. Chem. Phys.* **2016**, *18*, 10573–10584.
(227) Kučerka, N.; Tristram-Nagle, S.; Nagle, J. F. Structure of Fully Hydrated Fluid Phase Lipid Bilayers with Monounsaturated Chains. *J. Membr. Biol.* **2006**, *208*, 193–202.
(228) Kučerka, N.; Nieh, M.-P.; Katsaras, J. Fluid Phase Lipid Areas and Bilayer Thicknesses of Commonly Used Phosphatidylcholines as a Function of Temperature. *Biochim. Biophys. Acta Biomembr.* **2011**, *1808*, 2761–2771.
(229) Binder, H.; Gawrisch, K. Effect of Unsaturated Lipid Chains on Dimensions, Molecular Order and Hydration of Membranes. *J. Phys. Chem. B* **2001**, *105*, 12378–12390.
(230) Wang, Y.; Zhao, T.; Wei, D.; Strandberg, E.; Ulrich, A. S.; Ulmschneider, J. P. How Reliable Are Molecular Dynamics Simulations of Membrane Active Antimicrobial Peptides? *Biochim. Biophys. Acta Biomembr.* **2014**, *1838*, 2280–2288.
(231) Faulkner, C.; Santos-Carballal, D.; Plant, D. F.; de Leeuw, N. H. Atomistic Molecular Dynamics Simulations of Propofol and Fentanyl in Phosphatidylcholine Lipid Bilayers. *ACS Omega* **2020**, *5*, 14340–14353.
(232) Fu, R.; Rooney, M. T.; Zhang, R.; Cotten, M. L. Coordination of Redox Ions within a Membrane-Binding Peptide: A Tale of Aromatic Rings. *J. Phys. Chem. Lett.* **2021**, *12*, 4392–4399.
(233) Gallivan, J. P.; Dougherty, D. A. Cation-π Interactions in Structural Biology. *Proc. Natl. Acad. Sci. U.S.A.* **1999**, *96*, 9459–9464.
(234) Yorita, H.; Otomo, K.; Hiramatsu, H.; Toyama, A.; Miura, T.; Takeuchi, H. Evidence for the Cation−π Interaction between Cu2+ and Tryptophan. *J. Am. Chem. Soc.* **2008**, *130*, 15266–15267.

(235) Libardo, M. D. J.; Bahar, A. A.; Ma, B.; Fu, R.; McCormick, L. E.; Zhao, J.; McCallum, S. A.; Nussinov, R.; Ren, D.; Angeles-Boza, A. M.; Cotten, M. L. Nuclease Activity Gives an Edge to Host-Defense Peptide Piscidin 3 over Piscidin 1, Rendering It More Effective against Persisters and Biofilms. *FEBS J.* **2017**, *284*, 3662–3683.

(236) Meyer, F. de; Smit, B. Effect of Cholesterol on the Structure of a Phospholipid Bilayer. *Proc. Natl. Acad. Sci. U.S.A.* **2009**, *106*, 3654–3658.

(237) Róg, T.; Pasenkiewicz-Gierula, M.; Vattulainen, I.; Karttunen, M. Ordering Effects of Cholesterol and Its Analogues. *Biochim. Biophys. Acta Biomembr.* **2009**, *1788*, 97–121.

(238) Berg, J. M. Zinc Finger Domains: Hypotheses and Current Knowledge. *Annu. Rev. Biophys. Biophys. Chem.* **1990**, *19*, 405–421.

(239) Coleman, J. E. Zinc Proteins: Enzymes, Storage Proteins, Transcription Factors, and Replication Proteins. *Annu. Rev. Biochem.* **1992**, *61*, 897–946.

(240) Berg, J. M.; Godwin, H. A. Lessons from Zinc-Binding Peptides. *Annu. Rev. Biophys. Biomol. Struct.* **1997**, *26*, 357–371.

(241) Maret, W. Zinc and Sulfur: A Critical Biological Partnership. *Biochem.* **2004**, *43*, 3301–3309.

(242) Kröncke, K.-D.; Klotz, L.-O. Zinc Fingers as Biologic Redox Switches? *Antioxid. Redox Signal.* **2009**, *11*, 1015–1027.

(243) Cassandri, M.; Smirnov, A.; Novelli, F.; Pitolli, C.; Agostini, M.; Malewicz, M.; Melino, G.; Raschellà, G. Zinc-Finger Proteins in Health and Disease. *Cell Death Discov.* **2017**, *3*, 1–12.

(244) Yusuf, A. P.; Abubakar, M. B.; Malami, I.; Ibrahim, K. G.; Abubakar, B.; Bello, M. B.; Qusty, N.; Elazab, S. T.; Imam, M. U.; Alexiou, A.; Batiha, G. E.-S. Zinc Metalloproteins in Epigenetics and Their Crosstalk. *Life* **2021**, *11*, 186.

(245) Del Río, S.; Setzer, D. R. High Yield Purification of Active Transcription Factor IIIA Expressed in E. Coli. *Nucleic Acids Res.* **1991**, *19*, 6197–6203.

(246) Brayer, K. J.; Kulshreshtha, S.; Segal, D. J. The Protein-Binding Potential of C2H2 Zinc Finger Domains. *Cell Biochem. Biophys.* **2008**, *51*, 9–19.

(247) Fan, Y.; Lu, D. The Ikaros Family of Zinc-Finger Proteins. *Acta Pharm. Sin. B* **2016**, *6*, 513–521.

(248) Suske, G.; Bruford, E.; Philipsen, S. Mammalian SP/KLF Transcription Factors: Bring in the Family. *Genomics* **2005**, *85*, 551–556.

(249) Narayan, V. A.; Kriwacki, R. W.; Caradonna, J. P. Structures of Zinc Finger Domains from Transcription Factor Sp1. Insights into Sequence-Specific Protein-DNA Recognition. *J. Biol. Chem.* **1997**, *272*, 7801–7809.

(250) Christy, B.; Nathans, D. DNA Binding Site of the Growth Factor-Inducible Protein Zif268. *Proc. Natl. Acad. Sci. U.S.A.* **1989**, *86*, 8737–8741.

(251) Rio, S. D.; Setzer, D. R. The Role of Zinc Fingers in Transcriptional Activation by Transcription Factor IIIA. *Proc. Natl. Acad. Sci. U.S.A.* **1993**, *90*, 168–172.

(252) Rice, W. G.; Supko, J. G.; Malspeis, L.; Buckheit, R. W.; Clanton, D.; Bu, M.; Graham, L.; Schaeffer, C. A.; Turpin, J. A.; Domagala, J.; Gogliotti, R.; Bader, J. P.; Halliday, S. M.; Coren, L.; Sowder, R. C.; Arthur, L. O.; Henderson, L. E. Inhibitors of HIV Nucleocapsid Protein Zinc Fingers as Candidates for the Treatment of AIDS. *Science* **1995**, *270*, 1194–1197.

(253) Jacob, C.; Maret, W.; Vallee, B. L. Ebselen, a Selenium-Containing Redox Drug, Releases Zinc from Metallothionein. *Biochem. Biophys. Res. Commun.* **1998**, *248*, 569–573.
(254) Jacob, C.; Maret, W.; Vallee, B. L. Selenium Redox Biochemistry of Zinc–Sulfur Coordination Sites in Proteins and Enzymes. *Proc. Natl. Acad. Sci. U.S.A.* **1999**, *96*, 1910–1914.
(255) Korichneva, I.; Hoyos, B.; Chua, R.; Levi, E.; Hammerling, U. Zinc Release from Protein Kinase C as the Common Event during Activation by Lipid Second Messenger or Reactive Oxygen. *J. Biol. Chem.* **2002**, *277*, 44327–44331.
(256) Blessing, H.; Kraus, S.; Heindl, P.; Bal, W.; Hartwig, A. Interaction of Selenium Compounds with Zinc Finger Proteins Involved in DNA Repair. *Eur. J. Biochem.* **2004**, *271*, 3190–3199.
(257) Larabee, J. L.; Hocker, J. R.; Hanas, J. S. Cys Redox Reactions and Metal Binding of a Cys2His2 Zinc Finger. *Arch. Biochem. Biophys.* **2005**, *434*, 139–149.
(258) Zhou, X.; Cooper, K. L.; Sun, X.; Liu, K. J.; Hudson, L. G. Selective Sensitization of Zinc Finger Protein Oxidation by Reactive Oxygen Species through Arsenic Binding. *J. Biol. Chem.* **2015**, *290*, 18361–18369.
(259) Zhou, X.; Ding, X.; Shen, J.; Yang, D.; Hudson, L. G.; Liu, K. J. Peroxynitrite Contributes to Arsenic-Induced PARP-1 Inhibition through ROS/RNS Generation. *Toxicol. Appl. Pharmacol.* **2019**, *378*, 114602.
(260) Maret, W. The Redox Biology of Redox-Inert Zinc Ions. *Free Radic. Biol. Med.* **2019**, *134*, 311–326.
(261) Zhou, X.; Speer, R. M.; Volk, L.; Hudson, L. G.; Liu, K. J. Arsenic Co-Carcinogenesis: Inhibition of DNA Repair and Interaction with Zinc Finger Proteins. *Sem. Cancer Biol.* **2021**.
(262) Lenstra, D. C.; Al Temimi, A. H. K.; Mecinović, J. Inhibition of Histone Lysine Methyltransferases G9a and GLP by Ejection of Structural Zn(II). *Bioorg. Med. Chem. Lett.* **2018**, *28*, 1234–1238.
(263) Brahemi, G.; Kona, F. R.; Fiasella, A.; Buac, D.; Soukupová, J.; Brancale, A.; Burger, A. M.; Westwell, A. D. Exploring the Structural Requirements for Inhibition of the Ubiquitin E3 Ligase Breast Cancer Associated Protein 2 (BCA2) as a Treatment for Breast Cancer. *J. Med. Chem.* **2010**, *53*, 2757–2765.
(264) Ye, B.; Yang, G.; Li, Y.; Zhang, C.; Wang, Q.; Yu, G. ZNF143 in Chromatin Looping and Gene Regulation. *Front. Genet.* **2020**, *11*, 338.
(265) Izumi, H.; Wakasugi, T.; Shimajiri, S.; Tanimoto, A.; Sasaguri, Y.; Kashiwagi, E.; Yasuniwa, Y.; Akiyama, M.; Han, B.; Wu, Y.; Uchiumi, T.; Arao, T.; Nishio, K.; Yamazaki, R.; Kohno, K. Role of ZNF143 in Tumor Growth through Transcriptional Regulation of DNA Replication and Cell-Cycle-Associated Genes. *Cancer Sci.* **2010**, *101*, 2538–2545.
(266) Paek, A. R.; Mun, J. Y.; Hong, K.-M.; Lee, J.; Hong, D. W.; You, H. J. Zinc Finger Protein 143 Expression Is Closely Related to Tumor Malignancy via Regulating Cell Motility in Breast Cancer. *BMB Rep.* **2017**, *50*, 621–627.
(267) Theunissen, O.; Rudt, F.; Guddat, U.; Mentzel, H.; Pieler, T. RNA and DNA Binding Zinc Fingers in Xenopus TFIIIA. *Cell* **1992**, *71*, 679–690.

(268) Tan, C.; Li, W.; Wang, W. Localized Frustration and Binding-Induced Conformational Change in Recognition of 5S RNA by TFIIIA Zinc Finger. *J. Phys. Chem. B* **2013**, *117*, 15917–15925.
(269) Dixit, P. D.; Asthagiri, D. An Elastic-Network-Based Local Molecular Field Analysis of Zinc Finger Proteins. *J. Phys. Chem. B* **2011**, *115*, 7374–7382.
(270) Temiz, A. N.; Benos, P. V.; Camacho, C. J. Electrostatic Hot Spot on DNA-Binding Domains Mediates Phosphate Desolvation and the Pre-Organization of Specificity Determinant Side Chains. *Nucleic Acids Res.* **2010**, *38*, 2134–2144.
(271) Tsui, V.; Radhakrishnan, I.; Wright, P. E.; Case, D. A. NMR and Molecular Dynamics Studies of the Hydration of a Zinc Finger-DNA Complex11Edited by M. F. Summers. *J. Mol. Biol.* **2000**, *302*, 1101–1117.
(272) Liu, L.; Wade, R. C.; Heermann, D. W. A Multiscale Approach to Simulating the Conformational Properties of Unbound Multi-C2H2 Zinc Finger Proteins. *Proteins: Struct. Funct. Bioinf.* **2015**, *83*, 1604–1615.
(273) Pelham, H. R.; Brown, D. D. A Specific Transcription Factor That Can Bind Either the 5S RNA Gene or 5S RNA. *Proc. Natl. Acad. Sci. U.S.A.* **1980**, *77*, 4170–4174.
(274) Segall, J.; Matsui, T.; Roeder, R. G. Multiple Factors Are Required for the Accurate Transcription of Purified Genes by RNA Polymerase III. *J. Biol. Chem.* **1980**, *255*, 11986–11991.
(275) Sakonju, S.; Bogenhagen, D. F.; Brown, D. D. A Control Region in the Center of the 5S RNA Gene Directs Specific Initiation of Transcription: I. The 5′ Border of the Region. *Cell* **1980**, *19*, 13–25.
(276) Bogenhagen, D. F.; Sakonju, S.; Brown, D. D. A Control Region in the Center of the 5S RNA Gene Directs Specific Initiation of Transcription: II. The 3′ Border of the Region. *Cell* **1980**, *19*, 27–35.
(277) Picard, B.; Wegnez, M. Isolation of a 7S Particle from Xenopus Laevis Oocytes: A 5S RNA-Protein Complex. *Proc. Natl. Acad. Sci. U.S.A.* **1979**, *76*, 241–245.
(278) Theunissen, O.; Rudt, F.; Pieler, T. Structural Determinants in 5S RNA and TFIIIA for 7S RNP Formation. *Eur. J. Biochem.* **1998**, *258*, 758–767.
(279) Baudin, F.; Romaniuk, P. J. A Difference in the Importance of Bulged Nucleotides and Their Parent Base Pairs in the Binding of Transcription Factor IIIA to Xenopus 5S RNA and 5S RNA Genes. *Nucleic Acids Res.* **1989**, *17*, 2043–2056.
(280) You, Q.; Veldhoen, N.; Baudin, F.; Romaniuk, P. J. Mutations in 5S DNA and 5S RNA Have Different Effects on the Binding of Xenopus Transcription Factor IIIA. *Biochemistry* **1991**, *30*, 2495–2500.
(281) Romaniuk, P. J.; Stevenson, I. L. de; Wong, H.-H. A. Defining the Binding Site of Xenopus Transcription Factor IIIA on 5S RNA Using Truncated and Chimeric 5S RNA Molecules. *Nucleic Acids Res.* **1987**, *15*, 2737–2755.
(282) Romaniuk, P. J. Characterization of the RNA Binding Properties of Transcription Factor IIIA of Xenopus Laevis Oocytes. *Nucleic Acids Res.* **1985**, *13*, 5369–5387.
(283) Clemens, K. R.; Wolf, V.; McBryant, S. J.; Zhang, P.; Liao, X.; Wright, P. E.; Gottesfeld, J. M. Molecular Basis for Specific Recognition of Both RNA and DNA by a Zinc Finger Protein. *Science* **1993**, *260*, 530–533.
(284) McBryant, S. J.; Veldhoen, N.; Gedulin, B.; Leresche, A.; Foster, M. P.; Wright, P. E.; Romaniuk, P. J.; Gottesfeld, J. M. Interaction of the RNA Binding Fingers of Xenopus

Transcription Factor IIIA with Specific Regions of 5S Ribosomal RNA. *J. Mol. Biol.* **1995**, *248*, 44–57.
(285) Hamilton, T. B.; Turner, J.; Barilla, K.; Romaniuk, P. J. Contribution of Individual Amino Acids to the Nucleic Acid Binding Activities of the Xenopus Zinc Finger Proteins TFIIIIA and P43. *Biochemistry* **2001**, *40*, 6093–6101.
(286) Friesen, W. J.; Darby, M. K. Phage Display of RNA Binding Zinc Fingers from Transcription Factor IIIA. *J. Biol. Chem.* **1997**, *272*, 10994–10997.
(287) Lee, B. M.; Xu, J.; Clarkson, B. K.; Martinez-Yamout, M. A.; Dyson, H. J.; Case, D. A.; Gottesfeld, J. M.; Wright, P. E. Induced Fit and "Lock and Key" Recognition of 5S RNA by Zinc Fingers of Transcription Factor IIIA. *J. Mol. Biol.* **2006**, *357*, 275–291.
(288) Searles, M. A.; Lu, D.; Klug, A. The Role of the Central Zinc Fingers of Transcription Factor IIIA in Binding to 5 S RNA11Edited by D. E. Draper. *J. Mol. Biol.* **2000**, *301*, 47–60.
(289) Setzer, D. R.; Menezes, S. R.; Rio, S. D.; Hung, V. S.; Subramanyan, G. Functional Interactions between the Zinc Fingers of Xenopus Transcription Factor IIIA during 5S RRNA Binding. *RNA* **1996**, *2*, 1254–1269.
(290) Lu, D.; Alexandra Searles, M.; Klug, A. Crystal Structure of a Zinc-Finger–RNA Complex Reveals Two Modes of Molecular Recognition. *Nature* **2003**, *426*, 96–100.
(291) Palermo, G.; Casalino, L.; Magistrato, A.; Andrew McCammon, J. Understanding the Mechanistic Basis of Non-Coding RNA through Molecular Dynamics Simulations. *J. Struct. Biol.* **2019**, *206*, 267–279.
(292) Anandakrishnan, R.; Aguilar, B.; Onufriev, A. V. H++ 3.0: Automating PK Prediction and the Preparation of Biomolecular Structures for Atomistic Molecular Modeling and Simulations. *Nucleic Acids Res.* **2012**, *40*, W537–W541.
(293) Kabsch, W.; Sander, C. Dictionary of Protein Secondary Structure: Pattern Recognition of Hydrogen-Bonded and Geometrical Features. *Biopolymers* **1983**, *22*, 2577–2637.
(294) Wriggers, W.; Stafford, K. A.; Shan, Y.; Piana, S.; Maragakis, P.; Lindorff-Larsen, K.; Miller, P. J.; Gullingsrud, J.; Rendleman, C. A.; Eastwood, M. P.; Dror, R. O.; Shaw, D. E. Automated Event Detection and Activity Monitoring in Long Molecular Dynamics Simulations. *J. Chem. Theory Comput.* **2009**, *5*, 2595–2605.
(295) Kovacs, J. A.; Wriggers, W. Spatial Heat Maps from Fast Information Matching of Fast and Slow Degrees of Freedom: Application to Molecular Dynamics Simulations. *J. Phys. Chem. B* **2016**, *120*, 8473–8484.
(296) Humphrey, W.; Dalke, A.; Schulten, K. VMD: Visual Molecular Dynamics. *J. Mol. Graph.* **1996**, *14*, 33–38.
(297) Schrödinger, LLC. The PyMOL Molecular Graphics System, Version 2.3.4, 2020.
(298) Lu, D.; Klug, A. Invariance of the Zinc Finger Module: A Comparison of the Free Structure with Those in Nucleic-Acid Complexes. *Proteins: Struct. Funct. Genet.* **2007**, *67*, 508–512.
(299) Forman, H. J.; Fukuto, J.; Torres, M. *Signal Transduction by Reactive Oxygen and Nitrogen Species: Pathways and Chemical Principles*; Springer, 2003.
(300) Forman, H. J.; Fukuto, J. M.; Miller, T.; Zhang, H.; Rinna, A.; Levy, S. The Chemistry of Cell Signaling by Reactive Oxygen and Nitrogen Species and 4-Hydroxynonenal. *Arch. Biochem. Biophys.* **2008**, *477*, 183–195.
(301) Finkel, T. Signal Transduction by Reactive Oxygen Species. *J. Cell Biol.* **2011**, *194*, 7–15.

(302) Halliwell, B. Free Radicals, Antioxidants, and Human Disease: Curiosity, Cause, or Consequence? *Lancet* **1994**, *344*, 721–724.
(303) Landar, A.; Zmijewski, J. W.; Dickinson, D. A.; Le Goffe, C.; Johnson, M. S.; Milne, G. L.; Zanoni, G.; Vidari, G.; Morrow, J. D.; Darley-Usmar, V. M. Interaction of Electrophilic Lipid Oxidation Products with Mitochondria in Endothelial Cells and Formation of Reactive Oxygen Species. *Am. J. Physiol. Heart Circ. Physiol.* **2006**, *290*, 1777–1787.
(304) Imlay, J. A. Cellular Defenses against Superoxide and Hydrogen Peroxide. *Annu. Rev. Biochem.* **2008**, *77*, 755–776.
(305) Murphy, M. P. How Mitochondria Produce Reactive Oxygen Species. *Biochem. J.* **2009**, *417*, 1–13.
(306) Imlay, J. A. The Molecular Mechanisms and Physiological Consequences of Oxidative Stress: Lessons from a Model Bacterium. *Nat. Rev. Microbiol.* **2013**, *11*, 443.
(307) Roy, J.; Galano, J.-M.; Durand, T.; Le Guennec, J.-Y.; Lee, J. C.-Y. Physiological Role of Reactive Oxygen Species as Promoters of Natural Defenses. *FASEB J.* **2017**, *31*, 3729–3745.
(308) Schöneich, C. Reactive Oxygen Species and Biological Aging: A Mechanistic Approach. *Exp. Gerontol.* **1999**, *34*, 19–34.
(309) Chatgilialoglu, C.; O'Neill, P. Free Radicals Associated with DNA Damage. *Exp. Gerontol.* **2001**, *36*, 1459–1471.
(310) Cherubini, A.; Ruggiero, C.; Polidori, M. C.; Mecocci, P. Potential Markers of Oxidative Stress in Stroke. *Free Radic. Biol. Med.* **2005**, *39*, 841–852.
(311) Valko, M.; Rhodes, C. J.; Moncol, J.; Izakovic, M.; Mazur, M. Free Radicals, Metals and Antioxidants in Oxidative Stress-Induced Cancer. *Chem. Biol. Interact.* **2006**, *160*, 1–40.
(312) Dalle-Donne, I.; Rossi, R.; Colombo, R.; Giustarini, D.; Milzani, A. Biomarkers of Oxidative Damage in Human Disease. *Clin. Chem.* **2006**, *52*, 601–623.
(313) De Flora, S.; Izzotti, A. Mutagenesis and Cardiovascular Diseases: Molecular Mechanisms, Risk Factors, and Protective Factors. *Mutat. Res.* **2007**, *621*, 5–17.
(314) Andreassi, M. G. DNA Damage, Vascular Senescence and Atherosclerosis. *J. Mol. Med.* **2008**, *86*, 1033.
(315) Jackson, S. P.; Bartek, J. The DNA-Damage Response in Human Biology and Disease. *Nature* **2009**, *461*, 1071–1078.
(316) Gutierrez, J.; Ballinger, S. W.; Darley-Usmar, V. M.; Landar, A. Free Radicals, Mitochondria, and Oxidized Lipids: The Emerging Role in Signal Transduction in Vascular Cells. *Circ. Res.* **2006**, *99*, 924–932.
(317) Balasaheb Nimse, S.; Pal, D. Free Radicals, Natural Antioxidants, and Their Reaction Mechanisms. *RSC Adv.* **2015**, *5*, 27986–28006.
(318) Hashemy, S. I.; Holmgren, A. Regulation of the Catalytic Activity and Structure of Human Thioredoxin 1 via Oxidation and S-Nitrosylation of Cysteine Residues. *J. Biol. Chem.* **2008**, *283*, 21890–21898.
(319) Birben, E.; Sahiner, U. M.; Sackesen, C.; Erzurum, S.; Kalayci, O. Oxidative Stress and Antioxidant Defense. *World Allergy Organ. J.* **2012**, *5*, 9–19.
(320) Stohs, S. J.; Bagchi, D. Oxidative Mechanisms in the Toxicity of Metal Ions. *Free Radic. Biol. Med.* **1995**, *18*, 321–336.
(321) Ensing, B.; Baerends, E. J. Reaction Path Sampling of the Reaction between Iron(II) and Hydrogen Peroxide in Aqueous Solution. *J. Phys. Chem. A* **2002**, *106*, 7902–7910.

(322) Ensing, B.; Buda, F.; E. Blöchl, P.; Jan Baerends, E. A Car–Parrinello Study of the Formation of Oxidizing Intermediates from Fenton's Reagent in Aqueous Solution. *Phys. Chem. Chem. Phys.* **2002**, *4*, 3619–3627.
(323) Buda, F.; Ensing, B.; Gribnau, M. C. M.; Baerends, E. J. DFT Study of the Active Intermediate in the Fenton Reaction. *Chem. Eur. J.* **2001**, *7*, 2775–2783.
(324) Anastasi, A. E.; Lienke, A.; Comba, P.; Rohwer, H.; McGrady, J. E. Competing Radical and Non-Radical Pathways for the Decomposition of LFeII(H2O2) Complexes: A Density Functional Study. *Eur. J. Inorg. Chem.* **2007**, *2007*, 65–73.
(325) Sigel, A.; Sigel, H. *Metal Ions in Biological Systems | Interrelations between Free Radicals and Metal Ions in Life Processes*; Marcel Dekker: New York, 1999; Vol. 36.
(326) Park, S.; Imlay, J. A. High Levels of Intracellular Cysteine Promote Oxidative DNA Damage by Driving the Fenton Reaction. *J. Bacteriol.* **2003**, *185*, 1942–1950.
(327) Kell, D. B. Towards a Unifying, Systems Biology Understanding of Large-Scale Cellular Death and Destruction Caused by Poorly Liganded Iron: Parkinson's, Huntington's, Alzheimer's, Prions, Bactericides, Chemical Toxicology and Others as Examples. *Arch. Toxicol.* **2010**, *84*, 825–889.
(328) Angelé-Martínez, C.; Goodman, C.; Brumaghim, J. Metal-Mediated DNA Damage and Cell Death: Mechanisms, Detection Methods, and Cellular Consequences. *Metallomics* **2014**, *6*, 1358–1381.
(329) Kalam, M. A.; Haraguchi, K.; Chandani, S.; Loechler, E. L.; Moriya, M.; Greenberg, M. M.; Basu, A. K. Genetic Effects of Oxidative DNA Damages: Comparative Mutagenesis of the Imidazole Ring-Opened Formamidopyrimidines (Fapy Lesions) and 8-Oxo-Purines in Simian Kidney Cells. *Nucleic Acids Res.* **2006**, *34*, 2305–2315.
(330) Rai, P.; Cole, T. D.; Wemmer, D. E.; Linn, S. Localization of Fe2+ at an RTGR Sequence within a DNA Duplex Explains Preferential Cleavage by Fe2+ and H2O2. *J. Mol. Biol.* **2001**, *312*, 1089–1101.
(331) Steenken, S. Purine Bases, Nucleosides, and Nucleotides: Aqueous Solution Redox Chemistry and Transformation Reactions of Their Radical Cations and e- and OH Adducts. *Chem. Rev.* **1989**, *89*, 503–520.
(332) Rai, P.; Wemmer, D. E.; Linn, S. Preferential Binding and Structural Distortion by Fe2+ at RGGG-Containing DNA Sequences Correlates with Enhanced Oxidative Cleavage at Such Sequences. *Nucleic Acids Res.* **2005**, *33*, 497–510.
(333) Henle, E. S.; Han, Z.; Tang, N.; Rai, P.; Luo, Y.; Linn, S. Sequence-Specific DNA Cleavage by Fe2+-Mediated Fenton Reactions Has Possible Biological Implications. *J. Biol. Chem.* **1999**, *274*, 962–971.
(334) Lee, J.; Kim, Y.; Lim, S.; Jo, K. Single-Molecule Visualization of ROS-Induced DNA Damage in Large DNA Molecules. *Analyst* **2016**, *141*, 847–852.
(335) Sarker, A. H.; Watanabe, S.; Seki, S.; Akiyama, T.; Okada, S. Oxygen Radical-Induced Single-Strand DNA Breaks and Repair of the Damage in a Cell-Free System. *Mutat. Res. DNA Repair.* **1995**, *337*, 85–95.
(336) Reiter, R. J.; Carneiro, R. C.; Oh, C.-S. Melatonin in Relation to Cellular Antioxidative Defense Mechanisms. *Horm. Metab. Res.* **1997**, *29*, 363–372.
(337) Zimmerman, M. T.; Bayse, C. A.; Ramoutar, R. R.; Brumaghim, J. L. Sulfur and Selenium Antioxidants: Challenging Radical Scavenging Mechanisms and Developing Structure–Activity Relationships Based on Metal Binding. *J. Inorg. Biochem.* **2015**, *145*, 30–40.

(338) Orville A. Levander. Selenium and Sulfur in Antioxidant Protective Systems: Relationships with Vitamin E and Malaria. *Proc. Soc. Exp. Biol. Med.* **1992**, *200*, 255–259.
(339) Müller, A.; Cadenas, E.; Graf, P.; Sies, H. A Novel Biologically Active Seleno-Organic Compound—1: Glutathione Peroxidase-like Activity in Vitro and Antioxidant Capacity of PZ 51 (Ebselen). *Biochem. Pharmacol.* **1984**, *33*, 3235–3239.
(340) Rossato, J. I.; Ketzer, L. A.; Centurião, F. B.; Silva, S. J. N.; Lüdtke, D. S.; Zeni, G.; Braga, A. L.; Rubin, M. A.; Rocha, J. B. T. Antioxidant Properties of New Chalcogenides Against Lipid Peroxidation in Rat Brain. *Neurochem. Res.* **2002**, *27*, 297–303.
(341) Ramoutar, R. R.; Brumaghim, J. L. Antioxidant and Anticancer Properties and Mechanisms of Inorganic Selenium, Oxo-Sulfur, and Oxo-Selenium Compounds. *Cell Biochem. Biophys.* **2010**, *58*, 1–23.
(342) Franzoni, F.; Colognato, R.; Galetta, F.; Laurenza, I.; Barsotti, M.; Di Stefano, R.; Bocchetti, R.; Regoli, F.; Carpi, A.; Balbarini, A.; Migliore, L.; Santoro, G. An in Vitro Study on the Free Radical Scavenging Capacity of Ergothioneine: Comparison with Reduced Glutathione, Uric Acid and Trolox. *Biomed. Pharmacother.* **2006**, *60*, 453–457.
(343) Pastor, N.; Weinstein, H.; Jamison, E.; Brenowitz, M. A Detailed Interpretation of OH Radical Footprints in a TBP-DNA Complex Reveals the Role of Dynamics in the Mechanism of Sequence-Specific Binding11Edited by I. Tinoco. *J. Mol. Biol.* **2000**, *304*, 55–68.
(344) Landry, V. K.; Minoura, M.; Pang, K.; Buccella, D.; Kelly, B. V.; Parkin, G. Synthesis and Structural Characterization of 1-Mesityl-1,3-Dihydro-Imidazole-2-Selone and Bis(1-Mesitylimidazol-2-Yl)Diselenide: Experimental Evidence That the Selone Is More Stable Than the Selenol Tautomer. *J. Am. Chem. Soc.* **2006**, *128*, 12490–12497.
(345) Rong, Y.; Al-Harbi, A.; Kriegel, B.; Parkin, G. Structural Characterization of 2-Imidazolones: Comparison with Their Heavier Chalcogen Counterparts. *Inorg. Chem.* **2013**, *52*, 7172–7182.
(346) Palmer, J. H.; Parkin, G. 2-Seleno-1-Alkylbenzimidazoles and Their Diselenides: Synthesis and Structural Characterization of a 2-Seleno-1-Methylbenzimidazole Complex of Mercury. *Polyhedron* **2013**, *52*, 658–668.
(347) Solomon, E. I.; Gorelsky, S. I.; Dey, A. Metal–Thiolate Bonds in Bioinorganic Chemistry. *J. Comput. Chem.* **2006**, *27*, 1415–1428.
(348) Wachters, A. J. H. Gaussian Basis Set for Molecular Wavefunctions Containing Third-row Atoms. *J. Chem. Phys.* **1970**, *52*, 1033–1036.
(349) Wadt, W. R.; Hay, P. J. Ab Initio Effective Core Potentials for Molecular Calculations. Potentials for Main Group Elements Na to Bi. *J. Chem. Phys.* **1985**, *82*, 284–298.
(350) Hay, P. J. Gaussian Basis Sets for Molecular Calculations. The Representation of 3 d Orbitals in Transition-metal Atoms. *J. Chem. Phys.* **1977**, *66*, 4377–4384.
(351) Roy, G.; Mugesh, G. Selenium Analogues of Antithyroid Drugs – Recent Developments. *Chem. Biodivers.* **2008**, *5*, 414–439.
(352) Roy, G.; Jayaram, P. N.; Mugesh, G. Inhibition of Lactoperoxidase-Catalyzed Oxidation by Imidazole-Based Thiones and Selones: A Mechanistic Study. *Chem. Asian J.* **2013**, *8*, 1910–1921.

(353) Aruoma, O. I.; Halliwell, B.; Gajewski, E.; Dizdaroglu, M. Damage to the Bases in DNA Induced by Hydrogen Peroxide and Ferric Ion Chelates. *J. Biol. Chem.* **1989**, *264*, 20509–20512.

(354) Aruoma, O. I.; Halliwell, B.; Dizdaroglu, M. Iron Ion-Dependent Modification of Bases in DNA by the Superoxide Radical-Generating System Hypoxanthine/Xanthine Oxidase. *J. Biol. Chem.* **1989**, *264*, 13024–13028.

(355) Hart, W. E.; Marczak, S. P.; Kneller, A. R.; French, R. A.; Morris, D. L. The Abilities of Selenium Dioxide and Selenite Ion to Coordinate DNA-Bound Metal Ions and Decrease Oxidative DNA Damage. *J. Inorg. Biochem.* **2013**, *125*, 1–8.

(356) Stadelman, B. S. Synthesis, Characterization, and Reactivity of Iron(II)- and Zinc(II) Complexes of Imidazole Thione and Selone Ligands: Investigations into Oxidation Mechanisms. Dissertation, Clemson University, 2016.

APPENDIX A

CHAPTER II SUPPORTING INFORMATION

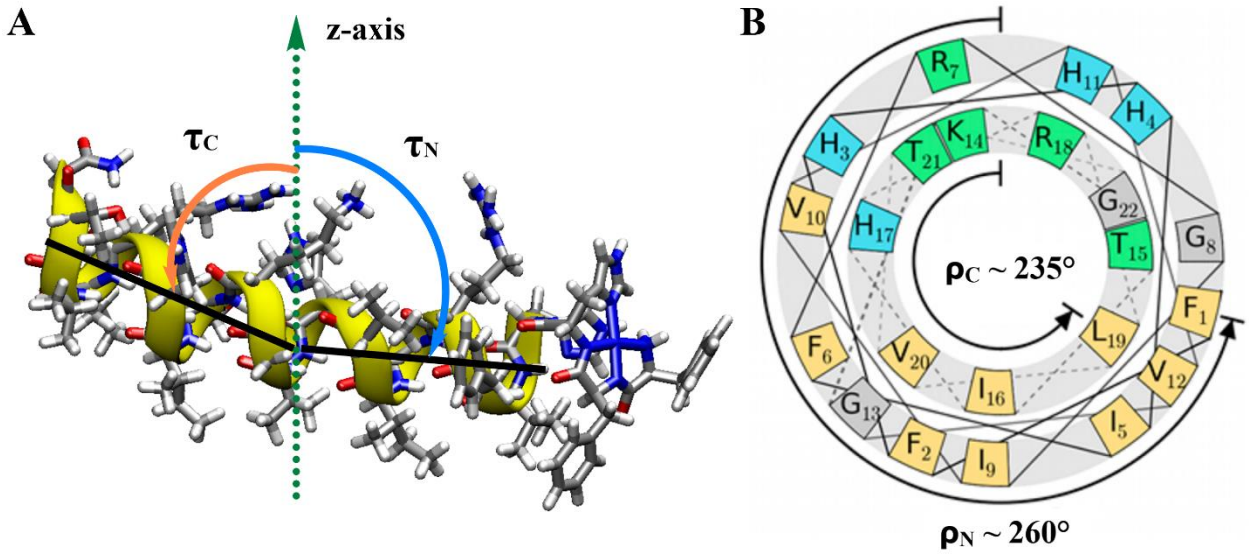

Figure A1. The orientation of the N- and C-terminal ends of the peptide in the bilayer described by the (A) tilt and (B) azimuthal rotational angles. The tilt angle, τ, defines the orientation of the helical axis with respect to the bilayer normal (z-axis), and the azimuthal rotation angle, ρ, is the rotation of the helix around its helical axis.

APPENDIX B

CHAPTER III RESEARCH FEATURED ON JOURNAL COVER

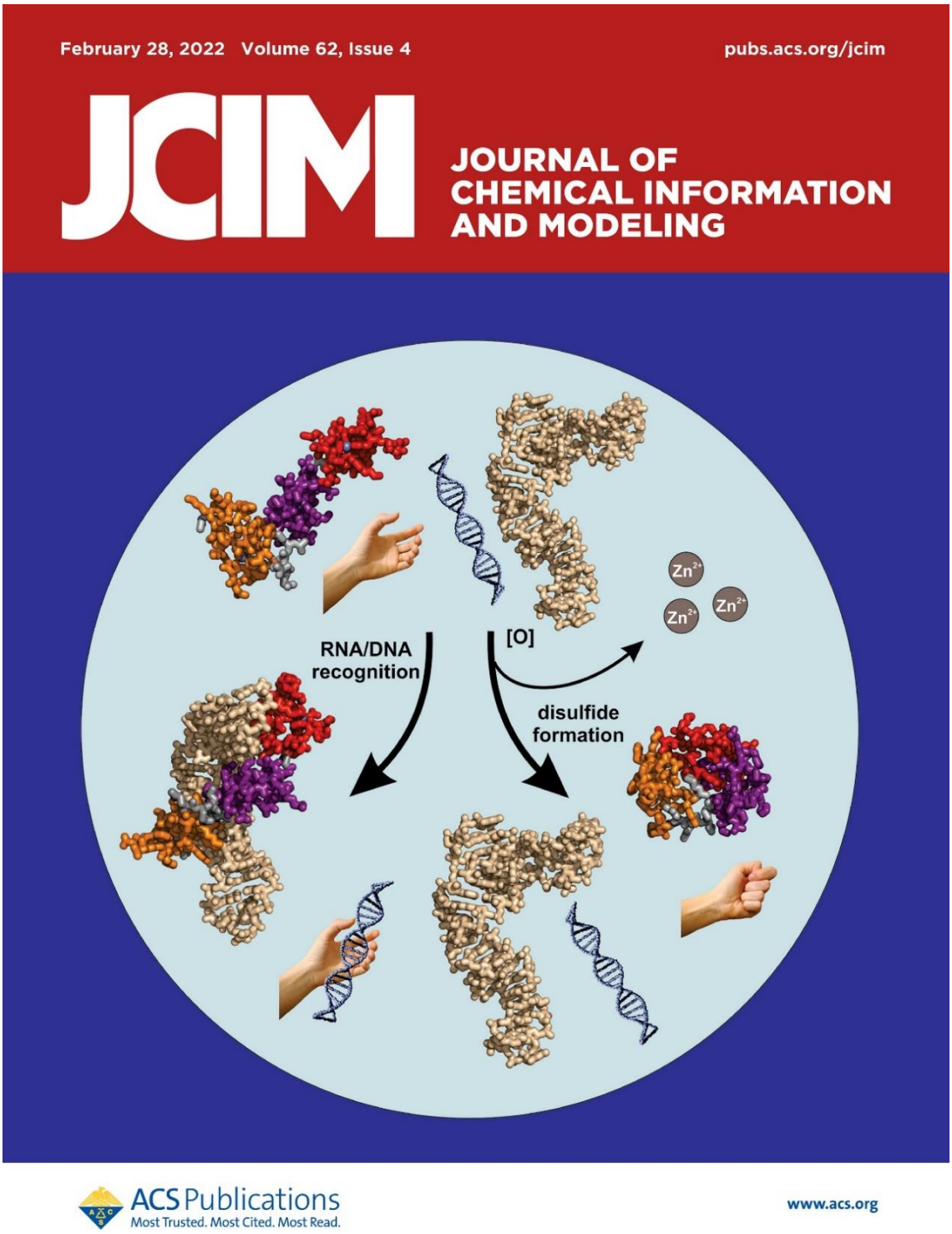

APPENDIX C

CHAPTER III SUPPORTING INFORMATION

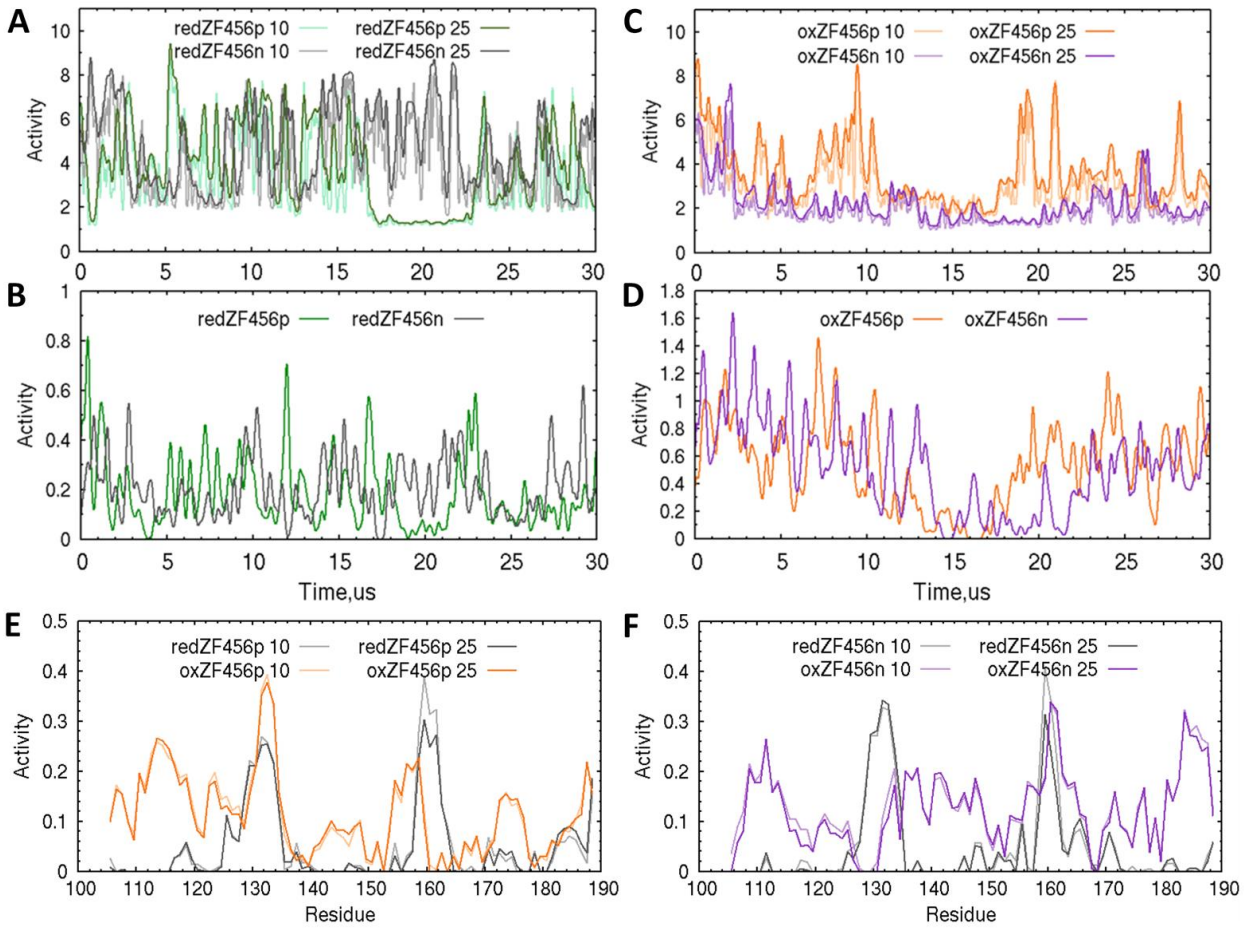

Figure A2. Trajectory Analysis of the reduced and oxidized ZF456 in the absence of RNA using the TimeScapes package. Comparison of filtering on the RMS fluctuations of (A) redZF456 and (B) oxZF456 using 25 and 10 sliding windows. Event detection activity determined by cutoff-(6.0–7.0 Å crossing buffer) screening using the 25-frame screened trajectory of (C) redZF456 and (D) oxZF456. Pivot angle activity in (E) protonated and (F) neutral ZF456 peptide determined by Pearson projection using 25 and 10 sliding windows.

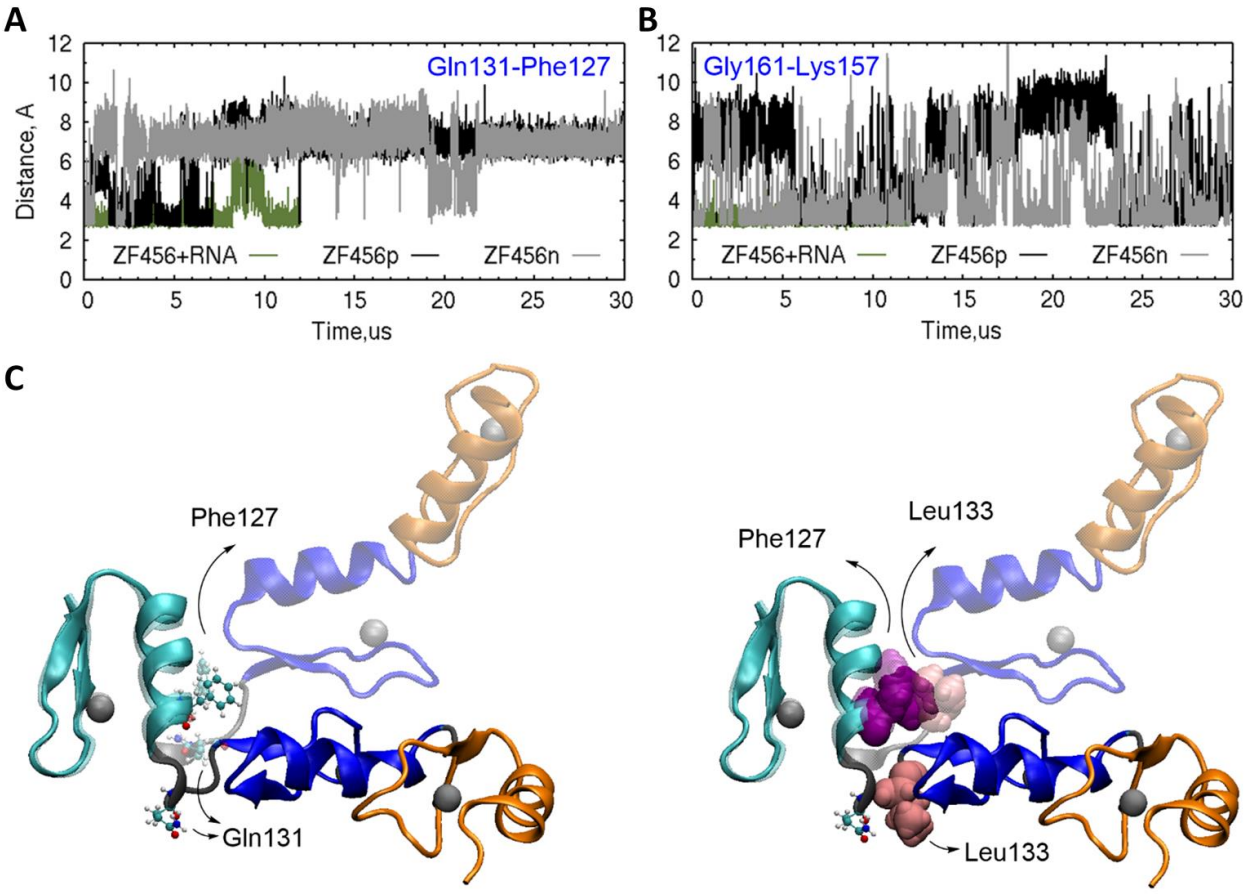

Figure A3. Comparison of linkers structure in reduced ZF456 in presence and absence of 5S RNA. Distance plot of the hydrogen bond within the (A) ZF4-ZF5 and (B) ZF5-ZF6 linker. (C) Snapshots from the simulations showing the change in the ZF4-ZF5 linker structure interactions upon RNA removal. The three zinc fingers are depicted as cartoon and colored in cyan (ZF4), blue (ZF5) and orange (ZF6). The gray spheres represent the Zn^{2+} ions. The faded conformation is from the simulation of ZF456 – 5S RNA complex. The structures are best fitted with respect to ZF4.

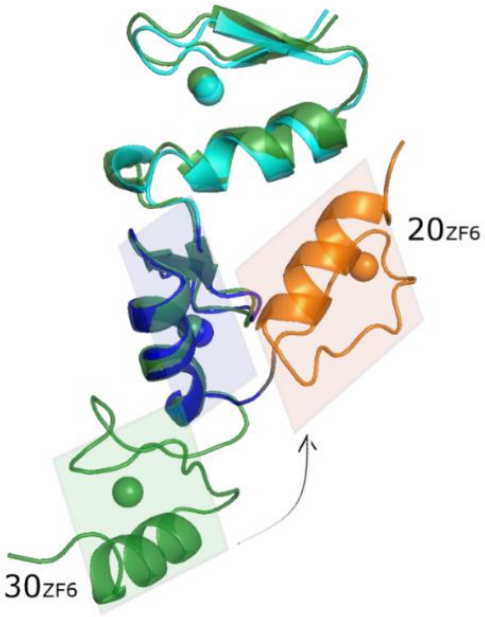

Figure A4. Closing of the ZF5-ZF6 interface seen in the long-lived conformation *redZF456p*.

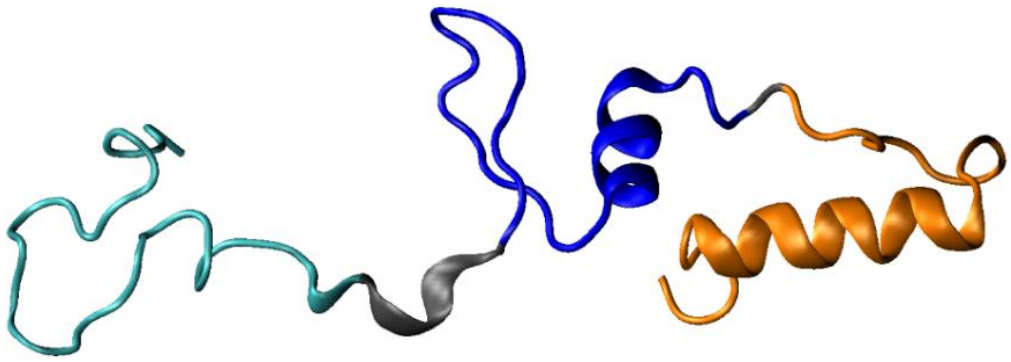

Figure A5. Snapshot from the simulation of *oxZF456p* showing the unfolding of ZF4 and opening of the ZF4-ZF5 interface.

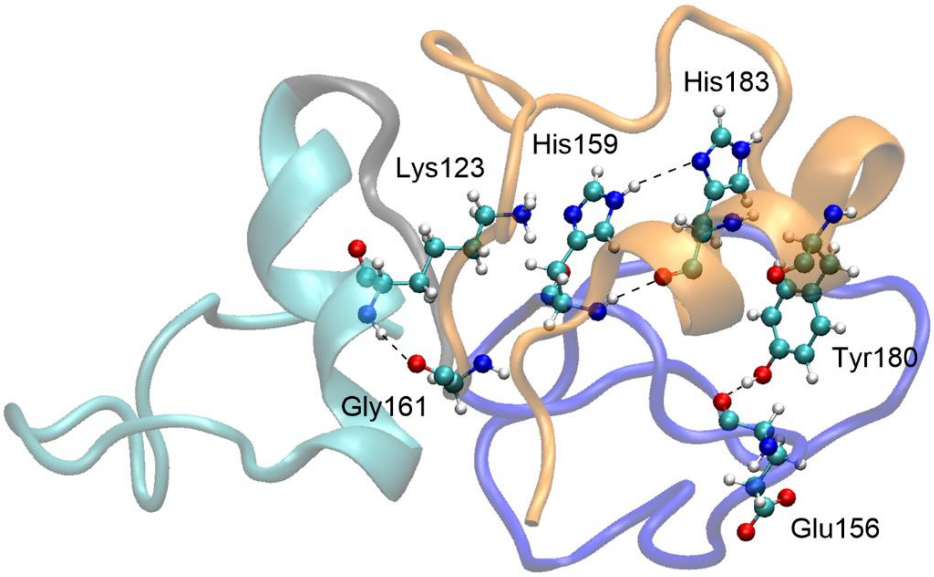

Figure A6. Interdomain hydrogen bonds in the globular conformation of *oxZF456n*.

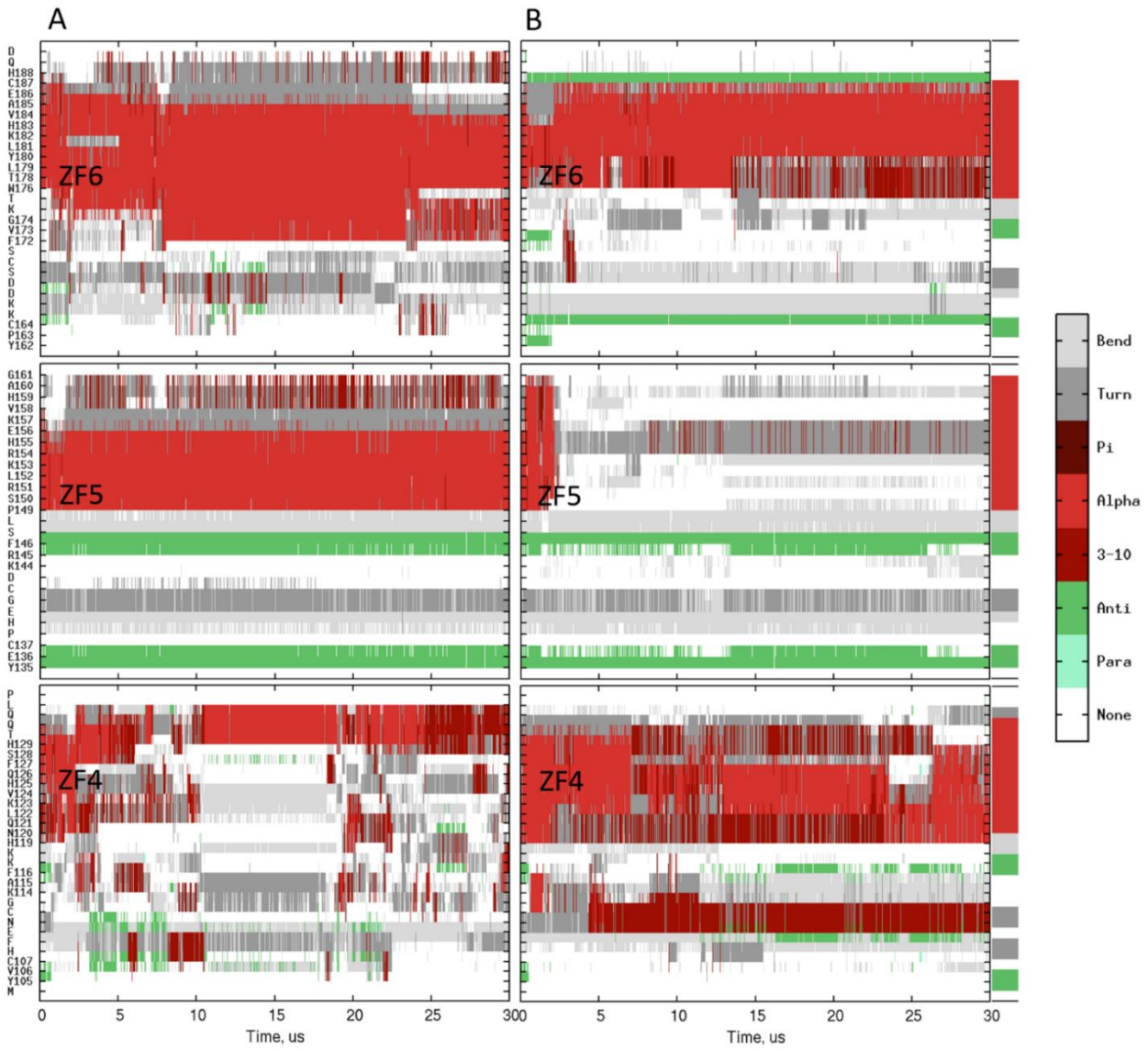

Figure A7. Comparison of the secondary structure modifications of (A) *oxZF456p* and (B) *oxZF456n* in the absence of 5S RNA. The initial secondary structure of each ZF is shown on the right. Only the residues within the β-hairpin and α-helix are numbered.

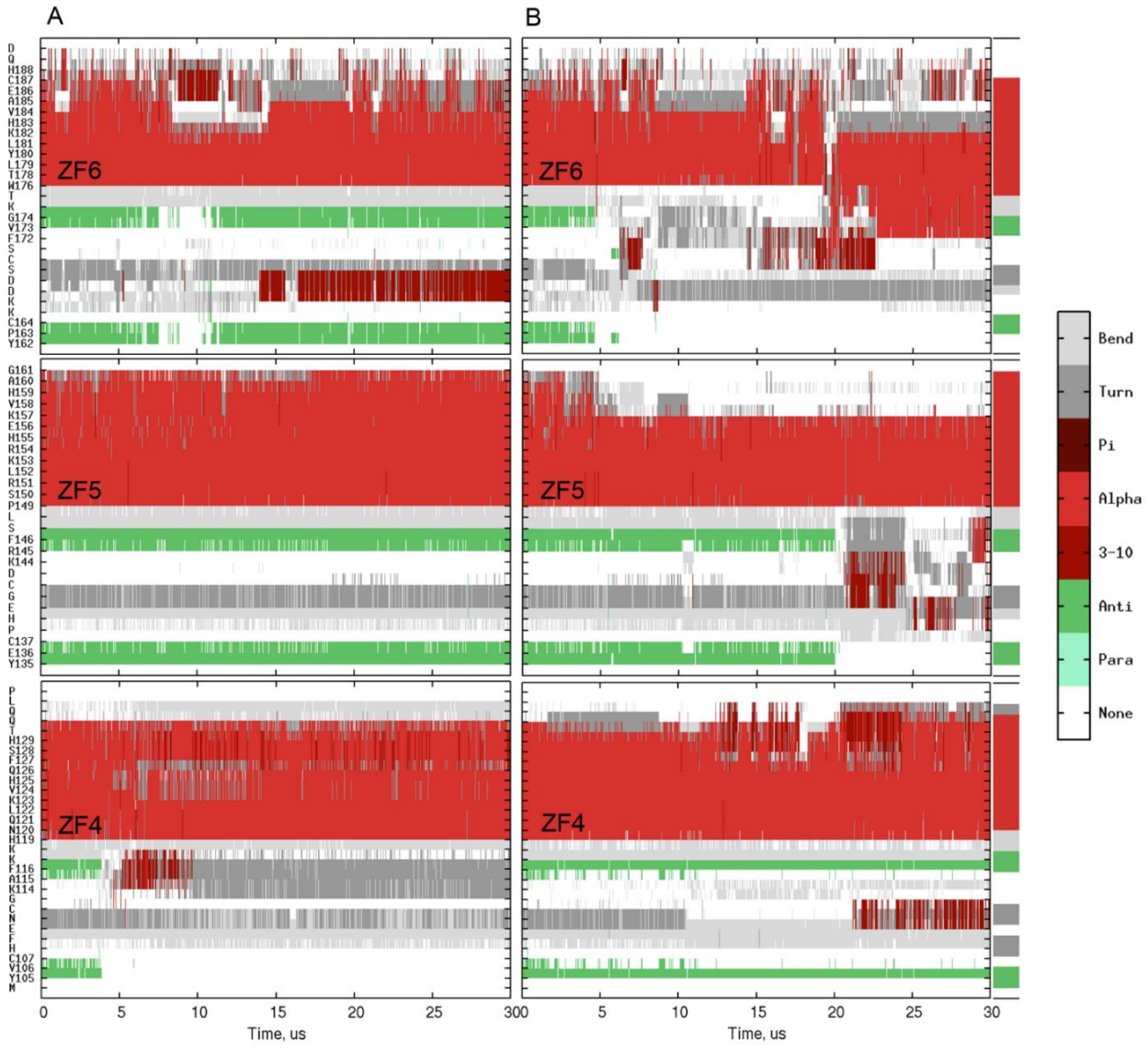

Figure A8. Comparison of the secondary structure modifications of (A) *oxZF456p* and (B) *oxZF456n* in the presence of 5S RNA. The initial secondary structure of each ZF is shown on the right. Only the residues within the β-hairpin and α-helix are numbered.

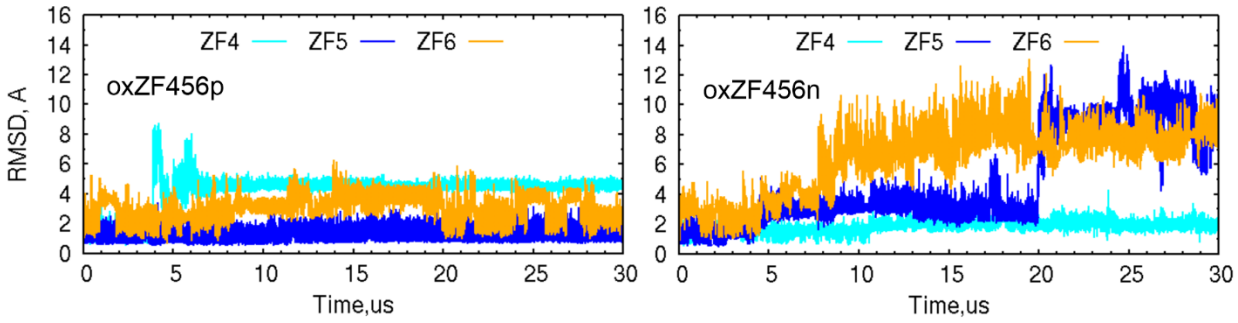

Figure A9. RMSD of individual ZF domains in the simulation of the oxZF56 - 5SRNA complex

Table A1. Hydrogen bonds with population >20.0% in the simulations of reduced ZF456-5S RNA. H-bonds that populated at least 40% of the frames are defined as key and shown in bold. Hydrogen bonds involving the Lys residues are reported as the sum of up to three populations (same H-bond acceptor and donor but different H atom).

H-bond acceptor	**H-bond donor**	**redZF456**	**oxZF456p**		**oxZF456n**	
		0-12 μs	*0-12 μs*	*18-30 μs*	*0-12 μs*	*18-30 μs*
			ZF4			
G26 b-N7	His119 BB	91.4	41.2	-	72.0	62.0
G26 b-O6	Asn120 BB	82.9	21.4	-	90.7	96.7
A25 s	Lys118 SC	56.2	21.0	5.9	32.4	24.6
G40 p'	Lys123 SC	40.4	13.5	-	80.1	82.7
G41 p"	Lys123 SC	38.9	9.5	-	84.8	92.2
U23 p	Lys117 SC	37.4	10.7	-	29.3	31.0
A25 s	Lys118 SC	30.9	28.1	17.4	12.7	12.5
A42 p	Asn120 SC	23.3	4.0	-	30.1	32.2
			ZF5			
U7 p'	Arg154 SC-$N^{\eta 2}$	59.8	43.0	2.3	35.9	-
A6 p'	Arg154 SC-$N^{\eta 2}$	55.6	25.9	-	38.2	-
A6 p'	Arg154 SC-N^{ε}	47.3	31.5	-	21.2	-
U7 p'	Arg154 SC-$N^{\eta 1}$	28.7	33.9	7.2	14.6	<1.0
U20 p'	Arg151 SC-$N^{\eta 2}$	27.7	34.2	77.8	3.2	-
A6 b-N7	Lys157 SC	27.3	11.9	<1.0	6.9	-
U20 p'	Arg151 SC-N^{ε}	26.5	33.5	-	0.8	-
G21 p"	Arg151 SC-$N^{\eta 2}$	26.0	30.2	95.1	2.5	-
A6 p"	Lys157 SC	20.4	9.8	-	7.4	-
			ZF6			
A6 p"	Tyr162 SC	97.3	95.3	-	55.0	-
C5 b-O2	Thr178 BB	95.7	93.0	-	64.9	-

Table A1. Continued

H-bond acceptor	H-bond donor	redZF456	oxZF456p		oxZF456n	
		0-12 μs	*0-12 μs*	*18-30 μs*	*0-12 μs*	*18-30 μs*
			ZF6			
C5 s	Trp177 BB	92.8	95.7	-	65.0	-
A8 s	Trp177 SC	90.6	87.5	-	60.9	-
Tyr162 SC	C5 s	67.5	72.7	-	28.6	-
C5 b-O2	Thr178 SC	65.8	89.5	-	50.6	-
C5 b-N3	Thr178 SC	560	27.9	<1.0	27.8	-
C5 b-N3	Thr176 SC	29.6	20.3	-	10.4	-

Table A2. Hydrogen bonds with population >40% in the oxZF456p-5S RNA simulation but absent in the reduced ZF456-5SNA. Hydrogen bonds involving the Lys residues are reported as the sum of up to three populations (same H-bond acceptor and donor but different H atom).

H-bond acceptor	**H-bond donor**	**oxZF456p**	
		0-12 μs	*18-30 μs*
	ZF4		
G26 p	Lys118 SC	48.1	79.5
U24 p	Lys118 SC	44.3	78.3
U23 p	Asn120 SC	43.5	0.9
G22 p"	Lys123 SC	40.3	0.0
G22 p'	Lys123 SC	2.8	94.5
G40 p'	Tyr105 BB	22.5	91.8
G40 p"	Lys117 SC	20.8	56.8
G39 b-O6	Lys114 SC	11.9	55.1
G41 b-N7	Lys117 SC	24.6	52.3
U38 p	Gly113 BB	11.6	50.5
	ZF5		
U20 p'	Arg151 SC-$N^{\eta 1}$	8.1	97.4
U20 p"	Arg154 SC-$N^{\eta 1}$	2.5	84.5
C19 p'	Arg154 SC-$N^{\eta 1}$	5.4	80.7
U20 p'	Arg154 SC-N^{ε}	6.7	74.7
G21 p'	Arg151 SC-N^{ε}	0.5	69.3
G21 p"	Ser150 SC	0.3	62.1
C19 p'	Arg154 SC-$N^{\eta 2}$	4.0	60.9
	ZF6		
A6 p"	Thr178 BB	-	97.5
A6 p"	Thr178 SC	-	96.6
A6 p'	Trp177 BB	-	85.1
C9 s	Trp177 SC	-	76.9

Table A3. **Hydrogen bonds with population >40% in the oxZF456n simulations but absent in the reduced ZF456-5S RNA**. Hydrogen bonds involving the Lys residues are reported as the sum of up to three populations (same H-bond acceptor and donor but different H atom).

H-bond acceptor	**H-bond donor**	**oxZF456n**	
		0-12 μs	*18-30 μs*
	ZF4		
G26 p	Lys117 SC	46.8	50.0
G22 p"	Gln121 SC	44.8	57.5
U24 p	Lys117 SC	43.7	46.2
G22 p'	Lys114 SC	31.9	51.8
G41 p'	Asn120 SC	34.7	47.7
G21 p'	Gln121 SC	32.5	47.7
	ZF5		
U7 p"	Arg154 SC-$N^{\eta 1}$	55.2	98.8
U7 p"	Arg154 SC-$N^{\eta 2}$	43.3	93.3
G17 s	Arg154 SC-N^{ε}	18.5	88.2
A6 p'	Arg151 SC-$N^{\eta 2}$	24.3	83.4
C18 p	Lys157 SC	3.1	72.0
U7 p'	Arg151 SC-$N^{\eta 1}$	23.7	66.3
C19 p"	Lys153 SC	6.7	61.8
A6 p'	Arg151 SC-N^{ε}	23.4	58.5
U7 p'	Arg151 SC-$N^{\eta 2}$	25.4	57.2
	ZF6		
C18 p	Tyr162 SC	-	90.7
C5 b-O2	Lys166 SC	-	42.9
C9 s	Asp167 BB	-	40.8

APPENDIX D

RIGHTS AND PERMISSIONS

VITA

ANA DREAB

Department of Chemistry and Biochemistry
Old Dominion University
Norfolk, VA 23529

EDUCATION

Anticipated Ph.D. in Chemistry,	Old Dominion University, Norfolk, VA, May 2022
M.S. in Chemistry,	Old Dominion University, Norfolk, VA, May 2020
B.S. in Chemistry,	University of Academy of Science of Moldova, Chisinau, Moldova, June 2015

PROFESIONAL EXPERIENCE

Graduate teaching assistant, ODU, 2016-2022

Research assistant for Dr. Craig. A. Bayse, ODU, 2017-2022

PUBLICATIONS

Marsan, E. S.; Dreab, A.; Bayse, C. A. In silico Insights into the Dimer Structure and Deiodinase Activity of Type III Iodothyronine Deiodinase from Bioinformatics, Molecular Dynamics Simulations, and ONIOM Calculations. *J. Biomol. Struct. Dyn*. **2022**, *in review*.

Dreab, A.; Bayse, C.A. Molecular dynamics simulations of reduced and oxidized TFIIIA zinc fingers free and interacting with 5S RNA. *J. Chem. Inf. Model*. **2022**, *62*, 903-913.

Dreab, A.; Brewer, M.I.; Bayse, C.A. DFT modeling of the prevention of Fe(II)-mediated redox damage by imidazole-based thiones and selones. *J. Inorg. Biochem.* **2019**, *193*, 9-14.

Coropceanu, E.B.; Dreab, A.; Croitor, L. Two Zn(II) mononuclear coordination compounds with pyridinedicarboxylate and auxiliary N-(pyridin-4-ylmethylidene) hydroxylamine ligands. *Acta Cryst. C* **2014**, *70*, 1101-1104.

SELECTED PRESENTATIONS

Dreab, A.; Cotton, M.L.; Bayse, C.A. Modeling of metal-binding antimicrobial peptides in lipid bilayers. ACS National Meeting in Atlanta, GA, August 22-26, **2021**.

Dreab, A.; Lutz, P.B.; Bayse, C.A. QM/MM MD simulations of zinc finger proteins and their reactivity with reducible sulfur and selenium compounds. ACS National Meeting in Orlando, FL, March 31 – April 4, **2019**.

Dreab, A.; Brewer, M.I.; Brumaghim, J.L.; Bayse, C.A. DFT modeling of the prevention of Fe(II)-mediated redox damage by sulfur and selenium compounds. SERMACS in Charlotte, NC, November 7–11, **2017**.